Calculation of electronic and magnetic properties of hybrid low-dimensional structures

Dissertation
zur Erlangung des Doktorgrades
des Fachbereichs Physik

vorgelegt von
Lilli Sacharow
aus Karaganda (Kasachstan)

Hamburg 2006

Gutachter der Dissertation:
Prof. Dr. R. Wiesendanger
Prof. Dr. S. Blügel

Gutachter der Disputation:
Prof. Dr. R. Wiesendanger
Prof. Dr. A. Lichtenstein

Datum der Disputation:
28.04.2006

Vorsitzender des Prüfungsauschusses:
Dr. A. Chudnovski

Vorsitzender des Promotionsausschusses:
Prof. Dr. G. Huber

Dekan des Fachbereichs Physik
Prof. Dr. G. Huber

Inhaltsangabe

Der Hauptteil der vorliegenden Arbeit widmet sich der theoretischen Untersuchung der elektronischen und magnetischen Struktur von Fe-Ketten auf der InAs(110) Oberfläche. Dazu wird zuerst die Geometrie der Fe-Monolage/InAs(110) mit einem Fe-Atom pro InAs(110) Einheitszelle berechnet. Ausgehend von dieser Geometrie werden die relaxierten Positionen der Fe- und InAs-Atome für die Fe-Ketten entlang der $[1\bar{1}0]$- und entlang der [001]-Richtungen bestimmt. Mit dieser Geometrie wird dann die jeweilige magnetische Grundstruktur bestimmt. Ausgehend von der Bandstruktur und den relevanten Zustandsdichten werden Modelle der Austauschwechselwirkung zwischen den Fe-Atomen aufgestellt. Ausserdem werden für die untersuchten Systeme die STM-Konstantstrom-Bilder und dI/dU-Karten simuliert und mit den experimentellen Daten aus STM-Messungen auf Fe-Multimeren verglichen.

Die Motivation für den zweiten Teil der Arbeit sind gemessene Rastertunnelspektroskopie-Daten von Co-Inseln auf der Co(0001) Oberfläche. Dabei wurde ein elektronischer Zustand unterschiedlicher Intensität bei -300 meV auf topographisch ähnlichen Co-Inseln gemessen. Um dieses Ergebnis besser interpretieren zu können, wird die Co(0001) Oberfläche mit der obersten Monolage in fcc- und hcp-Stapelung mit Hilfe der Dichtefunktionaltheorie simuliert. Auf der Basis der berechneten elektronischen Eigenschaften beider Stapelfolgen wird ein Modell zur Interpretation der experimentellen Daten entwickelt.

Abstract

The first part of this work presents a theoretical study of the electronic and magnetic structure of Fe chains on the InAs(110) surface. To achieve this, first the geometry of an Fe ML/InAs(110) with a coverage of one atom per unit cell is calculated. Using this geometry as a starting situation the relaxed positions of Fe and InAs atoms are calculated for the Fe chains along $[1\bar{1}0]$ and [001] directions. With this calculated geometry the energetically preferable magnetic structure is determined. From the electronic properties like band structure and relevant densities of states the models of the exchange interaction between Fe atoms in the chain are suggested. Additionally, STM constant current images and dI/dU maps are simulated for the studied systems and are compared with experimental STM data on Fe multimers.

The motivation for the second part of the work were experimentally obtained scanning tunneling spectroscopy measurements on Co islands on a Co(0001) surface. A state of varying intensity was measured on topographically similar islands at -300 meV. To understand this result, density functional theory based calculations are performed on a Co(0001) surface terminated with a monolayer in hcp and fcc stacking. An explanation of the experimental results is given on the basis of the calculated electronic properties of both stackings.

Contents

Chapter 1

Introduction

With the decreasing dimensions of electronic devices the quantum phenomena start to play an increasing role. The study of these phenomena is a major topic in todays' solid state physics. Out of this range of phenomena spin electronics (spintronics) is attracting a great amount of attention in the academic world, and even outside of it. The spin transistor proposed by Datta and Das [11] has moved the interface between a ferromagnet and a semiconductor into the focus of research. Due to its high electron mobility and large effective g-factor of the bulk, InAs is a promising candidate for spintronic applications. Among the magnetic materials Fe is an interesting and highly controversial candidate. Despite the multiplicity of theoretical [15, 54] and experimental [20, 56] studies on Fe for spintronic applications the detailed mechanism of interaction between Fe and semiconductors is still unclear. In this work a lot of attention is paid to understand the interaction between Fe and InAs directly at the interface. The covalent, strongly direction-dependent bonding in InAs raises the question about the direction dependence of the interaction between the Fe atoms on the InAs surface. To address this question we decided to study Fe chains along two perpendicular directions on InAs(110). A reduction of dimensionality can lead to additional interesting effects.

I simulate the electronic and magnetic structure of the Fe/InAs system within density functional theory (DFT). DFT is a theory developed in the last decades [22, 25], which allows the computation of the electronic structure of crystalline materials from first principles. DFT allows the substitution of the many-particle Schrödinger equation by the effective single-particle (Kohn-Sham) equations.

In chapter 2 the Kohn-Sham equations are derived from the DFT, and a full-potential linarized augmented plane wave method (FLAPW) is introduced to solve them, as it is implemented in the FLEUR code [23]. This

method allows a very accurate calculation of the geometry and magnetic structure of the studied systems. The precision is paid for by a high numerical effort of the calculation.

To reduce this effort in the determination of the geometry, insights gained from experiments are used, namely measurements with the scanning tunneling microscope (STM), an invention of the 1980's [5, 6]. The STM allows measurements of the local density of states (LDOS) of the sample with a high spatial resolution, exploiting the quantum mechanical tunneling. Additionally, the interaction between the tip of the STM and atoms at the sample surface can be used to move the atoms of the sample and in this way structure the surface. The complexity of the quantum mechanical tunneling makes the interpretation and prediction of STM results a difficult task. Here we use an approximative model for the interpretation, which is described in detail in chapter 3. Nevertheless, we should be aware that the effects of inelastic tunneling, the interaction between tip and sample as well as the specific electronic structure of the tip are neglected in this approximation.

After the introduction of the tools used in this work in chapter 2 and 3 the results are presented in chapter 4 to 7.

To calculate the electronic structure the geometry of the system has to be determined first. For the Fe chains on InAs a large unit cell has to be used. This makes a good first guess for the position of the Fe and surrounding InAs atoms important. In the first part of chapter 4 the calculation for an Fe monolayer on InAs(110) is presented. This is less demanding on the computational ressources than Fe chains and at the same time gives the starting position for the geometry optimization of Fe chains. The results of this optimization are shown in the second and third part of chapter 4.

In chapter 5 the magnetic and electronic structure of Fe chains on InAs(110) is described for the relaxed structure and compared with STM measurements on Fe multimers.

Motivated by STM measurements of Co islands on Co(0001) a completely different system is studied in chapter 6, namely Co(0001), which is often used in layered magnetic thin-film structures.

Chapter 2

Density Functional Theory

2.1 Kohn-Sham equations

The goal of solid state physics is to investigate and to understand the properties of materials, which are many-body systems containing an enormously large number of interacting electrons and ions. Due to the complexity of this problem it cannot be solved even nowadays neither analytically no numerically. First attempts to find some simplifications were made a long time ago. The most essential among them is the Born-Oppenheimer approximation, which is employed by the majority of first-principle calculations. It states that as the electrons are very light compared with the nuclei, they move much more rapidly and one can neglect all the quantum effects due to the motion of the nuclei. In other words, in this approximation the positions of ions are fixed, and the Hamiltonian of the system becomes:

$$\mathcal{H} = \sum_{i=1}^{N} -\frac{\hbar^2}{2m}\nabla_i^2 + \frac{1}{2}\sum_{i,j}\frac{e^2}{|\mathbf{r}_i - \mathbf{r}_j|} - \sum_{i,I}\frac{Z_I e^2}{|\mathbf{r}_i - \mathbf{R}_I|} + \frac{1}{2}\sum_{I,J}\frac{Z_I Z_J}{|\mathbf{R}_I - \mathbf{R}_J|}, \quad (2.1)$$

where Z_I denotes the charge of the nucleus I, $\mathbf{R}_I$ is the position of the nucleus I and $\mathbf{r}_i$ the positions of the electrons. But even with this simplification there is not an analytical or numerical solution for this Hamiltonian, if more than a few electrons are considered.

A reduction of the complicated many-body problem to an effective single-particle theory which can be applied for the numerical prediction of the different properties for different types of materials and which also supplies deeper physical insight is the density functional theory by Hohenberg, Kohn and Sham [22, 25].

The Hamiltonian of N interacting electrons is decomposed into three

parts:

$$\mathcal{H} = T + V + U,$$

where T is the kinetic energy operator:

$$T = -\frac{\hbar^2}{2m}\sum_i \nabla_i^2,$$

the quantity V denotes the external potential, which in the Born-Oppenheimer approximation consists of the potential due to the fixed ions, and possibly other external fields:

$$V = \sum_i \left(V_{field}(\mathbf{r}_i) + \sum_j V_{ion}(\mathbf{r}_i - \mathbf{R}_j) \right). \tag{2.2}$$

The last term of the Hamiltonian is the Coulomb electron-electron interaction:

$$U = \sum_{ij, i\neq j} \frac{e^2}{|\mathbf{r}_i - \mathbf{r}_j|}. \tag{2.3}$$

We focus our attention on the observable properties of the system like the electron density or the ground-state energy. The electron density operator is defined as:

$$\hat{n}(\mathbf{r}) = \sum_{i=1}^{N} \delta(\mathbf{r} - \mathbf{r}_i), \tag{2.4}$$

from which the electron density is given by:

$$n(\mathbf{r}) = \langle \Phi | \hat{n}(\mathbf{r}) | \Phi \rangle,$$

where Φ is a many-body state. Hohenberg and Kohn discovered that this quantity is actually a crucial variable. This is reflected in two famous theorems.

1. The total ground-state energy, E, of any many-electron system is a functional of the density $n(\mathbf{r})$:

$$E[n] = F[n] + \int n(\mathbf{r}) V_{ext}(\mathbf{r})\, d\mathbf{r}, \tag{2.5}$$

where $F[n]$ is a functional of the density, but independent of the external potential.

2. For any many-electron system the functional $E[n]$ for the total energy has a minimum equal to the total ground-state energy at the ground-state density.

The second theorem allows a use of the variational calculation to derive a single-particle Schrödinger equation. This was done by Kohn and Sham who split the functional $F[n]$ into three parts:

$$F[n] = T[n] + \int\int \frac{n(\mathbf{r})n(\mathbf{r}')}{|\mathbf{r}-\mathbf{r}'|}\, d\mathbf{r}\, d\mathbf{r}' + E_{xc}[n], \tag{2.6}$$

which describe the kinetic, Hartree and exchange-correlation energy. In contrast to the Hartree integral, an explicit form of the other functionals, T and E_{xc} is not known in general. Ignoring this problem at the moment, we use the variational principle and write:

$$\frac{\delta E[n]}{\delta n(\mathbf{r})} + \mu \frac{\delta(N - \int n(\mathbf{r})\, d\mathbf{r})}{\delta n(\mathbf{r})} = 0, \tag{2.7}$$

where μ is a Lagrange multiplier taking care of particle conservation. We now split up the kinetic energy into a term T_0 reflecting the kinetic energy of noninteracting particles and T_{xc} which stands for the rest, i.e. we write:

$$T = T_0 + T_{xc}.$$

Here we are making an important step, we represent the density in the following form:

$$n(\mathbf{r}) = \sum_{i=1}^{N} |\psi_i(\mathbf{r})|^2, \tag{2.8}$$

where we assume that we can determine the 'single-particle' wave-functions ψ_i so that the density can be represented in this form. The question if every possible electron density can be written in this form is open. Then we are writing the kinetic energy of noninteracting particles as:

$$T_0[n] = -\frac{\hbar^2}{2m} \sum_{i=1}^{N} \int \nabla\psi_i^*(\mathbf{r}) \nabla\psi_i(\mathbf{r})\, d\mathbf{r}. \tag{2.9}$$

Since the Schödinger equation is just an Euler-Lagrange equation obtained by varying $T_0[n]$ plus a potential energy term we come to:

$$\left(-\frac{\hbar^2}{2m}\nabla^2 + V_{eff}(\mathbf{r}) \right) \psi_i(\mathbf{r}) = \epsilon_i \psi_i(\mathbf{r}). \tag{2.10}$$

Now we determine the effective potential which affects the ith 'single particle', such that the density $n(\mathbf{r})$ minimizes the energy functional. Thus, requiring

the functions ψ_i to be normalized, multiplying the last equation with ψ_i^*, integrating and adding we obtain:

$$T_0[n] = \sum_{i=1}^{N} \epsilon_i - \int V_{eff}(\mathbf{r}) n(\mathbf{r})\, d\mathbf{r}. \tag{2.11}$$

Noting that $\frac{\delta T_0[n]}{\delta n} = -V_{eff}(\mathbf{r})$ variation of the energy functional is now easily carried out:

$$V_{eff}(\mathbf{r}) = V_{ext}(\mathbf{r}) + 2\int \frac{n(\mathbf{r}')}{|\mathbf{r}-\mathbf{r}'|}\, d\mathbf{r}' + V_{xc}(\mathbf{r}) \tag{2.12}$$

with

$$V_{xc}(\mathbf{r}) = \frac{\delta(E_{xc}+T_{xc})}{\delta n(\mathbf{r})}. \tag{2.13}$$

The effective single-particle equation,

$$\left(-\frac{\hbar}{2m}\nabla^2 + V_{eff}(\mathbf{r})\right)\psi_i(\mathbf{r}) = \epsilon_i \psi_i(\mathbf{r}) \tag{2.14}$$

is called the Kohn-Sham equation. It is a Schröedinger equation with the external potential replaced by the effective potential which depends on the density. The density itself depends on the single-particle states ψ_i. The Kohn-Sham equation thus constitutes a self-consistent problem. By choosing some reasonable starting density, which is usually constructed from the densities of isolated atoms, the starting potentials are defined. Then by solving the Kohn-Sham equations the output density is constructed. The output density is mixed with the input density afterwards, thus becoming the starting density for the next iteration. This iterative process is repeated until the distance between the output and starting density becomes small. In this case the calculation is converged and the ground-state density is found.

The Kohn-Sham equation furthermore allows us to derive an alternative expression for the total energy:

$$E[n] = \sum_{i=1,\epsilon_i \le E_F}^{N} \epsilon_i - \int\int \frac{n(\mathbf{r})n(\mathbf{r}')}{|\mathbf{r}-\mathbf{r}'|}\, d\mathbf{r}\, d\mathbf{r}' - \int V_{xc}(\mathbf{r}) n(\mathbf{r})\, d\mathbf{r} + E_{xc}[n]. \tag{2.15}$$

The total energy thus consists of the sum over the eigenvalues, ϵ_i, minus the so-called 'double-counting' terms. Note that in the term E_{xc} we also included the exchange-correlation kinetic energy T_{xc}.

Although density-functional theory provides the scheme to reduce the entire many-body problem to a Schrödinger-like effective single-particle equation, the physical meaning of the eigenvalues ϵ_i is not clear. These eigenvalues have been used very often and with success to interpret excitation spectra. But there also some problematic cases like photoinduced exitations or bulk plasmons.

2.2 Spin Density Functional Theory

There are a lot of materials that possess a non-zero magnetisation in the ground state. The DFT was extended to the case of spin polarized electrons from Barth and Heidin [50] to describe materials of that kind. In this case the energy functional depends on the electon density $n(\mathbf{r})$ and on the magnetization density $\mathbf{m}(\mathbf{r})$. By introducing the two component Pauli wave function:

$$\boldsymbol{\psi}_i = \begin{pmatrix} \psi_i^{\uparrow}(\mathbf{r}) \\ \psi_i^{\downarrow}(\mathbf{r}) \end{pmatrix}, \tag{2.16}$$

we can write for the charge density and magnetisation density:

$$n(\mathbf{r}) = \sum_{i=1}^{N} |\boldsymbol{\psi}_i(\mathbf{r})|^2 \qquad \mathbf{m}(\mathbf{r}) = \mu_B \sum_{i=1}^{N} \boldsymbol{\psi}_i^* \boldsymbol{\sigma} \boldsymbol{\psi}_i. \tag{2.17}$$

Applying the variational principle:

$$E[n(\mathbf{r}), \mathbf{m}(\mathbf{r})] \geq E[n_0(\mathbf{r}), \mathbf{m}_0(\mathbf{r})] \tag{2.18}$$

we obtain again the KS equations:

$$\begin{aligned} (-\frac{\hbar^2}{2m}\nabla^2 + V_{eff}(\mathbf{r}) + \boldsymbol{\sigma}\mathbf{B}_{eff}(\mathbf{r}))\boldsymbol{\psi}_i(\mathbf{r}) = \epsilon_i \boldsymbol{\psi}_i(\mathbf{r}) \qquad \text{with} \\ V_{eff}(\mathbf{r}) = V_{ext}(\mathbf{r}) + 4\pi e \int \frac{n(\mathbf{r}')}{|\mathbf{r} - \mathbf{r}'|} d\mathbf{r}' + \frac{\delta E_{xc}[n(\mathbf{r})]}{\delta n(\mathbf{r})}. \end{aligned} \tag{2.19}$$

For collinear spin structures, like ferromagnetic and antiferromagnetic alignment, the choice of the z-axis along the magnetic field $\mathbf{B}_{eff} = (0, 0, B_{eff})$ results in the diagonal form of the Hamiltonian in (2.19). So the problem (2.19) can be solved independently for both spin components. In this case the energy functional depends only on $|\mathbf{m}(\mathbf{r})|$ and $n(\mathbf{r})$. With a trivial transformation:

$$\begin{aligned} n(\mathbf{r}) &= n_{\uparrow}(\mathbf{r}) + n_{\downarrow}(\mathbf{r}) \\ m(\mathbf{r}) &= n_{\uparrow}(\mathbf{r}) - n_{\downarrow}(\mathbf{r}), \end{aligned}$$

E becomes dependent on the densities of spin up and spin down electrons:

$$n_{\sigma}(\mathbf{r}) = 2 \sum_{i=1}^{N} |\psi_i^{\sigma}(\mathbf{r})|^2. \tag{2.20}$$

Up to this point we have an exact theory. No approximations have been made. So if we could write the exchange-correlation functional in an explicit

form, this would be a perfect theory to calculate all ground state properties of the system. Actual state of affairs is that only approximative representations for E_{xc} have been found. One very widely used approach is the local spin density approximation (LSDA), which is described in the following.

2.3 The Local Spin Density Approximation

So far, no approximations have been made. The density functional formalism, outlined in the previous sections, could in principle reproduce all ground state properties of any complex many-electron system exactly, if the exchange correlation energy E_{xc} was known. Unfortunately, no explicit representation of this functional, that contains all many-body effects, has been found yet. Thus, approximations to E_{xc} have to be used. The most widely used and very successful approximation is the local spin density approximation (LSDA). The underlying idea is very simple. At each point of space, E_{xc} is approximated locally by the exchange correlation energy of a homogeneous electron gas with the same electron and magnetization density. Hence, the approximate functional E_{xc} is of the form

$$E_{xc}[n(\mathbf{r}), |\mathbf{m}(\mathbf{r})|] = \int n(\mathbf{r})\epsilon_{xc}(n(\mathbf{r}), |\mathbf{m}(\mathbf{r})|)\, d^3r. \tag{2.21}$$

It is important to note that ϵ_{xc} is not a functional, but a function of $n(\mathbf{r})$ and $|\mathbf{m}(\mathbf{r})|$ at a particular point of space. As a consequence of its local definition, ϵ_{xc} and thus E_{xc} depend only of the magnitude of the magnetization. This, in terms, leads to the fact that $\mathbf{B}_{xc}(\mathbf{r})$ and $\mathbf{m}(\mathbf{r})$ do always have the same direction. Therefore, the exchange correlation potential and magnetic field derived from (2.21) become

$$\begin{aligned} V_{xc}(\mathbf{r}) &= \epsilon_{xc}(n(\mathbf{r}), |\mathbf{m}(\mathbf{r})|) + n(\mathbf{r})\frac{\delta\epsilon_{xc}(n(\mathbf{r}), |\mathbf{m}(\mathbf{r})|)}{\delta n(\mathbf{r})} \\ \mathbf{B}_{xc}(\mathbf{r}) &= n(\mathbf{r})\frac{\delta\epsilon_{xc}(n(\mathbf{r}), |\mathbf{m}(\mathbf{r})|)}{\delta|\mathbf{m}(\mathbf{r})|}\hat{\mathbf{m}}(\mathbf{r}). \end{aligned} \tag{2.22}$$

Using the LSDA, the Kohn-Sham equations take exactly the same form as the Hartree equations, and they are no more difficult to solve. In particular, they are far easier to deal with than the Hartree-Fock equations because of the local effective potential. Intuitively one should expect that the LSDA is valid only for slowly varying densities. Nevertheless, it has been applied successfully to inhomogeneous systems.

Explicit parameterizations of ϵ_{xc} can be obtained for example from Hartree-Fock calculations for the homogeneous electron gas. Of course, such calculations do only take into account the exchange effects, but neglect correlation.

Modern parameterizations of ϵ_{xc} are based on quantum-mechanical many-body calculations. Most commonly used are the parameterizations of Barth and Hedin [50] and Moruzzi, Janak and Williams [35] which have been obtained applying the random phase approximation (RPA) and the parameterization of Perdew and Zunger [41] which is, in a certain sense, a mixture of the previous two.

It should be mentioned however, that LSDA is not the solution for all problems of the solid state physics. For the systems with charge density strongly varying over space the generalized gradient approximation (GGA) is more appropriate than LSDA. Other corrections, to apply where necessary, are self-interaction correction (SIC) [41, 47], orbital-polarization corrections [43], LDA+U [3, 44], and exact exchange [46].

2.4 Solving the KS equations

The solution of the KS equations is represented in form of a series:

$$\psi_i(\mathbf{r}) = \sum_n a_n \phi_n(\mathbf{r}) \tag{2.23}$$

where $\{\phi_n\}$ is a certain basis set. In the following the basis set, which is used in this work, is constructed. The plane waves, which are used in this construction, offer a large number of advantages including their simplicity. Furthermore, the plane waves are orthogonal, do not anticipate the special form of the solution and are solutions of the Schrödinger equation for a constant potential. However, in a crystalline material a potential can be approximated with a constant only in the interstitial, far enough from the nuclei. Around the nuclei spherical harmonics together with the radial solution of the Schrödinger equation become more suitable to represent $\psi_i(\mathbf{r})$. Slater [45] had the idea to augment each plane wave into the solution described by the Schrödinger equation for the spherical potential.

2.4.1 APW basis functions

In this method and in further modifications of it, like linearized APW (LAPW) and full-potential LAPW (FLAPW), the crystal structure is partitioned into spheres around the atoms (muffin-tins) and the space in between (the interstitial). The effective potential V_{eff} is approximated with a spherical part $V_{eff}(r)$ in the muffin-tins and with a constant in the interstitial. Then a particular solution $\psi_i(\mathbf{r}, \mathbf{k})$ of the KS equations (2.14) is sought after in the form:

$$\begin{aligned} \psi_i(\mathbf{r}, \mathbf{k}) &= \sum_{\mathbf{G}} a_{\mathbf{G}} \phi_{\mathbf{G}}(\mathbf{r}, \mathbf{k}) \\ \phi_{\mathbf{G}}(\mathbf{r}, \mathbf{k}) &= \begin{cases} e^{i(\mathbf{G}+\mathbf{k})\mathbf{r}} & \mathbf{r} \in \text{interstitial} \\ \sum_{lm} A_{lm}^{\mu\mathbf{G}} u_l(r) Y_{lm}(\hat{\mathbf{r}}) & \mathbf{r} \in \text{muffin-tin } \mu \end{cases} \end{aligned} \tag{2.24}$$

where $\mathbf{G}$ is the reciprocal lattice vector and $\mathbf{k}$ is the Bloch vector. The cut-off K_{max} for the norm of the vector $\mathbf{K} = \mathbf{G} + \mathbf{k}$ determines the number of the plane waves used in the representation 2.24. The coefficients $A_{lm}^{\mu\mathbf{G}}$ are determined from the condition of continuity of the wave function at the muffin-tin boundary. Function $u_l(r)$ is the solution of the radial Schrödinger equation:

$$\left(\frac{\hbar^2}{2m} \frac{\partial^2}{\partial r^2} + \frac{\hbar^2}{2m} \frac{l(l+1)}{r^2} + V(r) - E \right) r u_l(r) = 0, \tag{2.25}$$

containing the energy parameters E: $u_l(\mathbf{r}) \equiv u_l(\mathbf{r}, E)$.

Inserting ansatz (2.24) in the KS equations (2.14) results in a linear, easily solvable eigenvalue problem in case of fixed E. However, fixed energy parameters E do not provide enough variational freedom to describe the wave function and eigenvalues of the electrons with sufficient accuracy in the reasonable energy interval. An accurate description of the system can only be achieved by setting E to the band energies, not known *a priori*. On the other hand, in order to find the energy parameters self-consistently, a non-linear and computationally highly demanding problem is to be solved. This problem can be cured on the base of the LAPW method, described in the next section.

2.4.2 LAPW basis functions

The idea of the LAPW method, first proposed by O. K. Andersen [1], is to linearize radial functions $u(\epsilon_i, \mathbf{r})$ around a certain energy parameter value $\epsilon_i = \hat{E}_l$ using Taylor expansion:

$$u_l(\epsilon_i, r) = u_l(\hat{E}_l, r) + (\epsilon_i - \hat{E}_l)\frac{\partial}{\partial \epsilon} u_l(\epsilon_i, r)|_{\epsilon_i = \hat{E}_l} + O((\epsilon_i - \hat{E}_l)^2). \qquad (2.26)$$

The error of this expansion $O(\epsilon_i - \hat{E}_l)^2$ is of second order and therefore the error in the energy is of the order 4. According to this idea the basis functions in the muffin-tins are modified in the following way:

$$\phi_{\mathbf{G}}(\mathbf{r}, \mathbf{k}) = \sum_{lm} (A_{lm}^{\mu \mathbf{G}} u_l(r) + B_{lm}^{\mu \mathbf{G}} \dot{u}_l(r)) Y_{lm}(\hat{\mathbf{r}}). \qquad (2.27)$$

The coefficients $A_{lm}^{\mu \mathbf{G}}$ and $B_{lm}^{\mu \mathbf{G}}$ are determined from the continuity of the wave functions $\phi_{\mathbf{G}}(\mathbf{r}, \mathbf{k})$ and their derivatives with respect to r on the muffin-tin boundaries. The $\dot{u}(r) := \frac{\partial u(E_l, r)}{\partial E_l}$ can be calculated by differentiating (2.25) with respect to the energy. By differentiating the scalar product $\langle u(r)|u(r)\rangle$ with respect to the energy it is easy to show that $u(r)$ and $\dot{u}(r)$ are orthogonal. It follows that the LAPW basis functions are orthogonal inside the muffin-tins since the spherical harmonics are also orthogonal.

LAPW solves the problem of variational freedom that persists for APW basis functions. However, further substantial improvements of this method are possible. The APW and LAPW methods use an approximate form of the potential, i.e. it was assumed to be spherically symmetric in the muffin-tins and constant in the interstitial. This is an appropriate approximation for metals in bulk, but is not applicable for the materials in open structures like semiconductors and surfaces, where the difference between the true potential

and this approximation is too large. The need for a natural treatment of systems, where non-spherical contributions to the potential are essential, leads us to the full-potential LAPW (FLAPW) method.

2.4.3 FLAPW basis

In the FLAPW method no assumptions on the shape of the potential are made and a more general spatial representation is considered:

$$V(\mathbf{r}) = \begin{cases} \sum_{\mathbf{G}} V_i^{\mathbf{G}} e^{i\mathbf{G}\mathbf{r}} & \mathbf{r} \in \text{interstitial} \\ \sum_{lm} V_{MT}^{lm}(r) Y_{lm}(\theta, \phi) & \mathbf{r} \in \text{muffin-tin} \end{cases} \tag{2.28}$$

instead of

$$V(\mathbf{r}) = \begin{cases} V_i^0 = const. & \mathbf{r} \in \text{interstitial} \\ V_{MT}^0(r) & \mathbf{r} \in \text{muffin-tin.} \end{cases} \tag{2.29}$$

Because of the limited computational capacities only a finite number of elements from the infinite series over $\mathbf{G}$ and l in (2.28) can be considered. In (2.28) all elements with $|\mathbf{G}| < G_{max}$ and $l < l_{max}$ are used, where G_{max} and l_{max} are some cut-off parameters. Still, the large number of coefficients can be considerably reduced by exploiting the symmetry of the system. The corresponding symmetry group consists of N_{op} operations $\{\mathbf{R}|\mathbf{t}\}$, where $\mathbf{R}$ is a rotation and $\mathbf{t}$ is a non-lattice vector translation. Based on this symmetry group the plane waves that are associated via $\{\mathbf{R}|\mathbf{t}\}$ can be joined together in so-called star functions:

$$\phi_s = \frac{1}{N_{op}} \sum_{\mathbf{R}} e^{i\mathbf{R}\mathbf{G}(\mathbf{r}+\mathbf{t})} \tag{2.30}$$

with the sum over all reciprocal lattice vectors $\mathbf{G}$, that are connected through the rotation $\mathbf{R}$. Analogously, we combine the spherical harmonics into the lattice harmonics:

$$K_\nu^\alpha(\hat{\mathbf{r}}_\alpha) = \sum_m c_{\nu,m}^\alpha Y_{lm}(\hat{\mathbf{r}}_\alpha), \tag{2.31}$$

where α denotes the atomic site. One should keep in mind that the point-group symmetry is in general different from site to site. The index ν accounts for the fact, that there is in general more than one lattice harmonic for any given α and l. Finally, every quantity, like charge density or potential, that possess the symmetry of the crystal, can be represented in terms of star functions and lattice harmonics:

$$n(\mathbf{r}) = \begin{cases} \sum_s n_s \phi_s(\mathbf{r}) & \mathbf{r} \in \text{interstitial} \\ \sum_\nu n_\nu^\alpha(r) K_\nu^\alpha(\hat{\mathbf{r}}_\alpha) & \mathbf{r} \in \text{muffin-tin } \alpha. \end{cases} \tag{2.32}$$

In this way the number of coefficients that have to be stored in computer memory is drastically reduced due to the fact that every single star function and lattice harmonic contain terms with coefficients in the expansion (2.28), which are equal, or connected to each other by phase factors, defined by the symmetry basis once at the beginning of the calculation.

2.4.4 Surfaces

In the scanning tunneling microscopy (STM) experiments simulated in the main part of this work, the electronic and magnetic structure of the sample surface can be measured. In spite of the disrupted periodicity perpendicular to the surface, nevertheless, it is possible to simulate periodic boundary conditions based on a super-cell approach. In this case the periodicity perpendicular to the surface is restored by choosing an appropriate unit cell consisting of several atomic layers and a separating vacuum layer, thick enough to prevent adjacent surfaces from interacting. The super-cell approach as described requires a large number of plane waves to achieve sufficient accuracy. An efficient and elegant scheme, originally proposed by Krakauer et al. [26], allows to overcome difficulties imposed by the super-cell approach and to reduce the computational effort drastically. The space partitioning and the unit cell in this method are shown in Fig. 2.1. The film now consists of some atomic layers, typically up to 20, and is terminated on both sides by semi-infinite vacuum. The vacuum stretches from $-\infty$ to $-D/2$ and from $D/2$ to ∞. An auxiliary parameter $\bar{D}$ ($\bar{D} > D$) helps to generate a set of reciprocal vectors and corresponding plane-waves. The inner film space is divided according to the bulk-case into the muffin-tins and interstitial regions, preserving two-dimensional periodicity.

According to the new geometry an appropriate set of basis functions has to be considered. Essentially for APW-based approaches, plane waves are still used to represent the basis functions in the interstitial region (2.24). While the two-dimensional periodicity and symmetries are preserved, modifications in the basis functions are required due to the presence of the vacuum region. Consequently, a generalized wave vector is decomposed into three parts: two parallel ($\mathbf{G}_\parallel$, $\mathbf{k}_\parallel$) and one perpendicular $\mathbf{G}_\perp$ to the surface.

$$\phi_{\mathbf{G}_\parallel}(\mathbf{k}_\parallel, \mathbf{r}) = e^{i(\mathbf{G}_\parallel + \mathbf{k}_\parallel)\mathbf{r}_\parallel} e^{i\mathbf{G}_\perp z}, \tag{2.33}$$

where $\mathbf{G}_\parallel$, $\mathbf{k}_\parallel$ are the two-dimensional reciprocal lattice vector and the Bloch vector, $\mathbf{r}_\parallel$ is the corresponding in-plane part of $\mathbf{r}$ and $\mathbf{G}_\perp = \frac{2\pi n}{D}$ is the z-reciprocal vector. As $\phi_{\mathbf{G}_\parallel}(\mathbf{k}_\parallel, \mathbf{r})$ form a basis only inside the region with $|z| < D/2$, the choice of $\bar{D} > D$ seems to be arbitrary. This is, however,

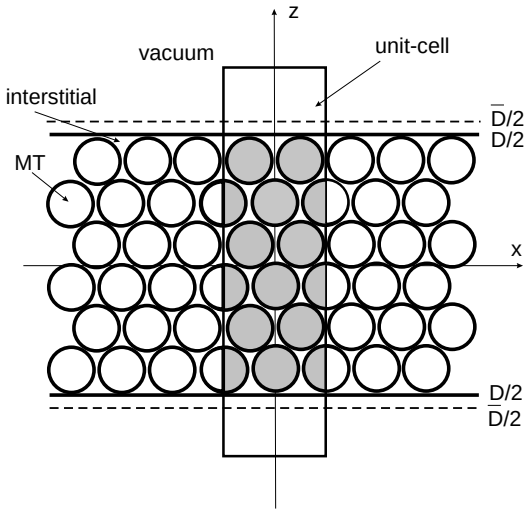

Figure 2.1: A unit cell contains a finite number of lattice planes in z-direction and is terminated on both sides by a semi-infinite vacuum region. The muffin-tin spheres are positioned at the atomic sites and the interstitial stretches out between $-D/2$ and $D/2$. The reciprocal vectors in z-direction are generated by $\bar{D}$.

only partly true as the span of the plane-wave vacuum boundary values is important for the variational flexibility of the basis and the optimal choice of the difference $(\bar{D} - D)$ can be established numerically (for more details see [28]).

The basis in the muffin-tins preserves the general shape of (2.27) and can be rewritten in terms of the two-dimensional wave- and Bloch-vectors as:

$$\phi_{\mathbf{G}_\parallel,G_\perp}(\mathbf{k}_\parallel,\mathbf{r}) = \sum_{lm}\left(A_{lm}^{\mu\mathbf{G}}(\mathbf{k}_\parallel)u_l(r) + B_{lm}^{\mu\mathbf{G}}(\mathbf{k}_\parallel)u_l(r)\right)Y_{lm}(\hat{\mathbf{r}}). \tag{2.34}$$

The basis functions in the vacuum are defined similarly to the muffin-tin basis wave functions, namely consisting of two-dimensional plane waves $e^{i(\mathbf{G}_\parallel+\mathbf{k}_\parallel)\mathbf{r}_\parallel}$ and a z-dependent part u, which is a solution of the one-dimensional Schrödinger equation:

$$(-\frac{\hbar^2}{2m}\frac{\partial^2}{\partial z^2} + V(z) - E_{vac} + \frac{\hbar^2}{2m}(\mathbf{G}_\parallel + \mathbf{k}_\parallel)^2)u_{\mathbf{G}_\parallel}(\mathbf{k}_\parallel, z) = 0. \tag{2.35}$$

From this equation the energy derivative $\dot{u}_{\mathbf{G}_\parallel}(\mathbf{k}_\parallel, z)$ can be easily evaluated. The resulting vacuum part of the basis functions reads:

$$\begin{aligned}\phi_{\mathbf{G}_\parallel,G_\perp}(\mathbf{k}_\parallel,\mathbf{r}) = (&A_{\mathbf{G}_\parallel,G_\perp}(\mathbf{k}_\parallel)u_{\mathbf{G}_\parallel}(\mathbf{k}_\parallel, z) + \\ &B_{\mathbf{G}_\parallel,G_\perp}(\mathbf{k}_\parallel)\dot{u}_{\mathbf{G}_\parallel}(\mathbf{k}_\parallel, z))e^{i(\mathbf{G}_\parallel+\mathbf{k}_\parallel)\mathbf{r}_\parallel}.\end{aligned} \tag{2.36}$$

Equation (2.33) in the interstitial, Eq. (2.34) in the muffin-tins and Eq. (2.36) in the vacuum form the FLAPW basis set in the film-geometry. This basis set is further used for expanding the solutions of the KS-equations.

2.4.5 The Generalized Eigenvalue Problem

Substituting the expansion $\psi_i(\mathbf{r},\mathbf{k}) = \sum_{\mathbf{G}} a^i_{\mathbf{G}} \phi_{\mathbf{G}}(\mathbf{r},\mathbf{k})$ in (2.14) yields:

$$\sum_{\mathbf{G}} a^i_{\mathbf{G}} \mathcal{H}\phi_{\mathbf{G}}(\mathbf{r},\mathbf{k}) = \epsilon_i \sum_{\mathbf{G}} a^i_{\mathbf{G}} \phi_{\mathbf{G}}(\mathbf{r},\mathbf{k}). \tag{2.37}$$

Scalar multiplication of this equation from the left with $\phi_{\mathbf{G}'}(\mathbf{r},\mathbf{k})$ leads to:

$$\sum_{\mathbf{G}} a^i_{\mathbf{G}} \langle \phi_{\mathbf{G}'}(\mathbf{r},\mathbf{k}) | \mathcal{H} | \phi_{\mathbf{G}}(\mathbf{r},\mathbf{k}) \rangle = \epsilon_i \sum_{\mathbf{G}} a^i_{\mathbf{G}} \langle \phi_{\mathbf{G}'}(\mathbf{r},\mathbf{k}) | \phi_{\mathbf{G}}(\mathbf{r},\mathbf{k}) \rangle. \tag{2.38}$$

This equation can be rewritten in matrix form:

$$(\mathbf{H} - \epsilon_i \mathbf{S}) a^i_{\mathbf{G}} = 0, \tag{2.39}$$

where the overlap matrix

$$\mathbf{S} := \int \phi^*_{\mathbf{G}}(\mathbf{r},\mathbf{k}) \phi^*_{\mathbf{G}'}(\mathbf{r},\mathbf{k}) \tag{2.40}$$

is in general only hermitian, but not diagonal. The equation (2.39) to be solved, is a so-called generalized eigenvalue problem, which can be transformed to a conventional eigenvalue problem using Cholesky factorization applied to the overlap matrix. For a given size N of the matrices in the eigenvalue problem, the time required for its solution scales like N^3, making it by far the most computationally demanding part of the whole algorithm. It is highly desirable, therefore, to have an efficiently constructed basis set, so that the smallest possible matrix size N is sufficient to describe the system accurately.

2.5 Relaxations

In the Born-Oppenheimer approximation the atomic nuclei are regarded as point charges with fixed positions $\mathbf{R}_\nu$. The energy functional still depends on those $\mathbf{R}_\nu$. Thus relaxation of the system means minimizing the ground state energy with respect to $\mathbf{R}_\nu$. To minimize the ground state energy we calculate the corresponding force on a nucleus α:

$$\begin{aligned} F_\alpha = -\nabla_\alpha \langle \Psi_0 | H | \Psi_0 \rangle \quad = \\ -\langle \Psi_0 | \nabla_\alpha H | \quad \Psi_0 \rangle - \langle \nabla_\alpha \Psi_0 | H | \Psi_0 \rangle - \quad \langle \Psi_0 | H | \nabla_\alpha \Psi_0 \rangle, \end{aligned} \tag{2.41}$$

with Ψ_0 being the ground state wave function. The first term in (2.41) is called the Hellmann-Feynman force [16]. The Hellmann-Feynman theorem states that the second and third terms vanish in case the basis used for the expansion of the single particle wave function is complete, which is not the case for the FLAPW basis set. Thus it is necessary to include the so-called incomplete basis set correction in the force calculation, first introduced by Pulay [42]. which arises from the gradient of the wave function on nuclei positions. The exact form of this correction is calculated in [55].

Chapter 3

Scanning Tunneling Microscopy

The scanning tunneling microscope (STM) is an instrument, that allows to study surfaces with high lateral resolution by using the quantum mechanical tunnel effect. The STM setup basically consists of a sharp metallic tip (the probe) and a sample surface. Usually the sample is parallel to the xy-plane with the tip at a vertical distance of about 3-10 Å. The tip can be moved with a high accuracy in all three dimensions with piezo actuators. Due to the small distance between tip and sample electrons can tunnel. By applying a voltage between the tip and the sample their Fermi energies shift against each other and the tunneling current can be measured as a function of the applied voltage and the lateral tip position. In first approximation the tunneling current decreases exponentially with the tip-sample distance. This implies that the atoms of the sample which lie directly under the tip apex contribute mainly to the tunneling current. In the following sections of this chapter some basics of the theory of STM and of the simulation of STM results are presented. The description in this chapter is restricted to the elastic one-particle tunneling. This means that possible interactions among the electrons and between electrons and quasi-particles, like phonons, are neglected. More details on the subject are given in [4, 9, 10, 52].

3.1 The Perturbational Approach

A schematic representation of an STM tunnel junction is shown in Fig. 3.1. The tip and a semiconducting sample are separated by vacuum. The Fermi energies E^F_{tip} of the tip and E^F_{sam} of the sample are shifted by eU. The density of states of the tip is assumed to be nearly constant. Electrons in occupied states of the tip can tunnel into empty states of the sample. The transmission coefficient depends on the distance between tip and sample and the applied

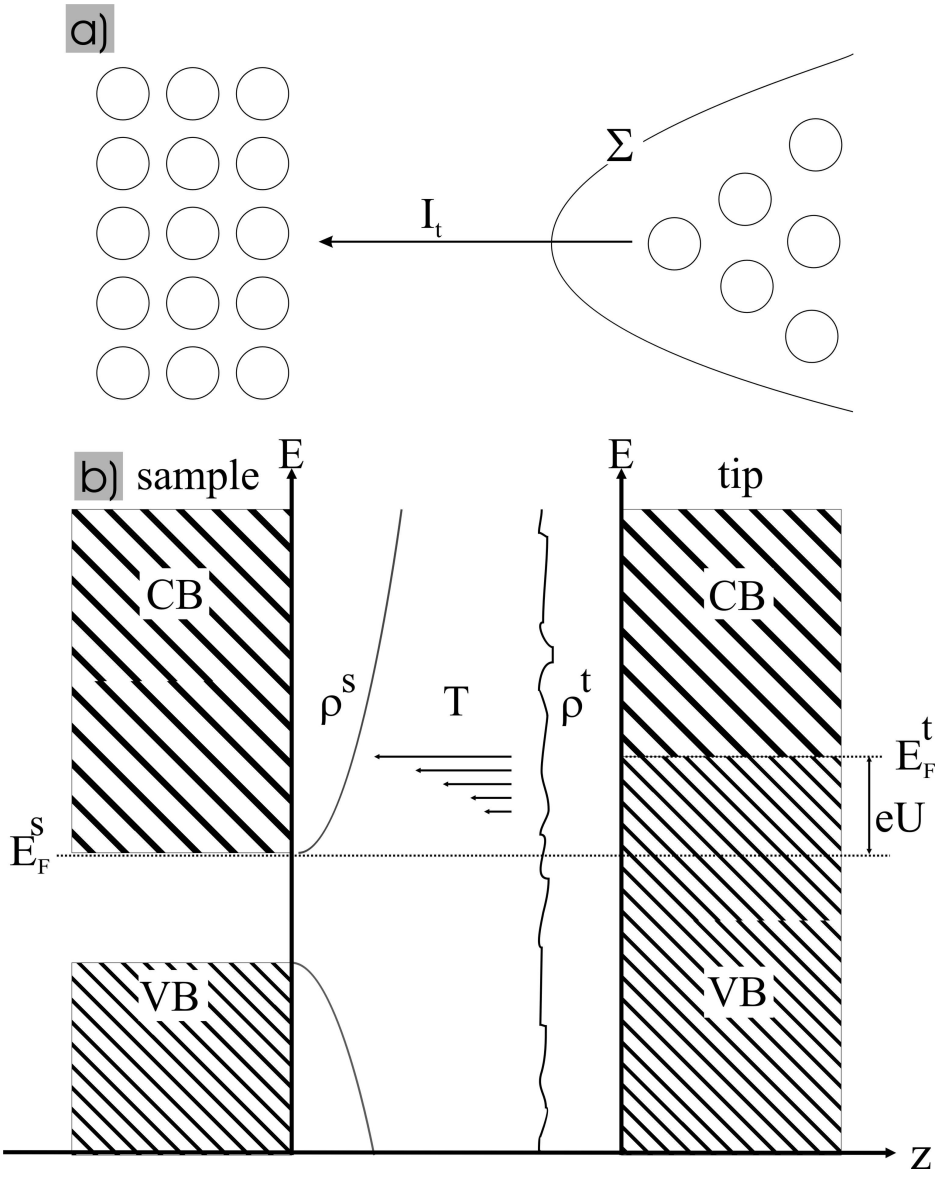

Figure 3.1: (a) Schematic representation of a sample and an ideal tip with only one apex atom. The space is devided into a tip part and a sample part by an arbitrarily formed surface Σ. (b) The electronic situation of the metallic tip close to a semiconducting surface is shown. The applied voltage U shifts the Fermi energies by the value eU. The DOS of the tip is assumed to be nearly constant. The electrons tunnel from the occupied states of the tip into the empty states of the semiconducting sample.

voltage. The tunneling current I_t can be calculated with a perturbational approach, for the first time suggested for an arbitrary tunnel junction by Bardeen [4] and then modified for applying to STM by Tersoff, Hamann and Chen [48, 49, 9].

Bardeen considered the tunneling current as the independend transfer of electrons across the tunneling barrier described by the single-electron Schrödinger equation:

$$i\hbar\frac{\partial\Psi(\mathbf{r},t)}{\partial t} = \left(-\frac{\hbar^2}{2m}\nabla^2 + V(\mathbf{r})\right)\Psi(\mathbf{r},t). \tag{3.1}$$

$V(\mathbf{r})$ is the electrostatic potential energy that an electron would have inside of STM. The idea of Bardeen was to exploit the knowledge we might have of the tip and the sample as two separate systems. He defined tip- and sample-Hamiltonians as :

$$H_{sam}\Psi(\mathbf{r}) = \left(-\frac{\hbar^2}{2m}\nabla^2 + V_{sam}(\mathbf{r})\right)\Psi(\mathbf{r}) \tag{3.2}$$

$$H_{tip}\Psi(\mathbf{r}) = \left(-\frac{\hbar^2}{2m}\nabla^2 + V_{tip}(\mathbf{r})\right)\Psi(\mathbf{r}), \tag{3.3}$$

with the potentials V_{tip}, V_{sam} defined by two conditions:

$$V_{tip}(\mathbf{r}) * V_{sam}(\mathbf{r}) = 0 \tag{3.4}$$

$$V_{tip}(\mathbf{r}) + V_{sam}(\mathbf{r}) = V(\mathbf{r}) \tag{3.5}$$

The eigenstates of the sample- and tip-Hamiltonians (3.2), (3.3) are tip states ψ_{tip} and sample states ψ_{sam} respectively. The tunneling current is the transfer of electrons from tip states to sample states or reverse governed by the Schrödinger equation (3.1). An electron initially in the sample state $\Psi(\mathbf{r},0) = \psi_{sam}$ evolves with the time t. With the evolution determined only by the sample Hamiltonian (3.2) its wave function would become $\Psi(\mathbf{r},t) = \psi_{sam}\exp\left(-\frac{iE_{sam}t}{\hbar}\right)$.

To take into account the influence of the tip, an additional term is used to represent $\Psi(\mathbf{r},t)$:

$$\Psi(\mathbf{r},t) = \psi_{sam}\exp\left(-\frac{iE_{sam}t}{\hbar}\right) + \sum_{\nu} c_\nu(t)\psi^{\nu}_{tip}\exp\left(-\frac{iE^{\nu}_{tip}t}{\hbar}\right). \tag{3.6}$$

The additional term is the sum over all bound states ψ^{ν}_{tip} with eigenvalues E^{ν}_{tip} of the tip Hamiltonian.

Inserting this representation in (3.1) yields a set of differential equations for c_ν, that can be solved like described in [7, 19], with the result:

$$c_\nu = \frac{\exp(-itE_{sam}/\hbar) - \exp(-itE^\nu_{tip}/\hbar)}{E_{sam} - E^\nu_{tip}} \langle \psi^\nu_{tip} | V_{tip} | \psi_{sam} \rangle \tag{3.7}$$

The probability of the electron to be in the state ψ^ν_{tip} is calculated from the square of the expansion coefficients $|c_\nu|^2$. The transition rate from state ψ_{sam} into ψ^ν_{tip} is then defined as:

$$w = \frac{d}{dt}|c_\nu|^2. \tag{3.8}$$

Due to the symmetrical treatment of the tip and the sample to this point w also gives the transition rate from the given tip state ψ^ν_{tip} into ψ_{sam}. Inserting c_ν in this definition and considering only elastic tunneling yields Fermi's Golden Rule:

$$\begin{aligned} w &= \frac{2\pi}{\hbar}\delta(E^\nu_{tip} - E_{sam})|M|^2 \\ M &= \langle \psi^\nu_{tip} | V_{tip} | \psi_{sam} \rangle. \end{aligned} \tag{3.9}$$

The delta function annihilates all the transitions with $E_{sam} \neq E^\nu_{tip}$, so that only elastic tunneling processes are considered. The occupation of the states by the electrons at the temperature T is described by the Fermi-Dirac distribution:

$$f(E - E_F) = \left(1 + \exp\left(\frac{E - E_F}{k_B T}\right)\right). \tag{3.10}$$

By taking into account all possible initial and final states we get for the tunneling current I_t:

$$\begin{aligned} I_t &= \frac{4\pi e}{\hbar} \sum_{\nu\mu} \left(f(E^\mu_{sam} - E_{F,sam}) - f(E^\nu_{tip} - E_{F,tip}) \right) \times \\ &\times \quad |M|^2 \delta(E^\nu_{tip} - E^\mu_{sam} - eV) \end{aligned} \tag{3.11}$$

with the Fermi function $f(E)$ and the tunneling matrix element M which determines the probability for an electron to pass from the sample state ψ^μ_{sam} into the tip state ψ^ν_{tip}. Bardeen [4] calculates the tunneling matrix element like:

$$M[\psi_{tip}, \psi_{sam}] = -\frac{\hbar^2}{2m} \int_\Sigma \psi^*_{tip} \nabla \psi_{sam} - \psi_{sam} \nabla \psi^*_{tip} d\mathbf{S}, \tag{3.12}$$

where the integration is performed over the arbitrary surface Σ separating tip and sample (compare Fig. 3.1). In the original work [4], where unperturbed potentials are considered, the corresponding error is minimized by choice of the surface equidistant between the two electrodes.

3.2 Tersoff-Hamann Model

Now it is possible to calculate the tunneling current in an STM setup with equations (3.11), (3.12) in case the exact electronic structure of the sample and the tip is known. The FLAPW method as described in sec. 2.4 gives access to the electronic structure of the sample whereas for the tip the situation is slightly more complicated. The main problem is that the atomic structure of any real tip is unknown. The symmetry of the tip is in general so low, that the exact calculation of the electronic structure of the tip remains a very demanding problem even with knowledge of the atomic structure available. Thus, simplifying assumptions have to be made. For the interpretation of STM experiments the Tersoff-Hamann model of the tip has been used very successfully. This model is based on two assumptions, firstly that the tip has one apex atom in the s-state and secondly that the tunneling happens in the limits of low temperature and low voltage.

To evaluate the tunneling matrix element (3.12) we need the tip wave function ψ_{tip} on the surface Σ, located somewhere in the vacuum gap between the electrodes. This means that the ψ_{tip} has to satisfy the Schrödinger equation in the vacuum:

$$(\nabla^2 - \kappa^2)\psi_{tip}(\mathbf{r}) = 0 \tag{3.13}$$

with the decay constant κ. $\psi_{tip}(\mathbf{r})$ can be expanded into the spherical harmonics:

$$\psi_{tip}(\mathbf{r}) = \sum a_{lm} f_l(\kappa\rho) Y_{lm}(\theta, \phi), \tag{3.14}$$

with $\rho = |\mathbf{r} - \mathbf{R}_t|$ where $\mathbf{R}_t$ is the position of the apex atom. Inserting ansatz (3.14) into equation (3.13) results in the spherical modified Bessel functions of the second kind:

$$k_l(u) = (-1)^l u^l \left(\frac{1}{u}\frac{d}{du}\right)^l \frac{e^{-u}}{u} \tag{3.15}$$

with $u = \kappa\rho$, for the radial part f_l. So the tip wave function for an s-orbital has the form:

$$\psi_{tip}(\mathbf{r}) = C k_0(\kappa\rho) = C\frac{e^{-\kappa\rho}}{\kappa\rho}. \tag{3.16}$$

It is crucial for the following considerations that the wave function of an s-orbital at the apex atom is proportional to the Greens function of the Schrödinger equation in vacuum. Substituting (3.16) into (3.12) and using the Greens theorem we obtain:

$$M[\psi_{tip},\psi_{sam}] = \frac{2\pi C\hbar^2}{\kappa m}\int_{\Theta_T} G(\mathbf{r}-\mathbf{R}_t)\nabla^2\psi_{sam} - \psi_{sam}\nabla^2 G(\mathbf{r}-\mathbf{R}_t)d\mathbf{V} = \\ = \frac{2\pi C\hbar^2}{\kappa m}\psi_{sam}(\mathbf{R}_t), \tag{3.17}$$

with Θ_T denoting the volume of the tip. Using this matrix element together with (3.11) leads to the following expression for the tunneling current:

$$\lim_{T=0} I(\mathbf{R}_t,V) = \lim_{T=0}\left[\frac{16\pi^3 C^2\hbar^3 e}{\kappa^2 m^2}\times \right. \\ \left.\times\int \rho_{sam}(\mathbf{R}_t,E)\left[f(E-E_{F,sam}) - f(E+eV-E_{F,tip})\right]dE\right] = \tag{3.18}$$
$$= \frac{16\pi^3 C^2\hbar^3 e}{\kappa^2 m^2}\int_{E_F}^{E_F+eV}\rho_{sam}(\mathbf{R}_t,E)dE$$

with the local density of states (LDOS) defined as:

$$\rho(\mathbf{r},\epsilon) = \lim_{\Delta\epsilon\to 0}\sum_{E_\mu=\epsilon}^{\epsilon+\Delta\epsilon}|\psi_\mu(\mathbf{r})|^2\delta(\epsilon-E_\mu). \tag{3.19}$$

The tunneling current $I_t(V)$ (3.18) is proportional to the integrated LDOS of the sample under the additional constraint of a constant DOS of the tip. An immediate consequence of equation (3.18) is that $\frac{dI}{dV}\sim\rho_{sam}(\mathbf{R}_t,E)$. Three basic measurement modes of an STM directly connected with $I_t(V)$ and $\frac{dI}{dV}$ are described in the following section.

3.3 Measurement Modes

In an STM experiment, different kinds of measurements can be done. I will discuss here the constant current mode (CCM) that allows to measure the topography of the surface, the spectroscopic dI/dV mapping, and the full spatially resolved spectroscopy of a sample.

3.3.1 Constant Current Mode

In the CCM during the scanning of the xy-plane, a feedback system keeps the tunneling current I_t at a constant value. The tunneling current (3.18) depends exponentially on the distance between the tip and the surface, so by

doing small adjustments in the distance, I_t can be regulated very efficiently. The feedback loop keeps the tip on the surface, where $\int_{E_F}^{E_F+eV} \rho_s(\mathbf{R}_t, E)dE = const.$. Consequently, scanning in CCM gives only an approximate measurement of the surface topography. Features in the LDOS will also affect the measurement when scanning in CCM.

3.3.2 Spectroscopic dI/dV Mapping

According to equation (3.18) the dI/dV signal is directly proportional to the LDOS of the sample at the position of the tip. A map of the differential conductivity (dI/dV) is obtained simultaneously with a topography measurement. To get the dI/dV map a small modulation voltage with a frequency of a few kHz is superimposed on the bias voltage during the CCM measurement. With a frequency higher than the cut-off frequency of the feedback circuit this modulation does not have any influence on the CCM tracking. The lock-in technique allows to record the corresponding dI/dV signal.

3.3.3 Full spatially resolved spectroscopy

After positioning the tip with stabilization voltage V_{st} and stabilization current I_{st} at the point of measurement, the feedback of the system is switched off. Then the voltage of the tip is changed slowly from a starting to a final value. At the same time $I(V)$ and the dI/dV signal are recorded by means of lock-in technique. Spatially resolved spectroscopic information is obtained by repeating this procedure at every location (x, y) of the image frame. These full spectroscopy measurements take a longer time to record than dI/dV maps. The advantage of the full spectroscopy measurement is, that it gives the dI/dV signal for a complete voltage range without the additional influence of the change of a tip height.

3.4 Simulating Experiments

The tunneling current is kept constant in the CCM through the adjustment of the z coordinate of the tip. This means that an STM image in the CCM represents the Δz movement of the tip from the starting height z for every point $\mathbf{r}_\parallel$. The simulation gives access to the LDOS of the sample at every given point in the simulated space. This means that we can easily get the plots of the LDOS at the distance $z = const.$ from the surface. In the Tersoff-Hamann theory this corresponds to the change in the current ΔI_t for every

point $\mathbf{r}_\parallel$ if the feed-back of the tip is switched off. The connection between measured Δz movements and ΔI_t can be established with two assumptions:

- The tunneling current $I_t(\mathbf{r}_\parallel, z)$ for the tip movement in CCM can be linearized around some set-point value z_0.
- The change of $I_t(\mathbf{r}_\parallel, z)$ with z is independent of $\mathbf{r}_\parallel$.

The second assumption is justified because the decay rate κ depends to first approximation only on the energy of the tunneling electrons and the work function. Due to the exponential dependence of the transmission coefficient on the distance, the adjustment of the distance is normally ≈ 0.1 Å, whereas the tip-sample distance is between 3 Å and 10 Å. Consequently we expect that the linearization of $I_t(\mathbf{r}_\parallel, z(\mathbf{r}_\parallel))$ around z_0 works.

$$I_t(\mathbf{r}_\parallel, z(\mathbf{r}_\parallel)) = I_t(\mathbf{r}_\parallel, z_0) + dI_t(\mathbf{r}_\parallel, z_0). \tag{3.20}$$

Due to the constant current in CCM the change of the current is zero:

$$dI_t = \frac{\partial I_t}{\partial \mathbf{r}_\parallel}(\mathbf{r}_\parallel, z_0)d\mathbf{r}_\parallel + \frac{\partial I_t}{\partial z}(\mathbf{r}_\parallel, z_0)dz = 0 \tag{3.21}$$

The first term is $\Delta I_t(\mathbf{r}_\parallel)$ - the change of the current with $\mathbf{r}_\parallel$ while the z coordinate of the tip is kept fixed: $z = z_0$. The second term $\frac{\partial I_t}{\partial z}(\mathbf{r}_\parallel, z_0)$ is constant over $\mathbf{r}_\parallel$ due to the second approximation. This means

$$-\frac{\partial I_t}{\partial z}(z_0)dz = \Delta I_t(\mathbf{r}_\parallel). \tag{3.22}$$

Accounting for $\frac{\partial I_t}{\partial z}(z_0) < 0$ with $dz > 0$ leads to the equation:

$$dz(\mathbf{r}_\parallel) \sim \Delta I_t(\mathbf{r}_\parallel). \tag{3.23}$$

This equation connects the change in the vertical position of the tip during the CCM measurement with the change of the tunnelling current in case the vertical position of the tip would be kept constant. The latter can be simulated directly with the LDOS plots calculated at the distance z_0 from the surface.

Chapter 4

Geometry of Fe on InAs(110)

The idea of spin electronics (spintronics) inspired a lot of extensive experimental [36] and theoretical [13, 29] studies on magnetic semiconductors and semiconductor/ferromagnet hybrid systems. Promising results on the spin injection through the interface between magnetic material/semiconductor, depending on the symmetry, were reported in [54, 31]. Despite the multiplicity of these studies, the details of the interaction between a metal and a semiconductor are still unclear. Additionally, research on quantum confined structures attracts increasing attention in recent years [38, 32]. This chapter is focused on the geometry of Fe on InAs(110). The determination of the geometry is the most demanding part in the calculation. The relaxation of the Fe monolayer on InAs(110) is calculated at first to obtain a good first guess of the geometry of Fe chains on InAs(110).

4.1 Fe ML on InAs(110)

InAs is a III-V semiconductor that crystallizes in the cubic zinc-blende structure. This structure consists of two fcc sublattices that are shifted relative to each other by 1/4 of the cube diagonal. Each atom is bound to its four nearest neighbours of the other element. We calculated the lattice constant to 11.437 a.u., which is in good agreement with the experimentally found value of 11.46 a.u. (1 a.u.=0.529 Å). The unit cell of the InAs(110) surface, which contains atoms of both species, is shown in Fig. 4.1 (c).

The calculations are performed using DFT [22]. The exchange-correlation functional is formulated within the local spin-density approximation [40]. The Kohn-Sham equations are solved applying the full-potential linearized plane-wave (FLAPW) method, as realized in the FLEUR-code [53, 23]. For simulating the InAs(110) surface we use a slab geometry with five layers of

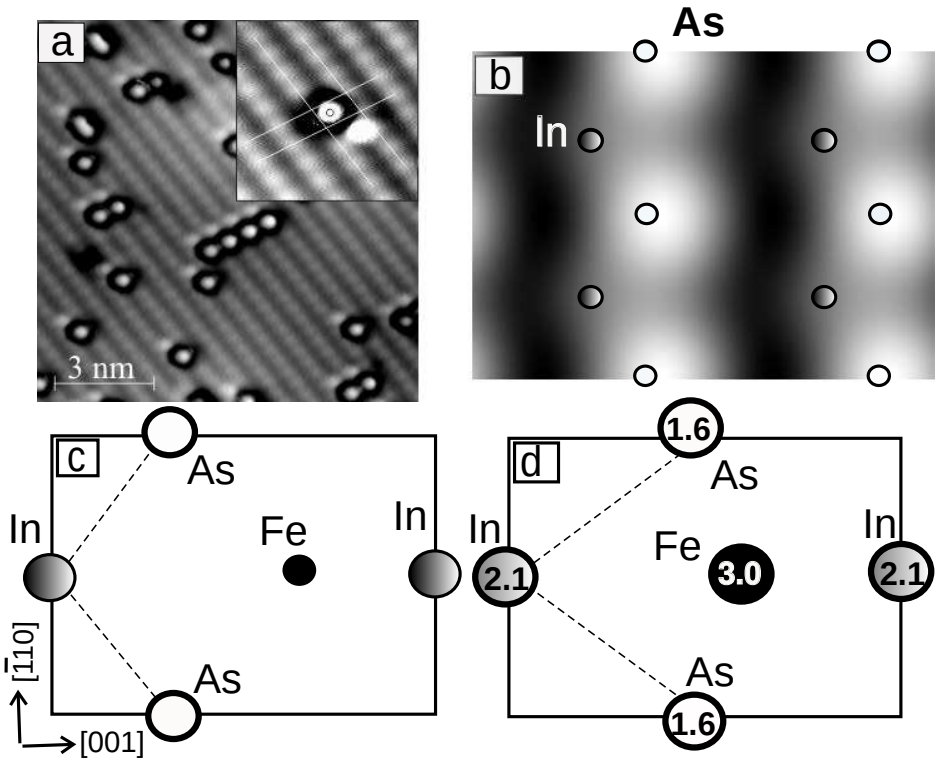

Figure 4.1: (**a**) STM constant-current image of InAs(110) covered with 7.5% Fe, $U = 50$ mV, $I = 200$ pA, $T = 8$ K; [33] (**b**) calculated constant-current image of the relaxed InAs(110) surface, $U = 50$ mV; (**c**) from (**a**) and (**b**) deduced position of the Fe-atom in the InAs(110) unit cell; (**d**) calculated position of Fe-atom in the InAs(110) unit cell after relaxation; The numbers on the atoms indicate the vertical relaxation in atomic units from the ideal bulk terminated position of the surface As.

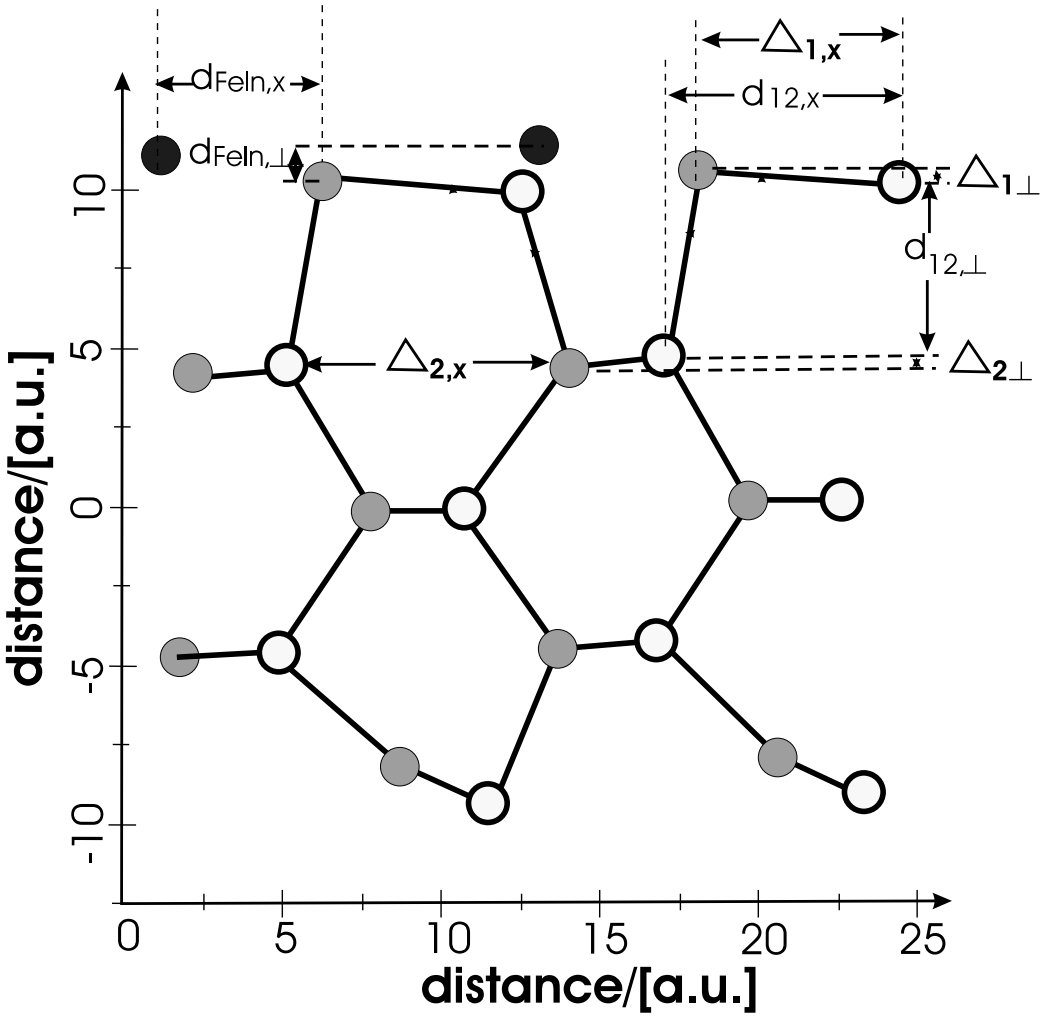

Figure 4.2: Side-view of calculated relaxed atomic positions at the InAs(110) surface covered with an Fe-monolayer. The lower half part shows the relaxation of the clean InAs(110) surface. Black circles mark the Fe-positions, gray the In- and white the As-positions. Tables 4.1 and 4.3 give the corresponding values of distances, bond lengths and angles.

InAs embedded in infinite vacua on both sides of the slab. Tests with five and nine atomic layer slabs of InAs show, that the energetically favorable structure is reproduced with sufficient accuracy using a five layer slab. Next, a Fe-monolayer with one Fe-atom per unit cell is placed on one side of the optimally relaxed InAs slab. For the optimization of the new configuration, the Fe-monolayer and the two adjacent layers of the InAs are allowed to relax. To prevent an overlap of the MT-spheres and at the same time to take into account the extension of the states at the atoms we choose the radii of the MTs to be 2.2 a.u. for the Fe, 2.0 a.u. for the In and 1.8 a.u. for the As. The wavefunctions are expanded into augmented plane waves with a maximum K-vector of $K_{max} = 3.9$ a.u.$^{-1}$, which amounts to 230 basis functions per atom. The basis functions in the MTs are expanded into radial functions and spherical harmonics with angular momenta up to $l = 8$. The BZ integration is carried out using 121 $k_{\|}$-points in the irreducible wedge of the two-dimensional BZ. The starting position for the relaxation of the Fe-atom is deduced as follows: We compare measured STM images of InAs(110) covered with submonolayers of Fe with calculated STM images of clean InAs(110) [14, 34]. Fig. 4.1(a) shows the measured image [33]. The atomic rows of one type of atoms are visible in the background. The bright spots surrounded by a black rim are the Fe atoms. The inset shows that the position of the Fe maxima is in between two atomic rows and slightly displaced towards one of them. Moreover, the Fe maxima are located exactly between two neighboring maxima inside the InAs rows [33]. The calculated image of the clean InAs(110) surface at the same voltage is displayed in Fig. 4.1 (b). The marked atomic centers of the In and the As atoms reveal that the protrusions in the constant-current image correspond to the As atoms. This is opposite to the conventional knowledge that cations (In) are imaged at positive voltage on III-V materials, but has its origin in the high energy position of the In dangling-bond state of 0.9 eV above the conduction band minimum and the fact that the surface As atoms are relaxed outwards [14, 34]. From comparison of Fig. 4.1 (a) and Fig. 4.1 (b) we deduce a lateral position of the Fe atom as displayed in Fig. 4.1 (c). The optimization process of this atomic structure led to the structure shown in Fig. 4.1 (d).

Fig. 4.2 shows a side-view of the InAs film after relaxation. The lower half of the film shows the relaxation without the Fe monolayer, while the relaxed structure with Fe is shown in the upper half. There, in contrast to the film without Fe, In and As are nearly at the same height. The In atom is even slightly higher (0.5 a.u.) than the As atom. The bond length between In and As in the uppermost layer as well as the bond length between the uppermost and the next layer of InAs are increased with respect to the relaxed

distance	unit	InAs bulk	InAs(110)	Fe/InAs(110)
a	[a.u.]	11.437		
$d_{\mathrm{FeIn},\perp}$	$[\frac{1}{2}a/\sqrt{2}]$			0.079
$d_{\mathrm{FeIn,x}}$	$[a]$			0.429
$\Delta_{1,\perp}$	$[a/\sqrt{2}]$	0.000	-0.164	0.056
$\Delta_{1,x}$	$[\frac{3}{4}a]$	1.000	1.033	0.632
$d_{12,\perp}$	$[\frac{1}{2}a/\sqrt{2}]$	1.000	1.118	1.241
$d_{12,x}$	$[\frac{1}{2}a]$	1.000	1.080	1.266
$\Delta_{2,\perp}$	$[\mathrm{a}/\sqrt{2}]$	0.000	-0.018	0.043
$\Delta_{2,x}$	$[\frac{3}{4}a]$	1.000	0.999	0.996

Table 4.1: Distances between the atoms at the clean relaxed InAs(110) surface and at the InAs(110) surface covered with one Fe-atom per unit cell according to the definitions in Fig. 4.2. The distances are expressed in units of the respective InAs bulk distances given in the second column.

InAs film without Fe. Table 4.1 and 4.3 give the corresponding values of distances and bond lengths for the clean relaxed InAs(110) and the relaxed InAs(110) covered with one Fe atom per unit cell. The results for the clean surface are in excellent agreement with other theoretical work on III-V semiconductors [14]. A strongly increased In-As bond length in the Fe/InAs(110) case shows that In-As-bonds are weakened in favor of the bonds between Fe and InAs.

In this section the geometry of 1 ML(Fe)/InAs(110) was calculated. The position of the Fe atom and the surface layer of InAs is used in the next section as a starting geometry for the calculation of the Fe chains on InAs(110).

4.2 Fe chains on InAs(110)

4.2.1 Computational details

To simulate the InAs(110) surface we used a slab of 5 layers InAs(110) with an Fe atom on top. To simulate Fe chains we put one Fe atom per two InAs(110) unit cells, so that the two-dimensional unit cell in the calculation consists of two InAs(110) unit cells along the [001] direction or along the $[1\bar{1}0]$, respectively. This model geometry leads to Fe chains along $[1\bar{1}0]$ (Fe$[1\bar{1}0]$/InAs(110)) with a distance between the chains of 22.87 a.u., as shown in Fig. 4.4, while chains along the [001] direction (Fe[001]/InAs(110))

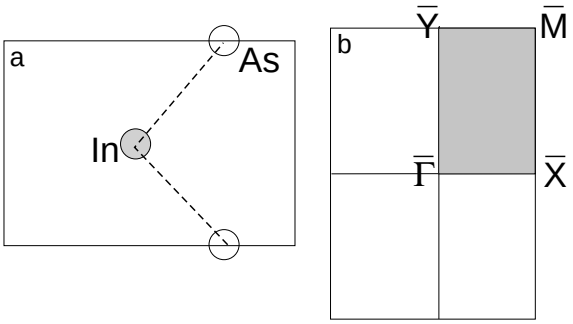

Figure 4.3: (a) InAs(110) unit cell. The bonds between In (grey) and As (white) are drawn as a dashed line. (b) The Brillouin zone of the InAs(110) with the irreducible part hashed grey.

have a distance of 16.16 a.u., as shown in Fig. 4.5. Compared to the Fe lattice constant of 3.5 a.u., these rather large distances rule out the interaction between the chains. The distance between Fe atoms in the chain is 8.16 a.u. in case of Fe[$1\bar{1}0$]/InAs(110) and 11.437 a.u. in case of Fe[001]/InAs(110). These distances are also rather large compared to the Fe lattice constant, so that we expect direct interaction between Fe atoms to be small. For the initial position of Fe and the surface layers of InAs, the geometry of Fe ML/InAs(110) is used. All three coordinates of the Fe atom and two surface layers of InAs were relaxed with the additional restriction that the mirror symmetry is preserved. For the 2DBZ sampling we used 12 k-points in the irreducible part of the 2DBZ shown in Fig. 4.3 (b). We started the calculation with a plane wave cut-off $K_{max} = 3.4$ a.u.$^{-1}$ and increased K_{max} during the convergence tests to $K_{max} = 3.8$ a.u.$^{-1}$, which corresponds to 230 plane waves per atom in the case of chains along [$1\bar{1}0$] and to 301 plane waves per atom in the case of chains along [001]. The radii of the muffin-tins (MTs) were set to 2 a.u. for the Fe and In atoms and to 1.8 a.u. for the As atoms. In case of Fe[001]/InAs(110) we had to increase the MTs radii to achieve sufficient accuracy in the relaxation to 2.1 a.u. for Fe, 2.2 a.u. for the In atoms in the surface layer, 2.1 a.u. for the remaining In atoms, and 1.9 a.u. for all As atoms. Spherical harmonics up to $l_{max} = 8$ were used for the basis functions in the MTs and with $l_{max} = 6$ for the expansion of the non-spherical potential.

4.2.2 Geometry of Fe[$1\bar{1}0$]/InAs(110)

After the relaxation and convergence tests we obtained the geometry pictured in Fig. 4.4 in the case of Fe chains along the [$1\bar{1}0$] direction. Fig. 4.4 (a) shows an isometric perspective of two relaxed unit cells. We assume that the mirror symmetry, imposed from the InAs(110), remains. This means that the y-coordinate of all atoms was kept fixed during the relaxation. So the relaxation concerns the x- and z-coordinates of Fe and two surface layers of

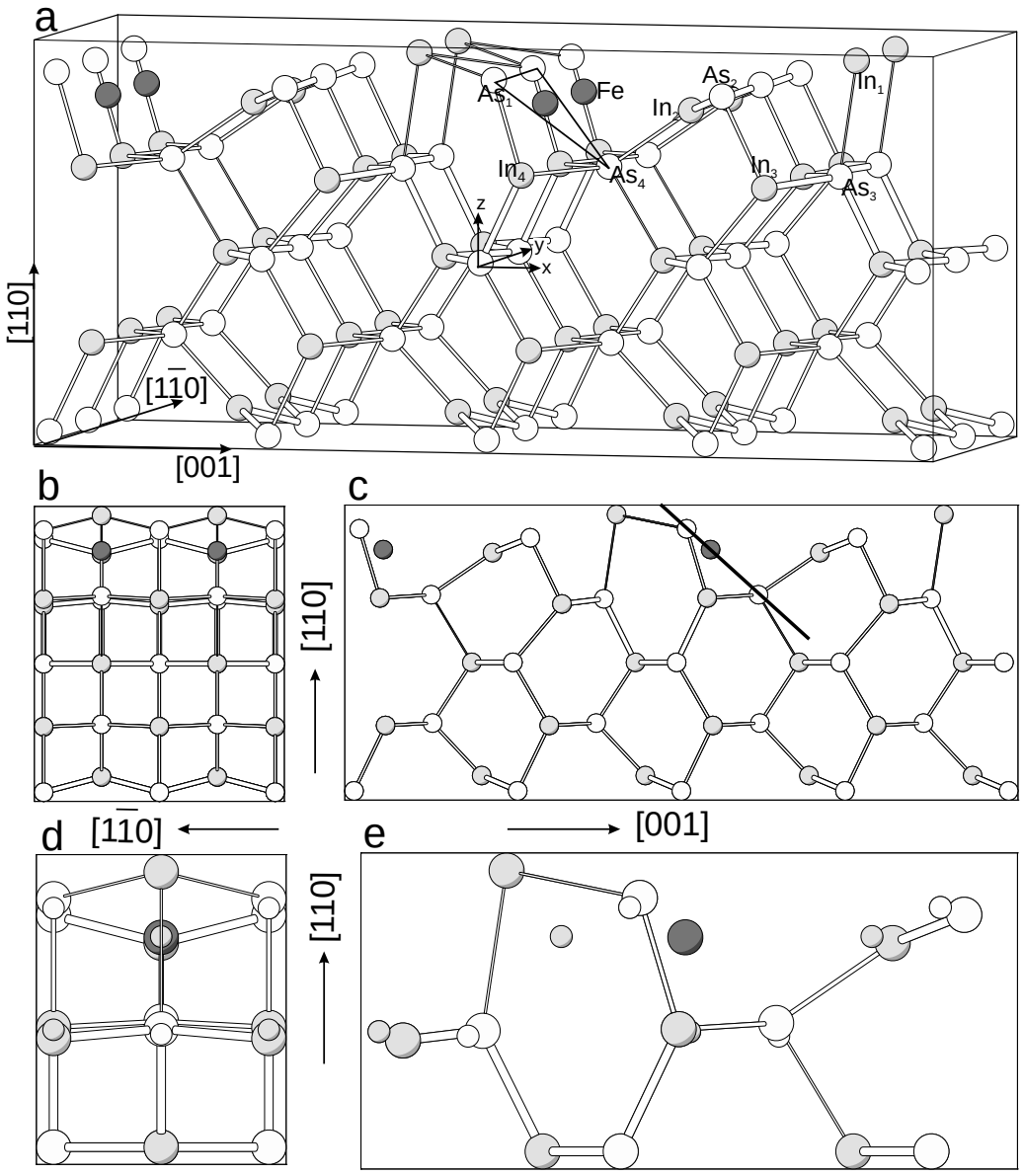

Figure 4.4: The structure of 5 layers InAs with Fe-chains along the [1$\bar{1}$0] direction on top. Fe is marked dark grey, In is light grey, and As white. (a) Isometric view of the structure. The atoms allowed to relax are marked with Fe, In_1-In_4, As_1-As_4. (b) - (e) Orthogonal projections of the structure. (d), (e) The relaxed atoms and the bulk layer are shown. Small spheres indicate the atomic positions for the free InAs(110) surface.

InAs. The relaxed atoms in one unit cell are marked with Fe_1, As_1-As_4 and In_1-In_4. The Fe atom (dark grey) goes from the top position in the starting configuration, which we took from the calculation with the Fe ML, to the energetically preferable position embedded in the first layer of InAs. This position is in the middle of the triangle formed by two mirror symmetrically connected As_1- and As_4-sites at the corners, as indicated in Fig. 4.4 (a). The orthogonal projection of the structure, shown in Fig. 4.4 (c) demonstrates that Fe is indeed in the same plane as the three As atoms. The distances between Fe and As_1 of 4.609 a.u. and between Fe and As_4 of 4.596 a.u. can be considered equal within limits of accuracy in the relaxation. We suppose that Fe forms bonds to these three As atoms. The nature of these bonds will be studied later in this work. The strength of the bonds between In and As is indicated by the respective bond lengths and marked as a different thickness of the bar between the atoms. The strongest bonds (thick bar) correspond to the previously calculated bulk value of 4.93 a.u.. The range of the bond length between 5.01 a.u. 5.41 a.u. corresponds to an intermediate strength and a length between 5.5 a.u. and 7.11 a.u. indicates the weakest bond. There are four bonds in this upper length range, as visible in Fig. 4.4 (a). These are all the bonds of In_1, which is the top atom, and the bond between As_4 and In of the bulk layer. Consequently, we assume that due to the presence of the Fe atom these bonds are considerably weakened.
Figures 4.4 (b) and (c) are the orthogonal projections of the same structure. They demonstrate that the vertical position of Fe and In_2 are nearly the same.

Figures 4.4 (d) and (e) show the top three layers of one 2-D unit cell from Fig. 4.4 (b) and (c). For comparison the positions of the free InAs(110) surface atoms are drawn in the same plot as small spheres. The largest visible deviations between the pure InAs(110) and Fe[1$\bar{1}$0]/InAs(110) are in the vicinity of In_1 and In_2. In_2 moves into the film after the Fe deposition. It is located in the plane defined by As_4 and two mirror plane connected As_2. In_1, on the other hand, relaxes outwards from the surface.

In the following, some quantitative data of the relaxed structure are given and compared between Fe[1$\bar{1}$0]/InAs(110) and InAs(110). The coordinates of the relaxed structure and their convergence with increasing number of plane waves are summarized in Table 4.2.

The As atom in the middle layer was chosen as the point of origin as marked in Fig. 4.4 (a) by the x,y,z-axes. Table 4.2 shows that for K_{max} between 3.7 a.u.$^{-1}$ and 3.8 a.u.$^{-1}$ the changes of the atomic coordinates are all below 0.1 a.u.. Consequently, sufficient convergence is achieved with K_{max}=3.7 a.u.$^{-1}$. The starting value for K_{max} of 3.4 a.u.$^{-1}$ is apparently too

	K_{max} [a.u.$^{-1}$]	3.4	3.5	3.6	3.7	3.8
Fe	x [a.u.]	2.44	2.41	2.39	2.39	2.41
	z [a.u.]	7.91	7.90	7.88	7.88	7.88
In_1	x [a.u.]	4.18	4.19	4.20	4.20	4.20
	z [a.u.]	10.86	10.67	10.54	10.41	10.34
As_1	x [a.u.]	0.82	0.77	0.74	0.71	0.71
	z [a.u.]	9.44	9.42	9.39	9.35	9.33
In_2	x [a.u.]	10.08	10.06	10.04	10.02	10.01
	z [a.u.]	7.72	7.70	7.69	7.67	7.66
As_2	x [a.u.]	12.69	12.67	12.67	12.66	12.64
	z [a.u.]	8.73	8.72	8.72	8.71	8.71
In_3	x [a.u.]	-7.89	-7.92	-7.93	-7.96	-8.01
	z [a.u.]	4.12	4.11	4.11	4.10	4.09
As_3	x [a.u.]	-5.01	-5.01	-5.02	-5.04	-5.08
	z [a.u.]	4.47	4.48	4.47	4.46	4.44
In_4	x [a.u.]	2.01	2.04	2.05	2.11	2.14
	z [a.u.]	4.59	4.56	4.55	4.57	4.55
As_4	x [a.u.]	5.74	5.72	5.72	5.73	5.72
	z [a.u.]	4.77	4.76	4.76	4.75	4.73

Table 4.2: The relaxed coordinates of Fe[1$\bar{1}$0]/InAs(110) and their convergence with increasing number of plane waves. The configuration achieved with $K_{max} = 3.7/3.8\,\text{a.u.}^{-1}$ is then analysed in the text. Notation is given in Fig. 4.4.

small to yield the atomic coordinates with a precision of 0.1 a.u.. The largest change in the atomic position from $K_{max} = 3.4$ a.u.$^{-1}$ to $K_{max} = 3.8$ a.u.$^{-1}$ is in the z-coordinate of In_1 and amounts to -0.56 a.u.. Since In_1 is the top atom on the surface, it plays a decisive role in simulating STM images. Consequently, the change in the z-coordinate of In_1 of -0.56 a.u. is very important for getting correct simulations of dI/dU and CCM images. Nevertheless, $K_{max} = 3.4\,\text{a.u.}^{-1}$ is enough to reproduce the planar arsenic neighborhood of the Fe atom.

Next we compare bond lengths and bond angles in the surface layer of pure InAs(110) and Fe[1$\bar{1}$0]/InAs(110). Two of the four bonds for each InAs atom are in the InAs(110) plane. For two relaxed layers one of the remaining two bonds points to the middle of the film and one points to the surface layer or to the vacuum respectively.

We will use the notation adopted from Engels [14]. The bonds in the

InAs(110) plane are called **bridge bonds (BrB)**, bonds pointing to the middle of the film are called **back bonds (BB)** and those pointing to the surface layer or to the vacuum - **dangling bonds (DB)**. The notation for DB deviates from the notation used by Engels, where DB is used only for the bonds pointing to the vacuum. We denote the angle between BrBs with α, and that between BrB and BB with β. The bond lengths and the angles between the bonds for the relaxed atoms of Fe[1$\bar{1}$0]/InAs(110), Fe[001]/InAs(110) and InAs(110) are summarized in Table 4.3.

The data for the pure InAs(110) surface are in good qualitative agreement with previous calculations on InAs(110) [14]. The main change in the bond lengths between pure InAs(110) and Fe[1$\bar{1}$0]/InAs(110) happens for In_1. The BB of In_1 is increased by 30% and the BrB by 20% compared with the bulk value of 4.95 a.u.. The angles between the bonds are strongly reduced for In_1 in case of Fe[1$\bar{1}$0]/InAs(110) compared to pure InAs(110). For As_1 the BB remains almost like in the pure InAs(110) surface. The angle between BrB and BB as well as the length of the BrB change strongly mainly due to the changed position of In_1, which is connected through the BrB to the As_1. The changes for In_2 and As_2 are less drastic. The BB of In_2 is increased by 10% in length compared to the value in pure InAs(110).

From Fig. 4.4 (d) und (e) and Table 4.3 we conclude that the Fe mainly affects the relaxation in its close vicinity. Just one unit cell away from an adsorption position of Fe, InAs(110) exhibits the configuration known from the pure InAs(110) surface with As atoms on top and In in almost planar neighborhood of the As atoms.

4.2.3 Geometry of Fe[001]/InAs(110)

For the Fe atoms placed along the [001] direction and with all atoms in the same starting configuration as for Fe[1$\bar{1}$0]/InAs(110), after relaxation we obtain the structure shown in Fig. 4.5. The relaxed atoms of one unit cell are marked in Fig. 4.5 (a) with Fe, In_1-In_3 and As_1-As_3. The unit cell contains two As_1 and two In_3 which are coincident under the mirror symmetry. Consequently, the positions of only seven different atoms are optimized. Under the additional constraint that the mirror symmetry is preserved, all three coordinates are allowed to relax. This means that not only x- and z-coordinates change, but also the y-coordinate is allowed to change without breaking the mirror symmetry. The change of the y-coordinate results in dimerization of As_1 and In_3, as can be seen in Fig. 4.5 (c), (e). We assume that this dimerization is caused by some kind of interaction between Fe and As_1 and not by the dimerization of arsenic DB's. The top position is occupied by Fe, which is 0.2 a.u. higher than In_1. Along the [001] direction

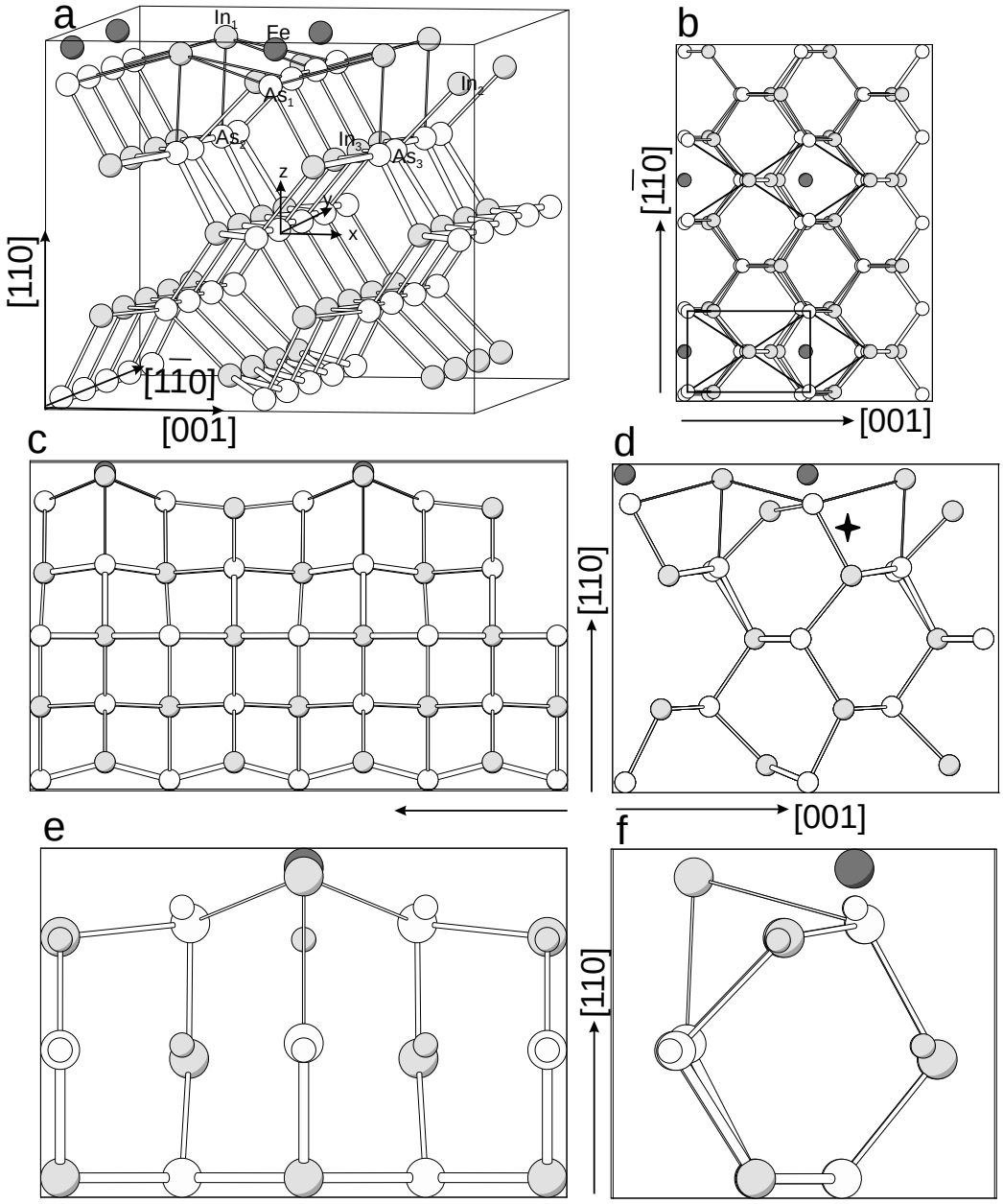

Figure 4.5: The structure of 5 layers InAs with Fe-chains along the [001] direction on top. Fe is marked dark grey, In light grey and As white. (a) Isometric perspective of the structure. The atoms allowed to relax are marked with Fe, In_1-In_4, As_1-As_4. (b) - (d) Orthogonal projections of the structure. (e), (f) The relaxed atoms and the bulk layer are shown. Small spheres indicate the atomic positions for the free InAs(110) surface.

InAs(110)

	In_1	As_1	In_2	As_2	In_3	As_3	In_4	As_4
BrB [a.u.]	5.15	5.15	5.15	5.15	5.2	5.2	5.2	5.2
BB [a.u.]	4.97	4.97	4.97	4.97	5.08	5.12	5.08	5.12
α [$\circ$]	103	103	103	103	102	102	102	102
β [$\circ$]	120	95	120	95	106	111	106	111

ML(Fe)/InAs(110)

	In_1	As_1	In_2	As_2	In_3	As_3	In_4	As_4
BrB [a.u.]	7.29	7.29	7.29	7.29	4.97	4.97	4.97	4.97
BB [a.u.]	5.61	5.5	5.61	5.5	5.29	5.1	5.29	5.1
α [$\circ$]	68	68	68	68	109	109	109	109
β [$\circ$]	97	105	97	105	114	103	114	103

Fe[1$\bar{1}$0]/InAs(110)

	In_1	As_1	In_2	As_2	In_3	As_3	In_4	As_4
BrB [a.u.]	6.43	6.43	4.94	4.94	5.0	5.0	5.40	5.40
BB [a.u.]	5.96	5.04	5.2	5.13	5.25	5.0	4.98	5.55
α [$\circ$]	78	78	110	110	107	107	97	97
β [$\circ$]	87	112	124	92	115	101	109	108

Fe[001]/InAs(110)

	In_1	As_1	In_2	As_2	In_3	As_3	In_4	As_4
BrB [a.u.]	7.07	7.07/5.01	5.01	4.94	4.94/5.09	5.09	-	-
BB [a.u.]	5.54	5.10	5.19	5.01	5.07	5.00	-	-
α [$\circ$]	65	93	116	101	108	115	-	-
β [$\circ$]	75	126/95	115	101	120/110	104	-	-

Table 4.3: Bond lengths and angles between bonds for the surface atoms of the InAs(110), Fe[1$\bar{1}$0]/InAs(110) and Fe[001]/InAs(110). BrB: bridge bonds, BB: back bonds, α: angle between BrBs, β: angle between BrB and BB

In_1 has a position nearly equidistant between two Fe atoms, as visible in Fig. 4.5 (d). The distance between In_1 and As atoms of the surface layer previously bonded to it is increased to 6.97 a.u.. The distance to the As atoms of the neighbouring unit cell is decreased to 7.06 a.u.. This means that in the (110) plane In_1 has a position nearly in the center of the rectangle drawn in Fig. 4.5 (b) with As_1 atoms at the corners. As a consequence, we cannot decide solely from the structure, if a bond between the In_1 and As_1 from the same unit cell and from the neighbouring unit cell exists.

To indicate this, thin bonds between the In_1 and As_1 of the same and the

neighbouring unit cells are shown in the picture, so that In_1 appears with five bonds, four to the As atoms in the same layer and one to the As_2 in the subsurface layer. The thickness of all bonds shown indicates their lengths. Over the whole structure only the five bonds of In_1 are drawn with thin lines, which correspond to the length range between 5.5 a.u, and 7.11 a.u.. In the next sections we will investigate which of these indicated bonds on In_1 really do exist. However, already from the relaxation data alone it is clear that the original bonds between In_1 and the As atoms are severely weakened. We conclude that for both structures, for Fe[1$\bar{1}$0]/InAs(110) and

	K_{max}[a.u.$^{-1}$]	3.4	3.5	3.6	3.7	3.8	MT
Fe	x [a.u.]	0.60	0.65	0.66	0.66	0.56	0.41
	z [a.u.]	10.85	10.86	10.88	10.49	10.44	10.19
In_1	x [a.u.]	-5.27	-5.21	-5.08	-4.84	-4.88	-4.90
	z [a.u.]	11.76	11.67	11.07	10.82	10.58	9.94
As_1	x [a.u.]	0.80	0.82	0.82	0.78	0.77	0.76
	y [a.u.]	-0.74	-0.74	-0.63	-0.40	-0.40	-0.21
	z [a.u.]	8.51	8.52	8.52	8.47	8.46	8.46
In_2	x [a.u.]	-3.63	-3.55	-2.99	-1.95	-1.89	-1.91
	z [a.u.]	10.78	10.50	10.19	8.58	8.28	7.96
In_3	x [a.u.]	-7.91	-7.92	-7.96	-8.07	-8.13	-8.26
	y [a.u.]	-0.11	-0.11	-0.10	-0.22	-0.25	-0.21
	z [a.u.]	3.87	3.88	3.91	3.93	3.94	3.95
As_3	x [a.u.]	-4.99	-4.99	-5.00	-5.01	-5.02	-5.14
	z [a.u.]	4.56	4.56	4.58	4.60	4.58	4.44
As_4	x [a.u.]	-5.20	-5.20	-5.21	-5.36	-5.43	-5.55
	z [a.u.]	4.65	4.63	4.58	4.40	4.33	4.20

Table 4.4: Convergence of the relaxed coordinates of Fe[001]/InAs(110) with increasing plane wave cut-off parameter K_{max} . The last column corresponds to $K_{max} = 3.8$ a.u^{-1} and increased MT radii. Notation is given in Fig. 4.5.

Fe[001]/InAs(110), the geometry is determined by the partial substitution of an In atom with Fe in the In-As bonds.

In Figure 4.5 (d) a star indicates the position of the Fe atom in the case of Fe[1$\bar{1}$0]/InAs(110) (see Fig. 4.4 (c)). By comparing Fig. 4.5 (c) and Fig. 4.4 (c) we see that the distance between the marked position and In_1 of the next unit cell is smaller in Fig. 4.5 (c) than in the case of Fe[1$\bar{1}$0]/InAs(110). We assume that the presence of the In in the neighbourhood of the marked position displaces the Fe atom from this position further outwards of the surface.

Summarizing we can say that two trends determine the geometry of the structure. Fe tends to have a position as near as possible to the As atoms and at the same time as far as possible from the In atoms.

To confirm this structure we performed at first the same convergence test on the number of plane waves, like for the Fe[1$\bar{1}$0]/InAs(110). The relaxed coordinates and their convergence over the number of plane waves are summarized in Table 4.4. The point of origin is on the As atom in the middle layer as marked in Fig. 4.5 (a). In the last step of increasing K_{max} from 3.7 a.u.$^{-1}$ to 3.8 a.u.$^{-1}$ the largest change of -0.3 a.u. is in the z-coordinate of In_2.

This accuracy is not sufficient for a proper calculation of the electronic structure and simulation of an STM measurement. Further increase of the number of plane waves would blow up the calculation time beyond feasible border. Another way to improve this point is the increase of the muffin-tin radii. The disadvantage of this approach is that the energy of the calculation cannot be compared any more with the energy of the structure Fe[1$\bar{1}$0]/InAs(110). I increased the muffin-tin radii to the values 2.1 a.u. for Fe, 2.2 a.u. for In_1 and In_2, 2.1 a.u. for the remaining In atoms, and 1.9 a.u. for all As atoms. The result of this improved relaxation is summarized in the last column of Table 4.4. Especially considering the In_1 of the first layer, this last step with increased MTs was indispensable. With increased MT, In_1 went more than 0.5 a.u. into the surface.

Only this step gives the correct relation between the vertical position of Fe and In_1 atoms, namely, that Fe has the highest position.

Table 4.4 demonstrates that the coordinates of the In atoms are especially sensitive to the increase of K_{max} in a particular way. Namely a small K_{max} leads to the underestimation of the bonding between As and In atoms in the surface layer. The y-coordinate of As_1 shows that the dimerization of As_1 decreases with increase of K_{max}. So we conclude that another consequence of a too small K_{max} is the overestimation of the bonding between Fe and As.

Chapter 5

Electronic and magnetic properties of Fe chains on InAs(110)

This chapter is focused on the determination of magnetic moments and the comparison between two magnetic structures, namely ferromagnetic (FM) vs. antiferromagnetic (AF) ordering for both chain directions. To determine the magnetic structure we calculated the FM and AF state for both geometries with a unit cell twice as large as for the crystal structure. To perform the calculation within reasonable time the cut-off parameter for the number of plane waves was reduced to $K_{max} = 3.2\,\text{a.u.}^{-1}$. For the 2DBZ sampling we used 6 k-points in the irreducible part of the 2DBZ. The MT radii were set as in the relaxation calculation of Fe[1$\bar{1}$0]/InAs(110), namely 1.8 a.u. for the As, and 2.0 a.u. for Fe and In. The remaining numerical parameters are the same as in the relaxation calculation. The results of this calculation and their interpretation are covered in the following sections.

5.1 Magnetic structure of Fe[1$\bar{1}$0]/InAs(110)

In the case of Fe[1$\bar{1}$0]/InAs(110) the AF structure is favourable with an energy of 550 meV. The convergence test for the number of plane waves shows, that with the increase of $K_{max} = 3.1\,\text{a.u.}^{-1}$ to $K_{max} = 3.2\,\text{a.u.}^{-1}$ the difference in the energies of the AF and FM state decreases from 580 meV to 550 meV. This means, that the difference in the energy between the two states is converged with the accuracy of 30 meV.

The electronic configuration of As_1 of a free InAs(110) surface consists of four completely occupied sp^3-hybrids. Fe as a free atom has $3d^6\ 4s^2$ configu-

ration. This means that among the five d-orbitals one is completely occupied and four are half-filled. After the adsorption on the surface the magnetic moment of Fe changes from 4 μ_B to 2.4 μ_B. It has 4.1 d-electrons of one spin channel and 1.7 of the other. This means that the electrons are rearranged in a way, that approximately two d-orbitals are filled and one empty. The magnetic moment of Fe is slightly higher in the AF case with $\mu = 2.44\,\mu_B$ than in the FM case with $\mu = 2.38\,\mu_B$. The Fe induces also a small magnetic moment on InAs namely in the MTs of As_1 and As_4 following the notation given in Fig. 4.4. In the FM case these magnetic moments are $\mu(As_1) = 0.025\,\mu_B$ and $\mu(As_4) = 0.01\,\mu_B$, whereas in the AF case $\mu(As_4) = 0.03\,\mu_B$ and $\mu(As_1)$ vanishes.

Some hints to a possible explanation of the AF structure can be extracted solely from the geometry of the system. In section 4.2.2 it was discussed that the geometry of the system indicates a strong interaction between Fe and As_1, As_4. One well known model of the AF interaction of the magnetic atoms embedded in a non-magnetic system is superexchange. Superexchange is the interaction between magnetic cations via a non-magnetic anion. This interaction depends strongly on the overlap between cation and anion orbitals and thus on the character of the interacting orbitals and the cation-anion-cation angle. With the angle Fe-As_1-Fe of $\frac{2}{3}\pi$ and the position of As_1 symmetrically between the Fe atoms of the chain an overlap between As_1 p-orbitals and Fe d-orbitals is possible. The character of these orbitals will be discussed later in this section. These observations strongly suggest that superexchange between the Fe atoms via As_1 is the mechanism that leads to the AF structure.

In the following we can show from our results that the Fe atoms indeed interact strongly with adjacent As atoms and that the interaction with As_1 leads to superexchange and to the energetically prefered AF configuration in the Fe chain.

5.1.1 DOS of Fe[1$\bar{1}$0]/InAs(110)

The DOS in the Fe MT for the FM and AF Fe chains along the InAs rows are presented in Fig. 5.1 (a)-(d). For the FM structure (a), (b) the DOS in both spin channels are not only shifted with respect to each other by 2.5 eV, but have also different band width. The DOS in the spin1 channel has a width of 2 eV and is nearly constant in the range from -3.5 eV to 1.5 eV, whereas the DOS in spin2 channel has a width of approximately 1.5 eV with a maximum at E_F.

The DOS of the AF structure Fig. 5.1 (c), (d) has approximately the same bandwidth of 2 eV in both spin channels. Spin1 channel shows, differently to the FM case, a clear two-peak structure. The formation of the band gap

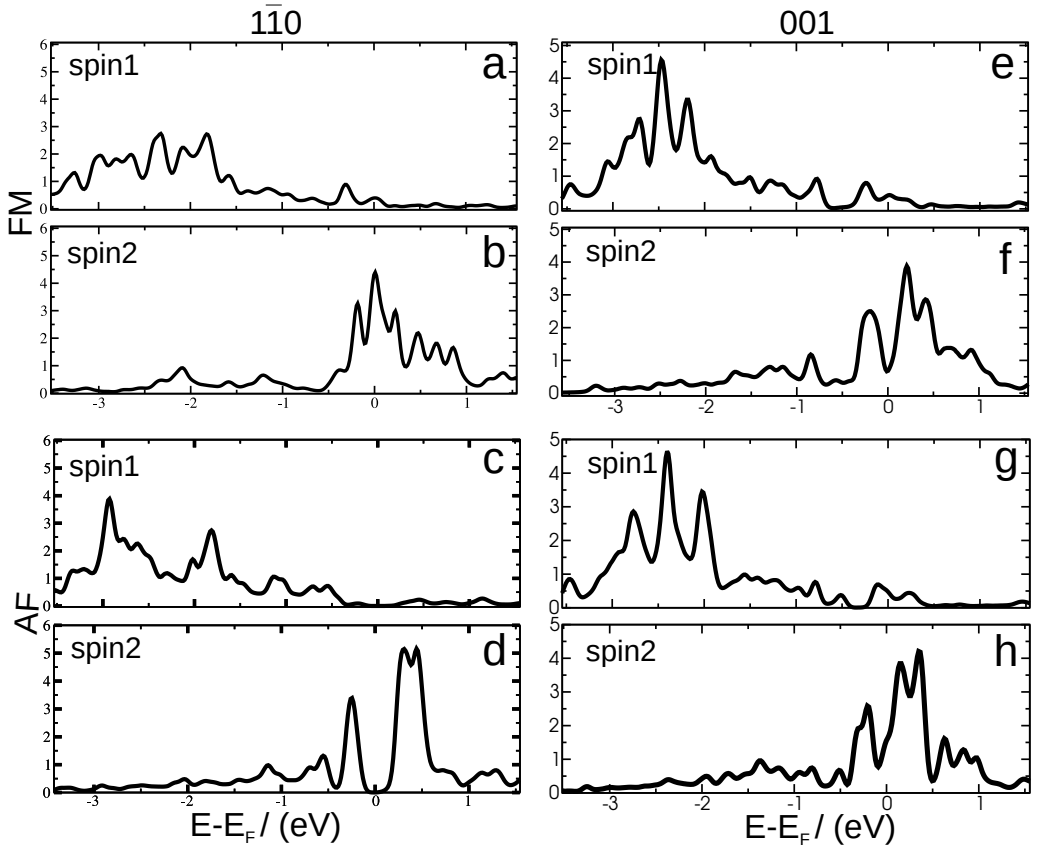

Figure 5.1: The left column (a) - (d) shows the DOS in the Fe MTs for the Fe[1$\bar{1}$0]/InAs(110) structure. (e) - (h) show the DOS in the Fe MTs for the Fe[001]/InAs(110) structure.

of about 0.3 eV at E_F in the spin2 DOS of Fig. 5.1 (d) in effect lowers the energy of the occupied states and leads to the preference of the AF structure. Consequently we focus in the following discussion on the formation of the band gap in the DOS of the AF structure. Two different effects play a role in the creation of this band gap. The first one is a symmetry breaking induced through the antiferromagnetism, which leads to the splitting at the edge of the quasi-one-dimensional BZ. The second effect is the bond formation between Fe and As_1 in the AF case, which leads to the splitting of the DOS around E_F into bonding and antibonding states with a band gap between them.

The DOS of As_1 and As_4 presented in Fig. 5.2 provides additional indication for a strong interaction between Fe and adjacent As. The As_1 DOS

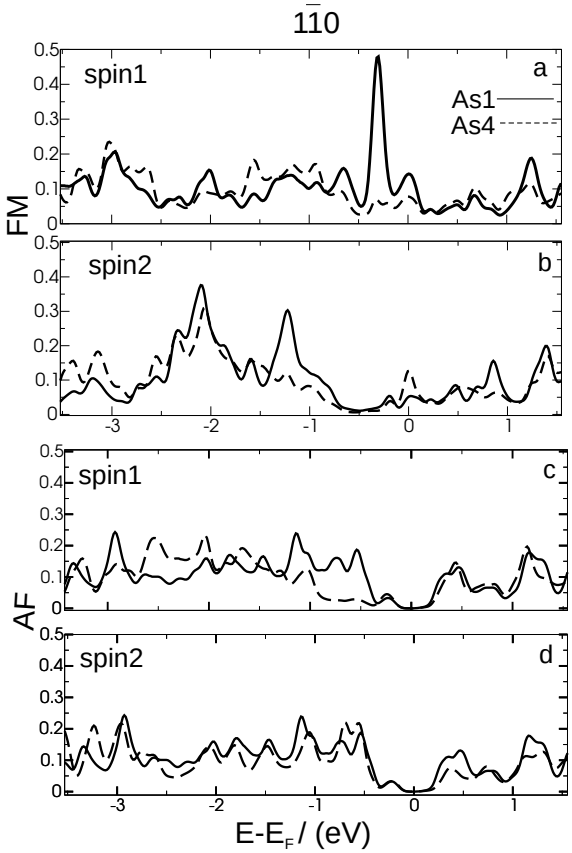

Figure 5.2: The DOS in the MTs of As_1 (solid line) and As_4 (dhashed line) for the Fe[1$\bar{1}$0]/InAs(110) structure.

of the FM case in Fig. 5.2 (a)-(b), shows one prominent peak at -0.3 eV and a smaller peak directly at E_F in the spin1 channel and vanishes almost completely around E_F in the spin2 channel. We assume, that the peak at -0.3 eV in the spin1 channel is spatially so extended, that it contributes also to the DOS in the Fe MTs in the spin1 channel at -0.3 eV. The As_4 DOS has in both spin channels a small contribution at E_F. For the AF case the DOS of As_1 as well as the DOS of As_4 exhibit a band gap in both spin channels and have no other significant features in the energy range shown. The spin polarisation of the As_4 state around -0.5 eV is not surprising, since this As interacts only with one Fe atom of the unit cell. The striking change of the As_1 DOS with the change of magnetic configuration in the Fe chain is an indication for the significant role of As_1 in the formation of the magnetic configuration.

One of the differences between our calculations and the experiment is that in the calculations the magnetic configuration is imposed as a restriction on the system. The result is the energy of the system and the acompanying interaction. In the experiment the true magnetic configuration arises from interaction between the atoms. Comparing the DOS of As and Fe in

Fig. 5.2 (a), (b) and Fig. 5.1 (a), (b) we see narrow peaks around E_F on Fe (spin2 channel) and As_1 (spin1 channel) indicating that there is no interaction between these states in the FM configuration. This interaction is switched on in case of the AF configuration, which is energetically prefered. This means, that in the real system the interaction between these states forces the system into the AF configuration and leads to the splitting into bonding and antibonding states and to the formation of a band gap.

5.1.2 Dominant superexchange paths in Fe[1$\bar{1}$0]/InAs(110)

Superexchange is a special exchange interaction between two magnetic atoms via a nonmagnetic atom. Such a mechanism was originally proposed by Kramers [27]. Quantitative estimates of the dependence on the angle between cation-anion-cation were given by Anderson [2]. The superexchange is possible only if orbitals of the magnetic atoms exhibit sufficient overlap with an orbital of the non-magnetic atom. This leads to the dependence of the interaction on the cation-anion-cation angle, which was first quantitatively estimated by Anderson [2]. As pointed out by Goodenough and Loeb [18] the symmetry of the interacting orbitals is decisive for the superexchange. The entity of the interacting orbitals is called superexchange path. From the symmetry of the d- and p-states and from the previous qualitative evaluation of the states around E_F we suggest that the superexchange in this system is dominated by two paths. Figure 5.3 schematically shows the contributing orbitals and the geometry. Two Fe d_{xy} orbitals with an overlaping As p_y orbital between them are shown in Fig. 5.3 (a). The image plane is the plane going through two As_1 and As_4 as it is shown in Fig. 4.4. A σ bond between Fe and As_1 provides a large overlap between the orbitals and thus a large interaction. This superexchange path we call in the following d_{xy}-p_y superexchange. Superexchange in general, can have AF as well as FM character, as described in detail in [17]. For our system in case of a half-filled d_{xy} orbital the bond formation takes place only between electrons of opposite spins, leading to a strong AF coupling between the Fe atoms. Due to the intraatomic exchange between d-orbitals on the Fe the spin of the filled orbitals plays a role in the bond formation between empty d-orbitals and the p-electrons of As. The spin of electrons transfered from As into the bonding orbital has to align parallel to the spin of Fe. This leads to an AF coupling between Fe atoms.

Figure 5.3 (b) shows two Fe $d_{x^2-y^2}$ orbitals with the overlapping As p_x orbital between them. There is no definite answer to the question if this is a strongly asymmetric π bond between Fe $d_{x^2-y^2}$ and As p_x or a σ bond formed from only one lobe of p_x and Fe $d_{x^2-y^2}$ lobes on both sides. This

superexchange path we call in the following $d_{x^2-y^2}$-p_x superexchange. The angle between the bond line and the As p_x orbital is $\pi/3$. This means, that here the upper part of the π bond provides a very small contribution to the exchange interaction. Similarly to the d_{xy}-p_y superexchange path this path also gives antiparallel coupling between Fe atoms. Since π bonds in general are weaker than σ bonds the contribution of this path to the energy gain in the AF system is smaller than the contribution of the d_{xy}-p_y superexchange. We will discuss the band structure of the system in the following subsection

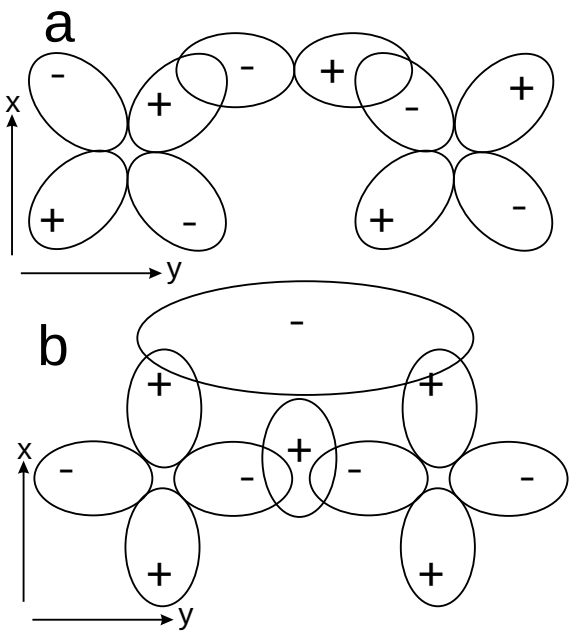

Figure 5.3: Bond paths of superexchange interaction between Fe cations (d-orbitals left and right) via As anion (p-orbital in the middle). (a) d_{xy} orbitals interact via As p_y. (b) $d_{x^2-y^2}$ orbitals interact via As p_x.

to see how exactly these two paths contribute to the splitting of the DOS into the bonding and antibonding states at E_F.

5.1.3 Band structure of Fe[1$\bar{1}$0]/InAs(110)

The band structures of the AF and FM configurations for both spin channels are plotted in Fig. 5.4 with Fe d_{xy} and As p_y states marked. Fe $d_{x^2-y^2}$ and As p_x states are marked in Fig. 5.5. The one-dimensional periodicity along $\overline{\Gamma Y}$ leads to the pronounced quasi-one-dimensional character of the band structure. The backfolding of the bands in the FM case is visible at $\overline{Y}$ and $\overline{M}$, which correspond to the edge of the one-dimensional BZ, with degeneracy of pairs of the states along $\overline{YM}$. Reduction of the symmetry removes these degeneracy in the AF case. The majority of the bands exhibits almost dispersionless behaviour perpendicular to the chain, i.e. along $\overline{YM}$ and $\overline{X\Gamma}$, and

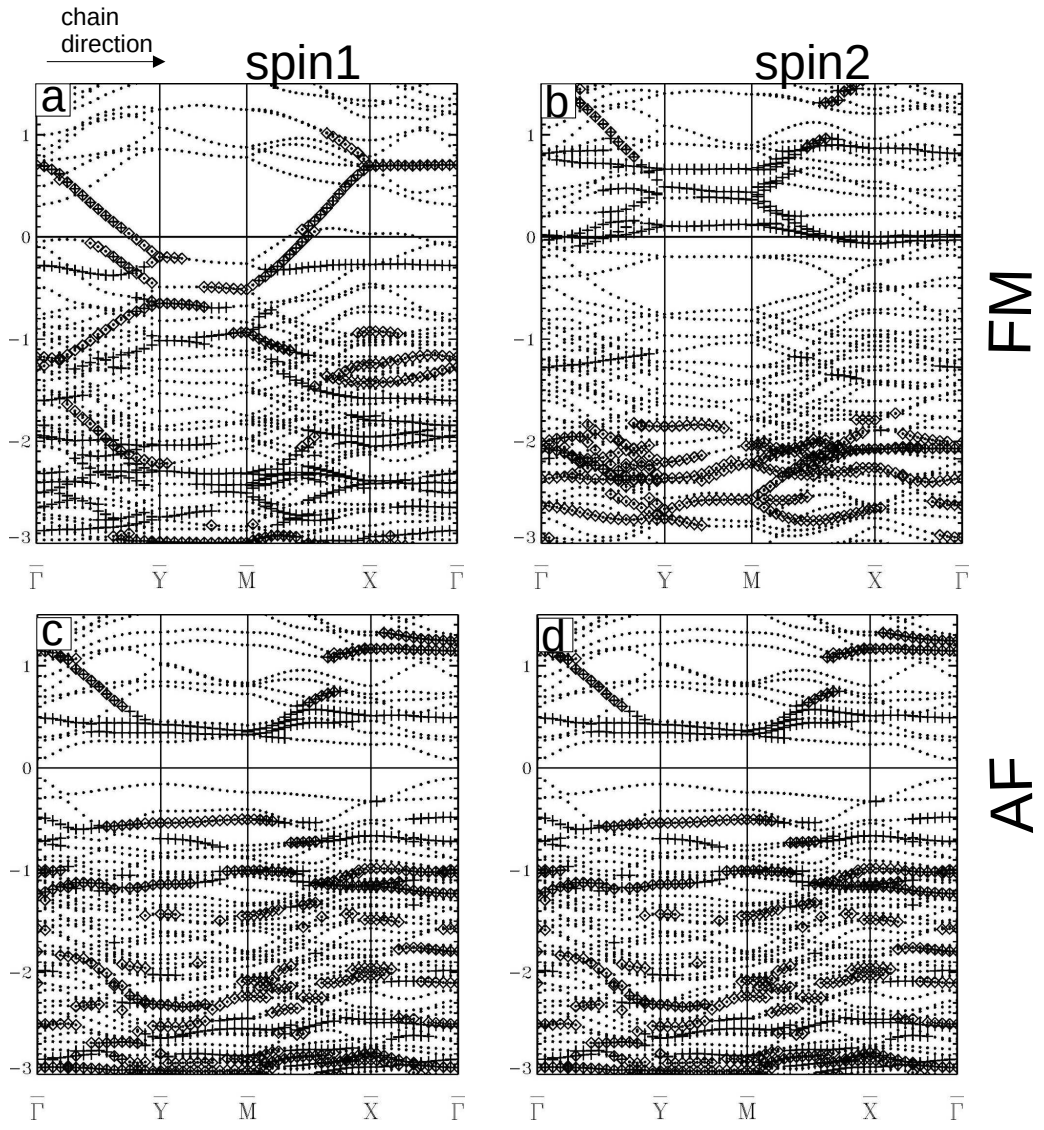

Figure 5.4: Projected band structure of Fe[1$\bar{1}$0]/InAs(110). The states marked with crosses are d_{xy} states localised on Fe MTs. The states marked with diamonds are p_y states localized to a large extent on As_1.

a strong dispersion along the chain, i.e. along $\overline{\Gamma Y}$ and $\overline{MX}$. The main contribution to the energy gain from the FM to the AF case comes from lowering of the partly occupied bands around E_F. Consequently the emphasis in the following discussion is put on the bands around E_F.

First, we discuss the FM band structure with projected bands of Fe d_{xy} and As p_y presented in Fig. 5.4 (a), (b). There is one partly filled As_1 band degenerate with an Fe band around E_F in the spin1 channel. These bands are occupied at the edge of the quasi one-dimensional BZ, along $\overline{YM}$, and exhibit a strong dispersion along the chain. The unoccupied part of these bands is visible as a completely dispersionless state at 0.8 eV along $\overline{X\Gamma}$, in the middle of the quasi one-dimensional BZ. Remaining marked states around E_F belong to the occupied As_1 band around -1 eV and the Fe band around -0.2 eV. Along the $\overline{YM}$ direction the As_1 band at E_F contributes to the peak at -0.6 eV in Fig. 5.2 (a) whereas the contribution of the dispersing part along $\overline{\Gamma Y}$ and $\overline{MX}$ to the DOS is rather small. Due to the strong dispersion, the contribution of the Fe band at E_F to the Fe DOS is negligible. In the spin2 channel presented in Fig. 5.4 (b) the Fe minority bands are around E_F while the As_1 bands are located around -2.1 eV. The prominent peak in the FM Fe DOS at E_F consists partly of two bands tagged with crosses in Fig. 5.4 (b) which are nearly dispersionless at E_F along the $\overline{X\Gamma}$ direction. The As_1 states are visible around -2.1 eV in the As DOS.

To summarize this section up to here we identified the states in the FM bandstructure, which can contribute to the d_{xy}-p_y superexchange, as an As_1 band degenerate with the Fe band at E_F in the spin1 channel (Fig. 5.4 (a)) and two partly filled Fe bands in Fig. 5.4 (b), which are nearly dispersionless at E_F along the $\overline{XG}$ direction. The interaction between these states leads to the hybridization and to a splitting in bonding and antibonding parts leading to the energetic preference of the AF order.

Next, we discuss the AF band structure with the aim to identify states evolved through the d_{xy}-p_y superexchange. The band structure of the AF case (Fig. 5.4 (c)-(d)) contains two nearly dispersionless bands around -0.6 eV and around $+0.6$ eV indicated with crosses. Two additional marked bands are: a dispersionless occupied band at -1 eV and a band dispergent along $\overline{\Gamma Y}$ and $\overline{MX}$ between $+0.6$ eV and $+1$ eV. In the AF Fe DOS these states are visible as small peaks around $\pm$ 1.1 eV and $\pm$ 0.6 eV. We assume that those are bonding and antibonding states arising from the interaction of the marked bands around E_F in Fig. 5.4 (a)-(b). Idications for this assumption are presented in the next subsection, where an example of the corresponding

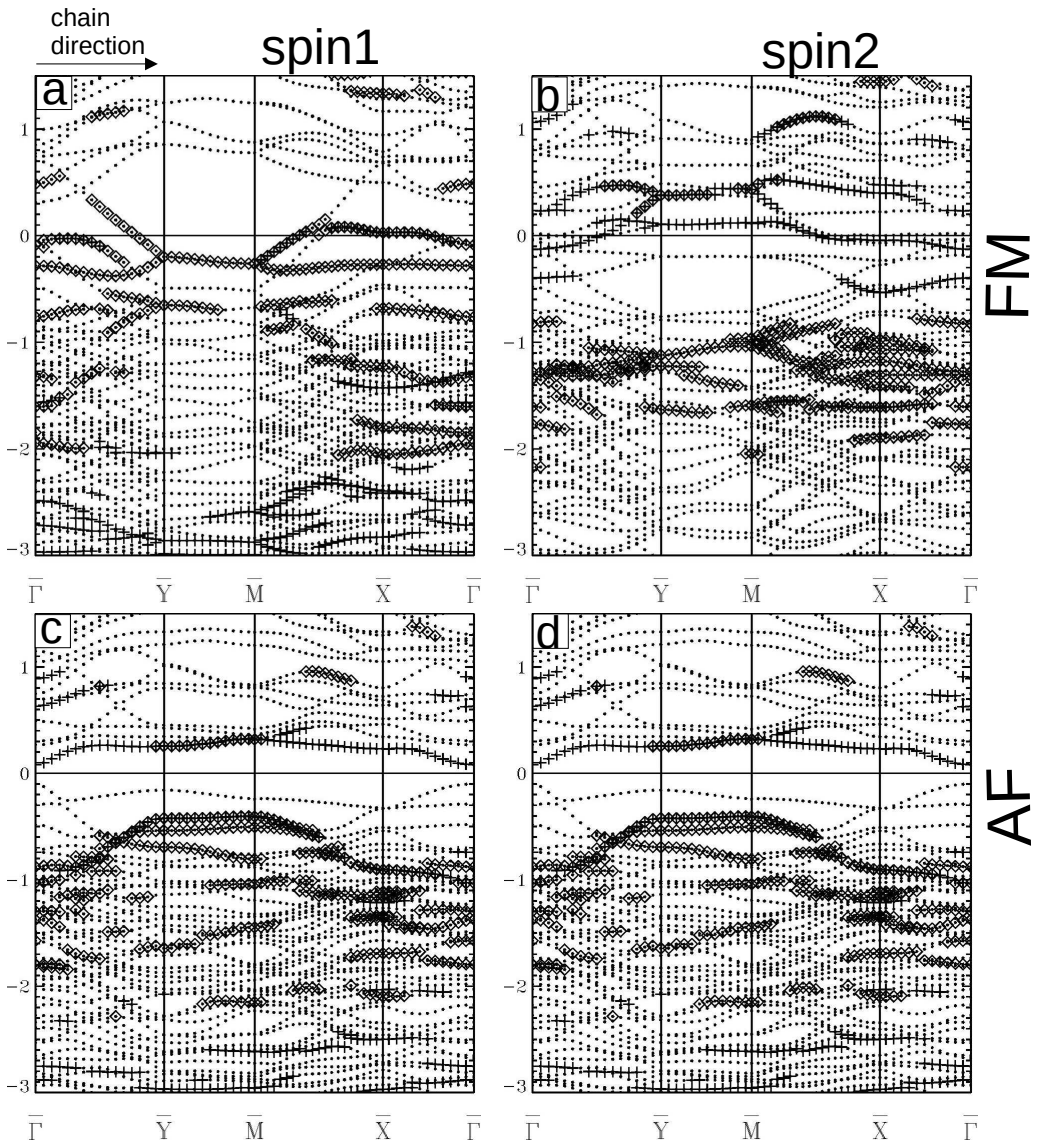

Figure 5.5: Band structure of Fe[1$\bar{1}$0]/InAs(110). The states marked with crosses are mainly Fe $d_{x^2-y^2}$ states. The states marked with diamonds are mainly As p_x states.

charge distribution is discussed.

The states contributing to the $d_{x^2-y^2}$-p_x superexchange are marked in the band structure in Fig. 5.5. Fe $d_{x^2-y^2}$ states are indicated with crosses and As_1 p_x states with diamonds. There is one partly filled, cross marked

band in the spin1 channel and one in the spin2 channel, which are nearly dispersionless at E_F around $\overline{\Gamma}$. These bands are degenerate with one spin1 As_1 band in the vicinity of $\overline{\Gamma}$. Another dispersionless spin1 As_1 band around -0.3 eV contributes to the prominent As_1 DOS in Fig. 5.2 (a). The interaction between these bands contributes to $d_{x^2-y^2}$-p_x superexchange and leads to the splitting of these states in the AF case.

Two bands are marked at the same time with crosses and diamonds in Fig. 5.5 (c). One has the energy of -500 meV along $\overline{\text{YM}}$ and -1 eV at $\overline{\Gamma}$. The counterpart of it is an empty band which has the energy between 200 meV and 300 meV along $\overline{\text{YM}}$ and 100 meV at $\overline{\Gamma}$. The As p_x contribution of this band is larger than a threshold of 7 % only along the $\overline{\text{YM}}$ direction. These bands are nicely visible in the AF Fe DOS (Fig. 5.1 (d)). The unoccupied band contributes to the large peak at 0.3 eV. The dispersionless part of the occupied band along $\overline{\text{YM}}$ is merged with a nearly flat band at -0.25 eV in the DOS to the peak at -0.25 eV, whereas the dispergent part in the remaining BZ has no significant contribution to the AF Fe DOS.

To complete our understanding of the bond formation, the next section will discuss the charge distribution of examplary states contributing to d_{xy}-p_y and $d_{x^2-y^2}$-p_x superexchange.

5.1.4 LDOS distribution in case of superexchange

To give an example of the distribution of the charge density in the states contributing to the d_{xy}-p_y superexchange we plot in Fig. 5.6 the contour and color scale plots of the states between $\overline{\text{M}}$ and $\overline{\text{X}}$ points at $\pm$700 meV marked as Fe d_{xy} and As_1 p_y in the AF bandstructure. Fig. 5.6 (a1)-(c1) and (a2)-(c2) show logarithmically scaled charge density plots in the plane containing Fe, As_1 and As_4. The color scale with corresponding values of the DOS at the edges is shown below. In the contour plots of the Fig. 5.6 (d1)-(f1) and (d2)-(d2) Fe atoms are marked with black circles and As atoms with white circles. The spin1 channel is presented in the left column of Fig. 5.6 (a1), (a2), the spin2 channel - in the right column of Fig. 5.6 (c1), (c2) and in the middle column (b1), (b2) the sum of both spin channels is shown.

The p_y state on As_4 is clearly visible in all panels additionally to the d_{xy} state on Fe and p_y on As_1. The bonds between Fe and As_1 are σ bonds, whereas bonds between Fe and As_4 are π bonds. The lobes of the p_y state at As_1 are slightly rotated in the spin1 channel with respect to the spin2 channel. Consequently, they are tilted to the left and to the right, respectively. Moreover, the tilt is exactly in the opposite direction for the two different spin channels. We consider now the spin1 channel Fig. 5.6 (a1), (a2). For

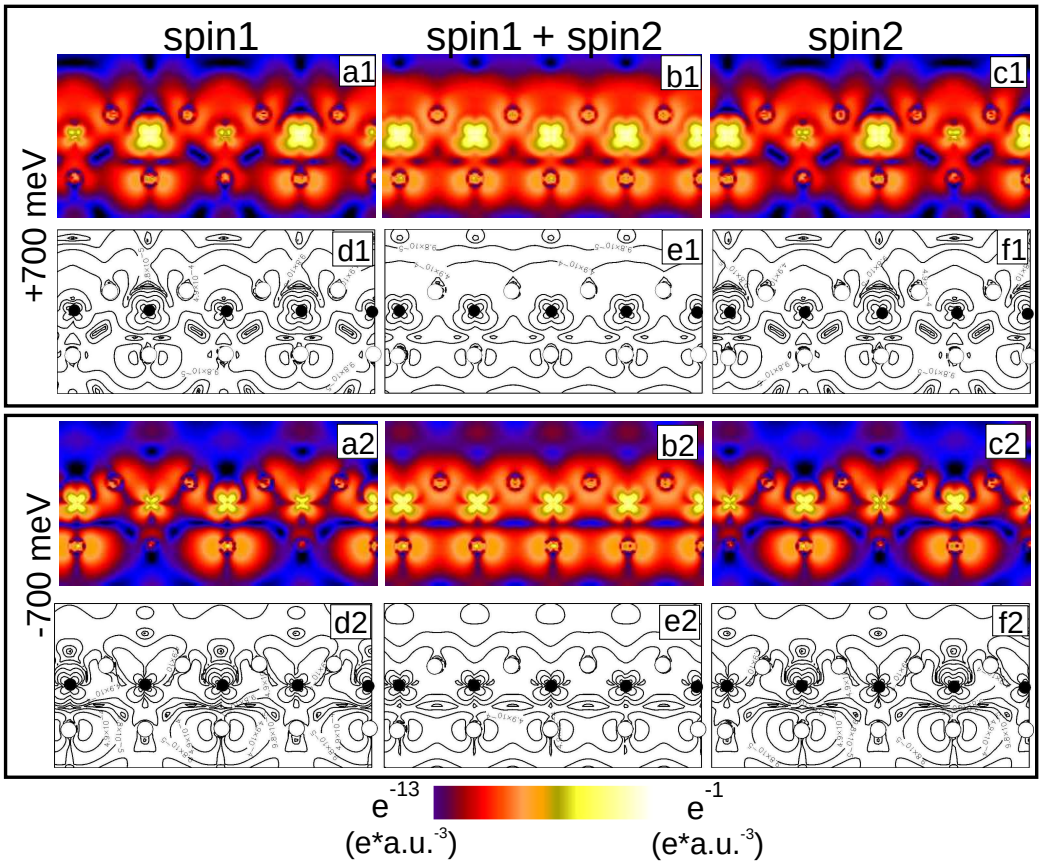

Figure 5.6: The contour plots and color plots of the states marked with crosses and at the same time with diamonds in Fig. 5.4 (c) along $\overline{\mathrm{MX}}$ at 700 meV (a1)-(f1) and -700 meV (a2)-(f2). In the right and left column the LDOS of the spin1 and spin2 channels are shown, respectively. The middle column represents the sum of both spin channels.

the bonding state (a2), one lobe of the p_y state, which is rotated away from the Fe, is nearly merged with one lobe of the d_{xy} state of this Fe. The polarization of the DOS on Fe for this state is almost negligible in accordance with the plot of the DOS in Fe MTs in Fig. 5.1 (c), (d). The bonding and antibonding character of the states is also clearly visible. Whereas in the bond between As_1 and the middle Fe in (a2) the charge density is persistent larger than zero, in (a1) within the same bond a node plane is visible. The bond between As_4 and Fe does not exhibit a clear bonding-antibonding character, although the spin-polarisation at As_4 changes the sign from -700 to 700 meV in agreement with the DOS of As_4 in Fig. 5.2 (c)-(d).

Summarizing, the plots in Fig. 5.6 clearly show that a strong bond is formed between Fe d_{xy} and As_1 p_y states. This confirms our assumption, that the superexchange is indeed the exchange mechanism between Fe atoms in the chain, and that one of the contributing superexchange paths is the d_{xy}-p_y. Additionally, the plots in Fig. 5.6 show a strong indication of the bonding and antibondig character of the Fe-As_1 bond. This is in agreement with our previous assumption that the band gap results from the splitting of the states at E_F in bonding and antibonding parts. As_4 obviously takes part in the bond formation but its contribution to superexchange is negligible compared to the contribution of As_1

Analogously, the contour and color plots of the states at $\overline{Y}$ at -500 meV and 210 meV presented in Fig. 5.7 are an example of the charge distribution in case of $d_{x^2-y^2}$-p_x superexchange. The plotted plane contains Fe, As_1 and As_4, as it is marked with a triangle in Fig. 4.4 (a). The states shown are marked in the band structure at $\overline{Y}$ as Fe $d_{x^2-y^2}$ and As p_x states at the same time. In the contour plots of Fig. 5.7 (d1)-(f1), (d2)-(f2) the Fe and As atoms are marked black and white. The spin1 channel is presented in the left column of Fig. 5.7 ((a1), (a2)), the spin2 channel, respectively, in the right column Fig. 5.7 ((c1), (c2)), and in the middle ((b1), (b2)) the sum of both spin channels.

First we consider the spin1 state at -500 meV (Fig. 5.7 (a2)). This state shows alternatingly a high intensity $d_{x^2-y^2}$ with a weak part from the d_{xy} state at Fe and a clear p_x at As_1. The lobes of the p_x states are slightly rotated away from the Fe $d_{x^2-y^2}$ of the same spin orientation and towards the Fe $d_{x^2-y^2}$ of the opposite spin orientation. Moreover, the tilt directions are opposite at -500 meV and +200 meV. The overlap between As_1 p_x and Fe $d_{x^2-y^2}$ states of opposite spin indicates a bond formation between them. Differently to the d_{xy}-p_y case, the bonding or antibonding character of this state cannot be identified solely from these plots. The contribution of this

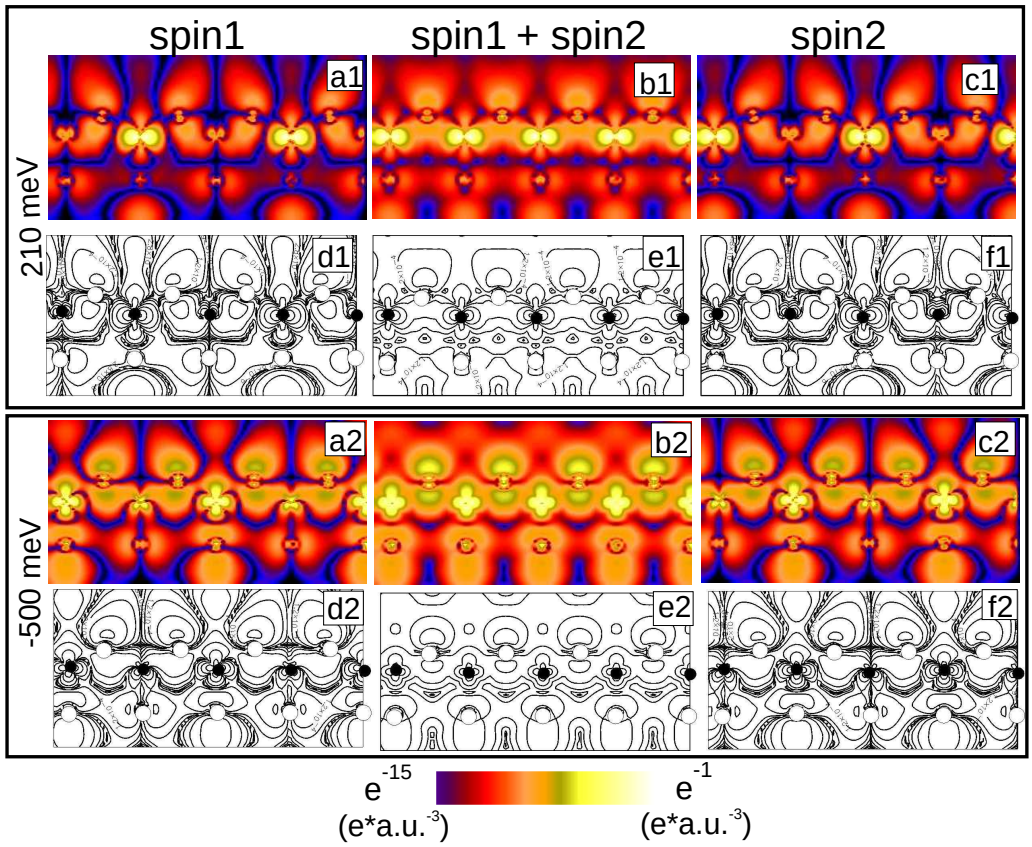

Figure 5.7: The contour plots and color plots of the states at 200 meV (a1)-(f1) and -500 meV (a2)-(f2) at $\overline{\Gamma}$, marked with crosses and diamonds in Fig. 5.5 (c), (d). In the right and left column the LDOS of the spin1 and spin2 channels are shown, respectively. The middle column represents the sum of both spin channels.

state to superexchange is estimated to be 500 meV provided that it emerges from the hybridization of the states at E_F. This is in nice agreement with the previously given difference of 550 meV between FM and AF configuration.

At 210 meV, the $d_{x^2-y^2}$ state at Fe varies in the distribution of the LDOS compared to the state at -500 meV. The lobes in x direction are weaker and the lobes in y direction are stronger. The overlap between one lobe of the p_x state and the lobes in y direction in the opposite spin channel appears to be responsible for the bond between Fe and As_1. The overlap is smaller than in the case of -500 meV. This state does not contribute to the energy lowering in the AF structure since it is empty.

Summarizing, the plots in Fig. 5.7 show that a bond formation between Fe $d_{x^2-y^2}$ and As_1 p_x takes place. This confirms $d_{x^2-y^2}$-p_x as one of the contributing superexchange paths.

5.2 Magnetic structure of Fe[001]/InAs(110)

In this section I will discuss the magnetic structure of Fe chains on InAs(110) along the [001] direction (perpendicular to the InAs rows). The calculation was performed in the same way, with the same numerical parameters, as for the chains along InAs rows (section 5.1). In the case of Fe[001]/InAs(110) the FM structure is favourable with an energy of 80 meV. The magnetic moment of Fe in the AF case with $\mu = 2.19\,\mu_B$ is slightly lower than in the FM case with $\mu = 2.26\,\mu_B$. Unlike for Fe[1$\bar{1}$0]/InAs(110), the magnetic moments induced on InAs are negligible. The distance of 11.437 a.u. between the Fe atoms in the chain is large compared to the Fe lattice constant of 3.5 a.u.. Thus, we assume that the direct exchange between the Fe d electrons is small. Consequently, the interaction between Fe atoms is mediated in some way by InAs. From the geometry of the system shown in Fig. 4.5 (a), (b) we see that there is one In atom (In_1) directly between two Fe atoms. However, the next nearest neighbour to the Fe is As_1. This As_1 has, on a pure InAs(110) surface, a bond (bridge bond) to the In_1. The geometry opens two main possibilities for the mediation of the interaction between Fe atoms via the InAs lattice: either Fe-In_1-Fe or Fe-As_1-In_1-As_1-Fe. To test these possibilities, which are derived only from the geometry of the system, and to obtain further insight into the interaction between Fe and InAs, I will discuss the DOS of the Fe, In_1 and As_1 in the next subsection.

5.2.1 DOS of Fe[001]/InAs(110)

The DOS in the MTs of Fe, In_1 and As_1 is shown in Fig. 5.8 (a), (b) for the FM case and (c), (d) for the AF case. The geometry of the 2-D unit cell with the Fe atoms and the first layer of InAs is sketched in Fig. 5.8 (e), (f) for a better overview.

The DOS of all three atoms look very similar for the FM and for the AF structure. The spin1 Fe DOS given in Fig. 5.8 (a), (c) has a three peak structure around -2.5 eV. This structure is slightly stretched on the energy scale in the AF case in Fig. 5.8 (c) compared to the FM case Fig. 5.8 (a).

In the following I will focus on the discussion of states around E_F. The Fe DOS in the spin2 channel has one peak slightly below E_F, then a clear minimum at E_F and two large peaks between E_F and +500 meV. The energetically lower edge of these two peaks is slightly below E_F in the AF case, whereas in the FM case the minimum of the DOS is directly at E_F. The large peak below E_F can be found again as a prominent feature in the DOS of As_1 in the FM case in Fig. 5.8 (a) as well as in the AF case in Fig. 5.8 (c) in the spin1 channel, opposite to the Fe. In the AF case this As_1 peak is

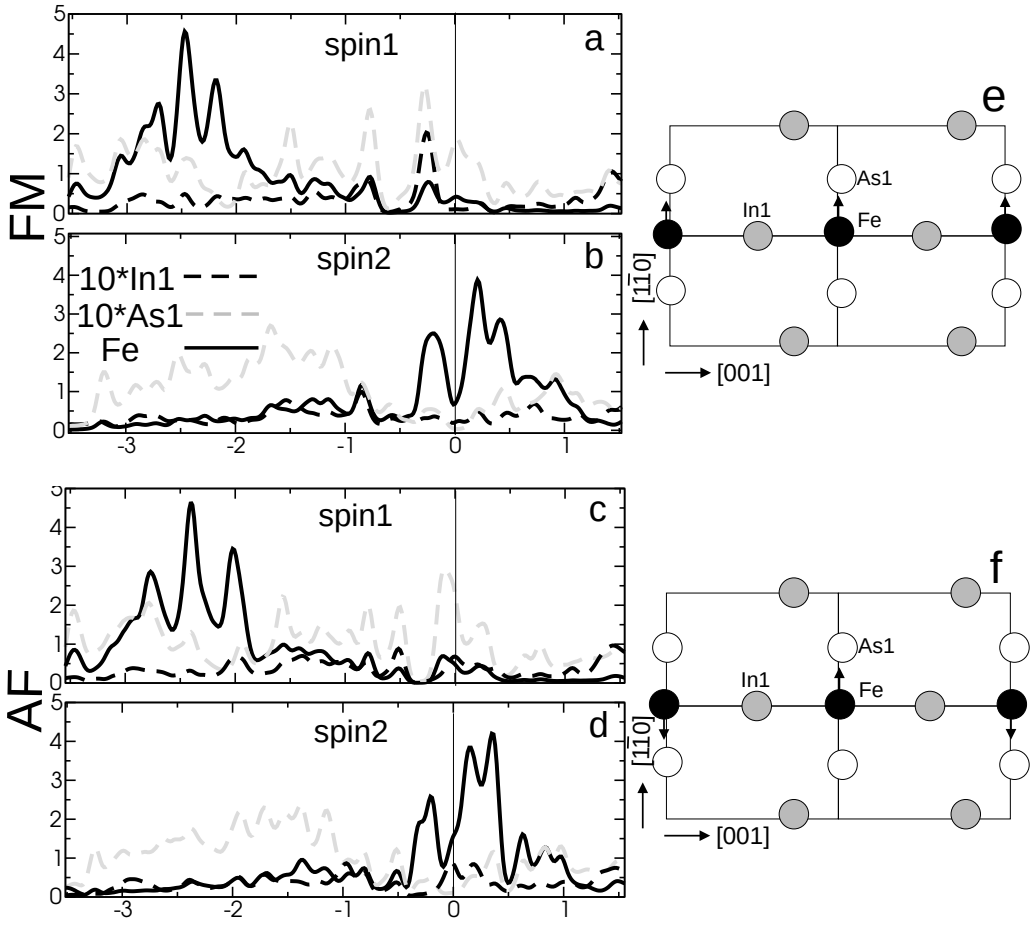

Figure 5.8: In (e) and (f) the two-dimensional projection of the geometry of the first layer of InAs with Fe-chains along [001] is shown. Detailed discussion of the geometry is given in section 4.2.3. The DOS of the atoms labeled in (e) and (f) is shown in (a)-(d). The DOS of As_1 (grey dashed) and In_1 (black dashed) is scaled by a factor of 10. The Fe DOS is plotted unscaled with a solid black line.

located at −90 meV and in the FM case at −250 meV. The energy of this As_1 state is lowered due to the interaction with the Fe state of opposite spin at −250 meV. Apparently the FM configuration of the Fe atoms in the chain benefits from this interaction. The In_1 DOS exhibits in the FM case also a state at −250 meV in the spin1 channel, which is a dominant feature in the DOS of In_1. This shows that In_1 participates in the interaction between the surface atoms at -250 meV.

To summarize, I found a state in the FM structure which exists on the three atoms Fe, In_1 and As_1 at an energy of −250 meV. This state is also present in the AF structure on Fe at −250 meV and on As_1 where it lies at −90 meV. In the FM case the interaction between Fe and As_1 apparently leads to the energy lowering of the arsenic state and also induces a state at the same energy on In_1.

The interaction between surface atoms leads to a redestribution of charge between the spin channels and as a consequence to the increase of the magnetic moment of Fe in the FM case. The minority states of Fe around E_F are depopulated in favour of the majority spin in the AF to FM transition.

From this findings the following scenario of interaction is possible. A bond between Fe and As_1 develops after adsorption of Fe on the surface. This bond leads to the AF coupling between Fe and As_1 with the same exchange mechanism as in superexchange. At the same time the As_1 is interacting with In_1. As described in section 4.2.3 the position of In_1 is relaxed to the position, which is almost equidistant between four As_1. This indicates that In_1 is interacting not only with two As_1 by means of the bridge bonds, but also very symmetrically with the As_1 of the next unit cell in the chain. Thus In_1 is coupled on two sides to the As_1 in the same way. The peaks at −250 meV in the DOS of In_1 and As_1 are in the same spin channel in Fig. 5.8 (a), which shows that this coupling is of the FM kind. Finally, the AF coupling between the As_1 of the next unit cell and the next Fe in the chain gives an overall FM coupling between the Fe atoms in the chain. This is again a kind of superexchange Fe-As_1-In_1-As_1-Fe with FM coupling between In_1 and As_1. The way of exchange between the Fe atoms Fe-In_1-Fe cannot be excluded entirely from the density of states. To investigate this exchange mechanism further I will discuss in the next section the band structure of the system.

5.2.2 Band structure of Fe[001]/InAs(110)

The band structure of Fe chains on InAs(001) with the chain direction perpendicular to the InAs rows (Fe[001]/InAs(110)) is plotted in Fig. 5.9. The first row, Fig. 5.9 (a) and (b) corresponds to the FM structure and the second row, Fig. 5.9 (c) and (d) to the AF structure. All states of the atoms, which

can contribute to the exchange between Fe atoms in the chain are marked. Fe states are marked with diamonds, As_1 states with squares and In_1 states with crosses.

The FM case of Fig. 5.9 (a), (b) will be discussed first. All marked bands are degenerate along $\overline{\mathrm{MX}}$. The reason for this is the calculation of the FM structure with doubled unit cell. The chain direction is along $\overline{\Gamma\mathrm{X}}$. So $\overline{\mathrm{MX}}$ is the edge of the quasi one-dimensional BZ. The backfolding of the bands through the doubled unit cell results in their degeneracy along the edge of the quasi one-dimensional BZ.

There are three As_1 bands and one In_1 band in the vicinity of the Fermi energy in Fig. 5.9 (a). Two of the As_1 bands, which are degenerate along $\overline{\mathrm{MX}}$ intersect the Fermi energy. These bands contribute to the peak at E_F in the As_1 DOS. One of the As_1 bands has a minimum at $\overline{\mathrm{Y}}$ around -300 meV. The completely occupied As_1 band and the In_1 band have a maximum at $\overline{\mathrm{Y}}$ with energies of -280 meV and -250 meV respectively. The energies of these extrema and the low dispersion of the bands along $\overline{\mathrm{YM}}$ and $\overline{\mathrm{MX}}$ lead to the conclusion that the peak in the As_1 and In_1 DOS at -250 meV is caused by these bands. The occupied As_1 band is degenerate along $\overline{\mathrm{MX}}$ and almost degenerate along $\overline{\mathrm{YM}}$ with the In_1 band. This means that the interaction between these two bands is possible and they originate from one band in the halved original unit cell.

Four Fe bands are visible in Fig. 5.9 (b) around the Fermi energy. One of them is occupied along $\overline{\mathrm{MX}}$ and unoccupied along the $\overline{\mathrm{GY}}$, $\overline{\mathrm{YM}}$ and $\overline{\mathrm{XG}}$. This band is degenerate along $\overline{\mathrm{MX}}$ with another one which is completely occupied. Both are nearly dispersionless with an energy of -100 meV along $\overline{\mathrm{MX}}$. The completely occupied band descends to the energy of -200 meV along $\overline{\mathrm{X\Gamma}}$ and to the energy of -600 meV and further to -900 meV along $\overline{\mathrm{MY}}$ and $\overline{\mathrm{Y\Gamma}}$. From the splitting and dispersion of these bands along the chain, $\overline{\mathrm{X\Gamma}}$ and $\overline{\mathrm{MY}}$, we conclude, that their contribution to the interaction along the chain is quite large.

Another two of the four Fe bands are degenerate and almost completely dispersionsless, not only along $\overline{\mathrm{MX}}$ but also along $\overline{\mathrm{MY}}$ at an energy of -250 meV. This means, that these bands contribute less than the two others to the interaction along the chain. Nevertheless, they have almost the same energy as the degenerate In and As bands in Fig. 5.9 (a). The conclusion is that although these Fe states interact with As_1 and In_1 states at -300 meV, this interaction does not mediate the interaction between Fe atoms in the chain. All Fe bands around E_F are almost flat along $\overline{\Gamma\mathrm{Y}}$ and $\overline{\mathrm{MX}}$. This means that the interaction between the Fe atoms perpendicular to the chains is weak.

To summarize the discussion of the FM band structure, I identified the

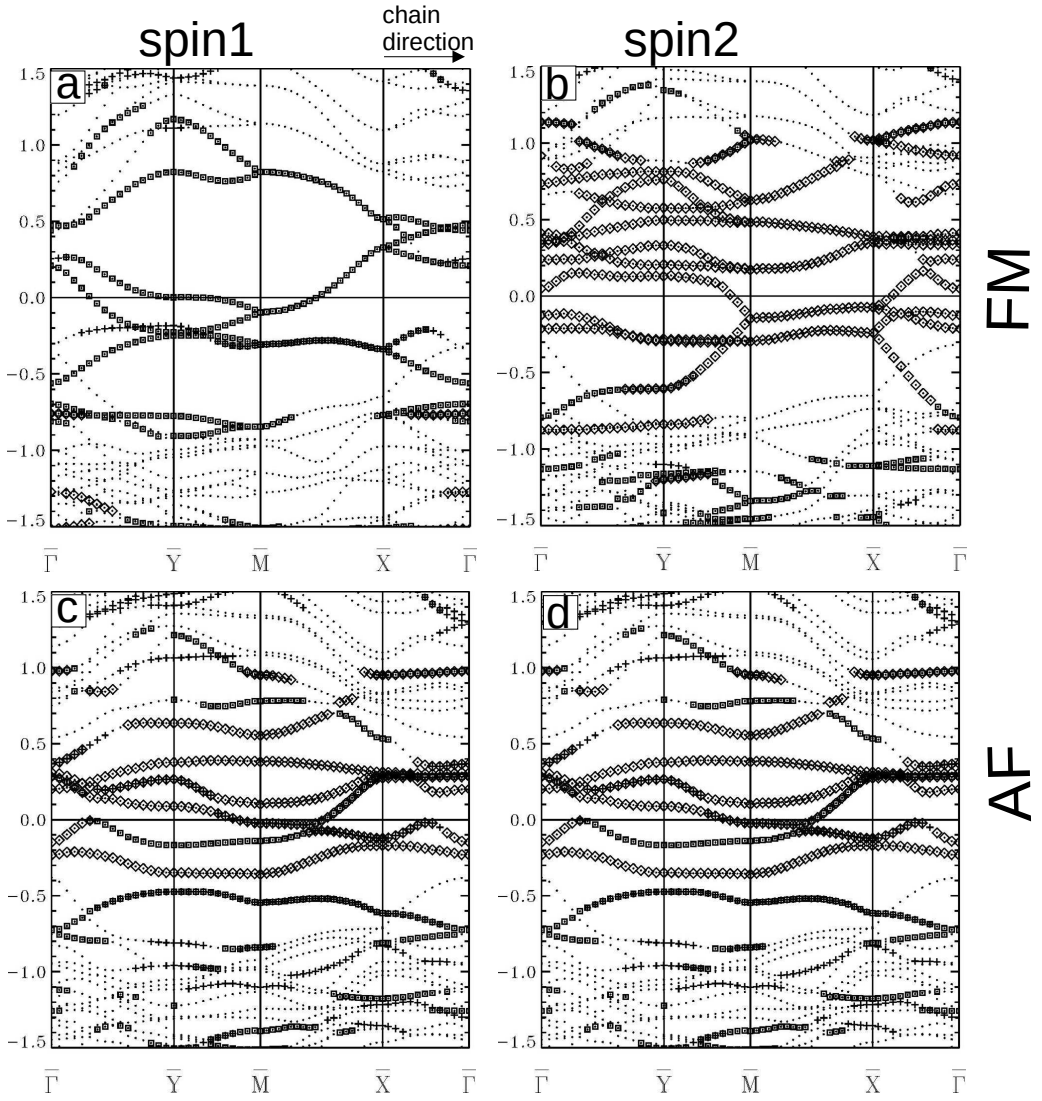

Figure 5.9: (a), (b) - the band structure of Fe[001]/InAs(110) in the FM configuration. (c), (d) - the band structure of the Fe[001]/InAs(110) in the AF configuration. Three kinds of states are marked, the Fe states with diamonds, the As states with squares and the In states with crosses.

bands contributing to the state at -250 meV in Fig. 5.8. The coinciding energetic position of those bands confirms the strong interaction between them. Additionally, I have shown that only parts of these bands mediate the interaction between Fe atoms along the chains.

Next, I analyse the band structure of the AF configuration shown in Fig. 5.9 (c), (d). Six bands are marked around E_F in Fig. 5.9 (c). They all are almost flat along the chain. Differently to the FM case with the maximal dispersion of 500 meV along the chain, in the AF case the maximal dispersion is 100 meV. The lowest of the marked bands has In and As character at the same time. Its energy lies between -700 and -500 meV. This band is split off from another occupied InAs band, which has an energy of -100 meV. The InAs band at -100 meV hybridizes with two Fe bands at the $\overline{\mathrm{X}}$ point and at an energy of -200 meV, and between $\overline{\mathrm{M}}$ and $\overline{\mathrm{X}}$ almost at the Fermi energy. The InAs band at -100 meV is marked with squares (arsenic band) from $\overline{\Gamma}$ to the point of hybridization between $\overline{\mathrm{M}}$ and $\overline{\mathrm{X}}$. From this point further to the $\overline{\mathrm{X}}$ and $\overline{\Gamma}$ the arsenic band becomes unoccupied through the hybridization with a mainly unoccupied Fe band. The InAs band at -100 meV is marked with crosses from the point of hybridization between $\overline{\mathrm{M}}$ and $\overline{\mathrm{X}}$ to $\overline{\mathrm{X}}$ and further to $\overline{\Gamma}$. From $\overline{\mathrm{M}}$ in the direction towards $\overline{Y}$ the In states become unoccupied. Thus the point of hybridization between $\overline{\mathrm{M}}$ and $\overline{\mathrm{X}}$ can be viewed as a cross point of Fe, In and As states. Different to this hybridization the occupied Fe band at -250 meV hybridizes only with In_1 states of the InAs band at -100 meV.

In the following section, I discuss the LDOS of the system in order to get further insights into the interaction mechanism between Fe atoms on InAs(110) in the FM case. In particular, I will look for the confirmation or counterevidence of the hypothesis, that the interaction between the Fe atoms in the chain works mainly along two paths: one of them being Fe-As_1-In_1-As_1-Fe with Fe-As_1 AF superexchange and the other being Fe-In_1-Fe.

5.2.3 Symmetry of the interaction states

In the previous section the bands contributing to the DOS peaks at -250 meV were identified. As an example of the DOS distribution in those interacting bands the LDOS of the state at $\overline{M}$ at -300 meV is plotted in Fig. 5.10 and the LDOS of the state at -100 meV in Fig. 5.11.

In Fig. 5.10 (c2) a d_{yz} state on Fe is clearly visible. Fig. 5.10 (a2) shows a slightly tilted p_z state on As_1. The symmetry of the states allows a π bond between them, which is shown in Fig. 5.10 (b2). This confirms the AF

interaction between Fe spin2 and As_1 spin1 via these states. Figure 5.10 (a1) shows a p_z state on As_1, which is slightly bend into the $(1\bar{1}\bar{1})$ direction. The LDOS on In_1 pictured in the same panel has sp_z character. Due to the small overlap between $sp_z(In_1)\uparrow$ with the outward directed lobe of the $p_z(As_1)\uparrow$ at one side and with the inward directed lobe of the $p_z(As_1)\uparrow$ at another side the FM interaction between these states is rather weak.

In Fig. 5.10 (a3)-(c3) the LDOS distribution is dominated by the spin1 channel as well on the Fe as on the In_1. This corresponds on the Fe to the minor peak at -250 meV and on the In_1 to the large peak at -250 meV in Fig. 5.8 (a). The LDOS on the In_1 has sp_z character. The state at the Fe is a linear combination of the d-states with a triangular shape. Two angles of this triangle point towards the In_1 in Fig. 5.10 (a3). These facts confirm a weak FM coupling between the Fe and the In_1, which is mediated through the spin1 states.

In summary, the interaction Fe$\downarrow$-$As_1\uparrow$-$In_1\uparrow$-$As_1\uparrow$-Fe$\downarrow$ between the Fe atoms in the chain via a state at -250 meV is confirmed. Differently to the Fe$\downarrow$-$As_1\uparrow$ with a strong coupling, the interaction $As_1\uparrow$-$In_1\uparrow$ is weak due to the small overlap between the $sp_z(In_1)\uparrow$ and the $p_z(As_1)\uparrow$ states. Additionally the FM interaction Fe$\uparrow$-$In_1\uparrow$-Fe$\uparrow$ is confirmed.

Next, the LDOS of the state at $\overline{M}$ at the energy of -100 meV, shown in Fig. 5.11 will be discussed. This state contributes, like the state at -300 meV, to the peak at -250 meV in Fig. 5.8 (b) at the Fe. Differently to the state at -300 meV the contribution to the DOS of the In_1 is negligible in the spin1 channel and very small in the spin2 channel. At the As_1 this state exists in the spin1 channel and is visible in the DOS of Fig. 5.8 (a) as a peak at the Fermi energy.

Figures 5.11 (a1)-(c1) show a tilted $p_z(As_1)\uparrow$ and $p_{[1\bar{1}\bar{1}]}$ $(In_1)\downarrow$ states. These states form a σ bond between the In_1 and the As_1 with AF coupling, opposite to the FM coupling at -300 meV. Figures 5.11 (a2)-(c2) show a tilted $p_z(As_1)\uparrow$ state and a linear combination of d-states on the Fe in the spin2 channel. The character of this linear combination cannot be determined in this case. The states at the Fe and at the As_1 couple antiferromagnetically likewise in the state at -300 meV. The bond between Fe and As_1 is a σ bond, differently to the state at -300 meV in Fig. 5.11 (a2)-(c2). In Fig. 5.11 (b3)-(c3) a large intensity of the LDOS at the Fe atoms, which interacts ferromagnetically with the state $p_{[1\bar{1}\bar{1}]}(In_1)\downarrow$, is visible. In summary, the FM coupling is mediated between Fe atoms in the chain via Fe$\downarrow$-$In_1\downarrow$-Fe$\downarrow$ and Fe$\downarrow$-$As_1\uparrow$-$In_1\downarrow$-$As_1\uparrow$-Fe$\downarrow$ for this state. The $p_{[1\bar{1}\bar{1}]}$ $(In_1)\downarrow$ character of the state at In_1 allows large overlap to the tilted $p_z(As_1)\uparrow$. Probably this leads to the stronger coupling than the coupling at -300 meV in spite of the lower

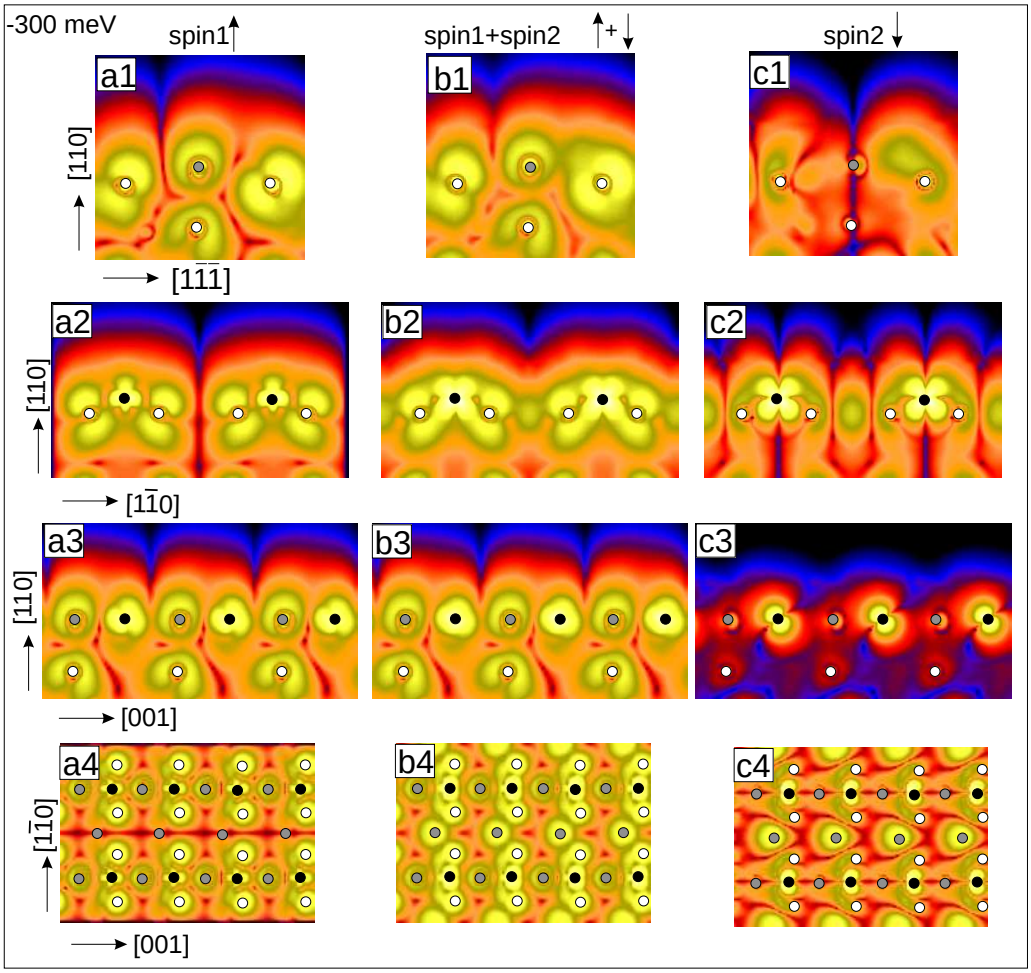

Figure 5.10: Density plots of the state at $\overline{\mathrm{M}}$ at -300 meV. Directions are indicated at the borders. The spin1 channel of the system (↑) is shown in panels (a), spin1+spin2 in (b), and the spin2 channel (↓) in (c). The panels (a1)-(c1) show the (1$\bar{1}$1) plane, (a2)-(c2) the (001) plane, (a3)-(c3) the (1$\bar{1}$0) plane, and (a4)-(c4) the (110) plane. The Fe atoms in the planes are marked with black circles, As atoms with white circles, and In atoms with grey circles.

DOS at In_1.

Next, I will describe the coupling between the chains. Figure 5.11 (a4)-(c4) indicates an interaction Fe↓-As_1↑-As_1↑-Fe↓ between the chains, whereas in Fig. 5.10 (a4)-(c4) this interaction is mediated via the In_2. According to the band structure with the low dispersion of the bands perpendicular to the chain direction the corresponding interaction is very low. The LDOS plots

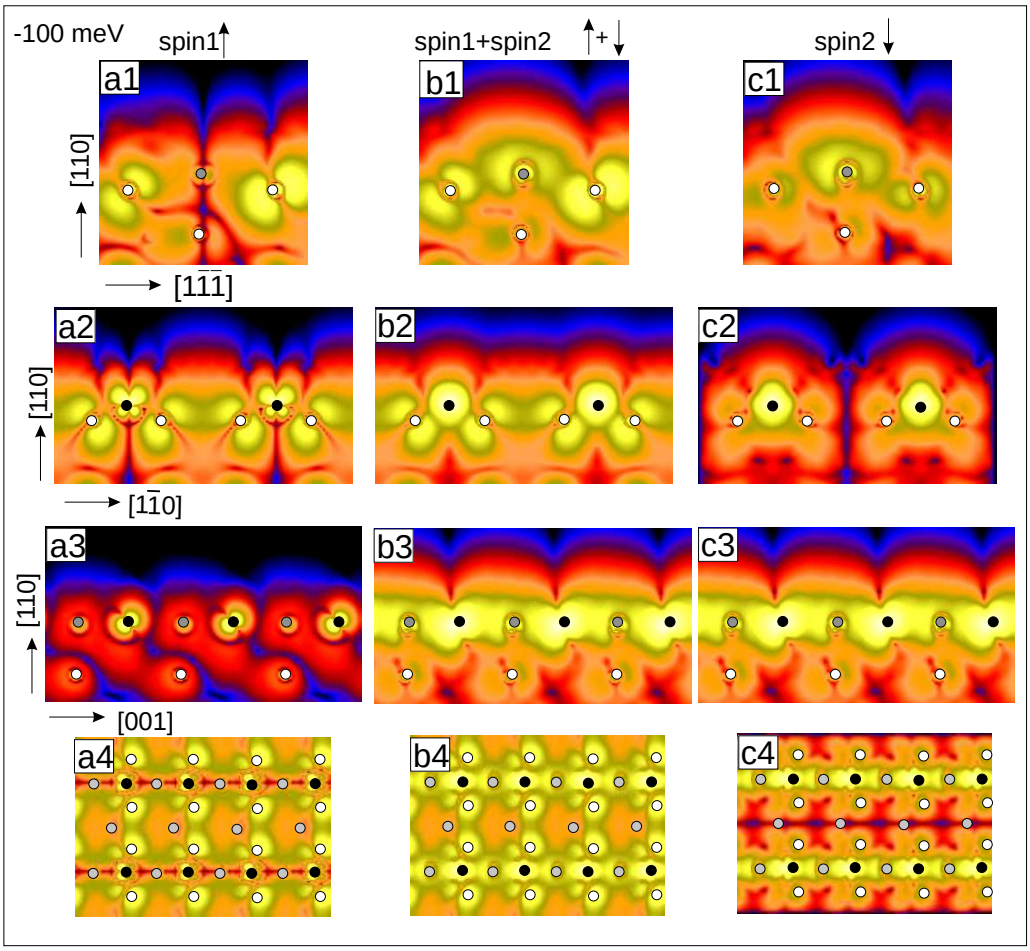

Figure 5.11: Density plots of the state at $\overline{\mathrm{M}}$ at -100 meV. Directions are indicated at the borders. The spin1 channel of the system (↑), is shown in panels (a), spin1+spin2 in (b), and the spin2 channel (↓) in (c). The panels (a1)-(c1) show the (1$\bar{1}$1) plane, (a2)-(c2) the (001) plane, (a3)-(c3) the (1$\bar{1}$0) plane, and (a4)-(c4) the (110) plane. The Fe atoms in the planes are marked with black circles, As atoms with white circles, and In atoms with grey circles.

reveal that the small overlap of the corresponding orbitals leads to the weak interaction.

Chapter 6

Simulation of the STM measurements

6.1 Simulation of STS on Fe multimers

The local density of states on and around a single Fe atom (monomer) and Fe multimers deposited on n-InAs(110) surfaces was studied experimentally by scanning tunneling spectroscopy at $T \sim 6$ K. Fe dimers, trimers and tetramers both perpendicular and parallel to the InAs rows were formed by evaporating Fe atoms on a clean InAs(110) surface at room temperature. The multimers perpendicular to the InAs rows are closely packed. One Fe atom is adsorbed in every unit cell with a separation between the Fe atoms of 11.435 a.u.. The parallel multimers on the other hand are stable only if one Fe atom is adsorbed in every second unit cell of InAs. This leads to a separation of 16.17 a.u. between the Fe atoms. Further experimental details are presented in [30].

The spectroscopy curves measured on a tetramer parallel to the InAs rows, i.e. along $[1\bar{1}0]$, and on a trimer perpendicular to the InAs rows, i.e. along [001], are shown in Fig. 6.1. In Fig. 6.1 (a) three curves measured on the different atoms of the Fe trimer are presented. Additionally, the spectrum of the substrate is shown as a thin dashed line. The topography of the corresponding structure as measured at U_B=0.1 V is shown in Fig. 6.1 (b). All three curves in Fig. 6.1 (a) have a two peak structure. The energies of the lower peak are $E(Fe1)_1$=0.73 eV, $E(Fe2)_1$=0.83 eV, $E(Fe3)_1$=0.87 eV and for the higher peak $E_2(Fe1)$=1.15 eV, $E_2(Fe2)$=1.0 eV, $E_2(Fe3)$=1.09 eV. The lower peak can also be found on the substrate at 0.88 eV. The contrast

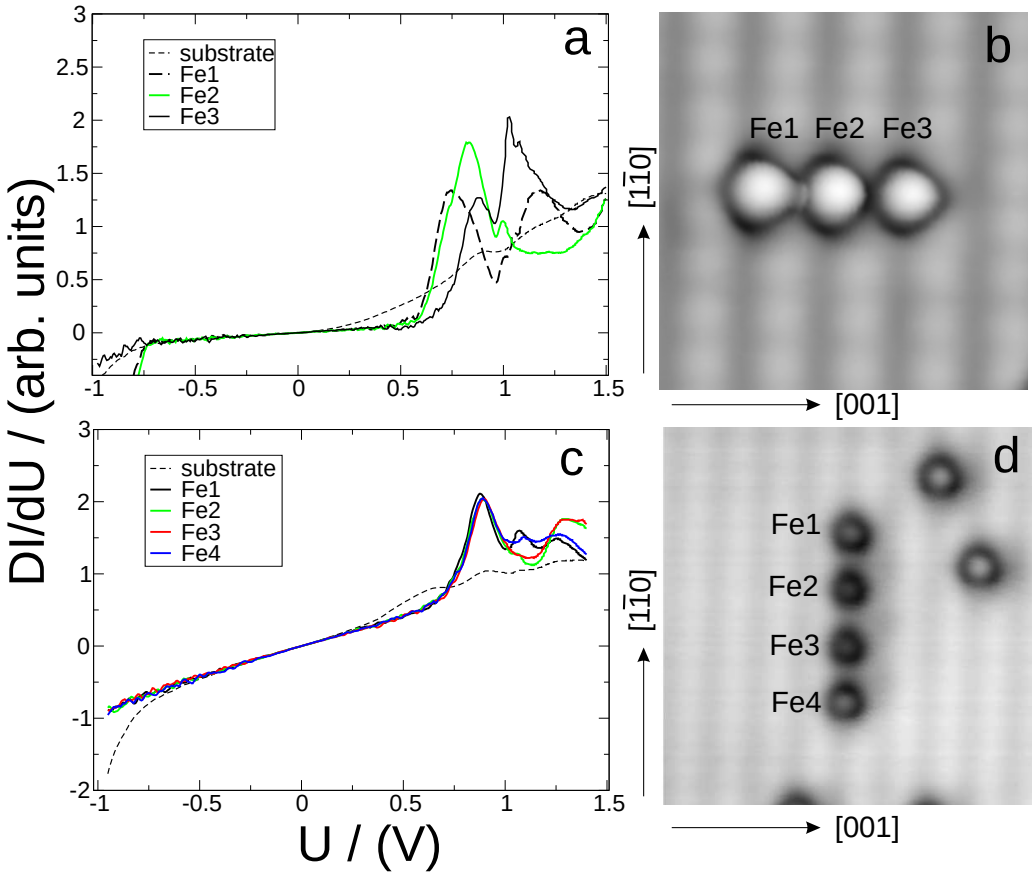

Figure 6.1: (a), (c) Experimentally obtained spectroscopy curves on Fe multimers. (b), (d) The topographic CCM image of the corresponding multimer at a bias of 100 meV. The spectrum of the substrate is shown with a thin dashed line. Other curves correspond to the atoms marked in (b) and (d).

between two peaks defined as

$$C = \frac{DOS(E_2) - DOS(E_1)}{DOS(E_2) + DOS(E_1)}$$

is $C_{Fe1} = 0$, $C_{Fe2} = -0.27$, $C_{Fe3} = 0.25$.

The spectroscopy curves obtained on the tetramer parallel to the InAs rows are shown in Fig. 6.1 (c) together with the substrate spectroscopy. The topography of the corresponding structure as measured at U_B=0.1 V is visible in Fig. 6.1 (d). The spectroscopy curves of the two middle Fe atoms have two peaks: one at 0.87 eV and one at 1.28 eV with the same contrast of -0.06 for both atoms. The first of these peaks can be found again in the spectroscopy of the substrate. The edge atoms exhibit an additional state at 1.07 eV. This additional peak is apparently the end state of the tetramer.

To understand these results I plotted in Fig. 6.2 the vacuum DOS of the Fe[1$\bar{1}$0]/InAs(110) and Fe[001]/InAs(110) in the FM and AF configuration. The DOS is averaged at a distance of 10 a.u. from the surface over the 2D unit cell. The energetically favoured configurations are Fe[1$\bar{1}$0]/InAs(110) AF shown in Fig. 6.2 (c) and Fe[001]/InAs(110) FM shown in Fig. 6.2 (b). Both systems have two peaks in the vacuum DOS in the neighbourhood of 1 eV.

The DOS of Fe[001]/InAs(110) FM in Fig. 6.2 (b) has a small peak at 1.1 eV and a large peak at 1.5 eV. The large peak has a double peak structure with a larger part at 1.44 eV coming from the majority spin and a lower part originating from the minority spin at 1.63 eV. The contrast between majority spin and minority spin contributions to the higher peak changes from 0.133 at the distance of 1 a.u. from the surface to 0.053 at the distance 14 a.u. from the surface. This leads to the asymmetric form of the peak in the sum of the majority and minority spin DOS at the lower distances to the surface. The contrast between the peak at 1.1 eV and the peak at 1.5 eV is 0.52.

The Fe[1$\bar{1}$0]/InAs(110) AF has a peak at 0.83 eV and one at 1.23 eV. The contrast between two peaks is 0.27. Thus in the system with the Fe chains along the InAs rows the peaks are shifted to the lower energies and the contrast between the peaks is reduced, compared with Fe chains perpendicular to the InAs rows.

Comparison between calculated vacuum DOS and experimental data shows that both have two peaks around 1 eV for the case Fe[1$\bar{1}$0]/InAs(110) as well as for the case Fe[001]/InAs(110). The exact energies and contrasts are different probably due to the finite length of the multimeres in the experiment. Another cause for the differences in the calculated and measured vacuum DOS can be the distance between the Fe atoms in the Fe[1$\bar{1}$0]/InAs(110),

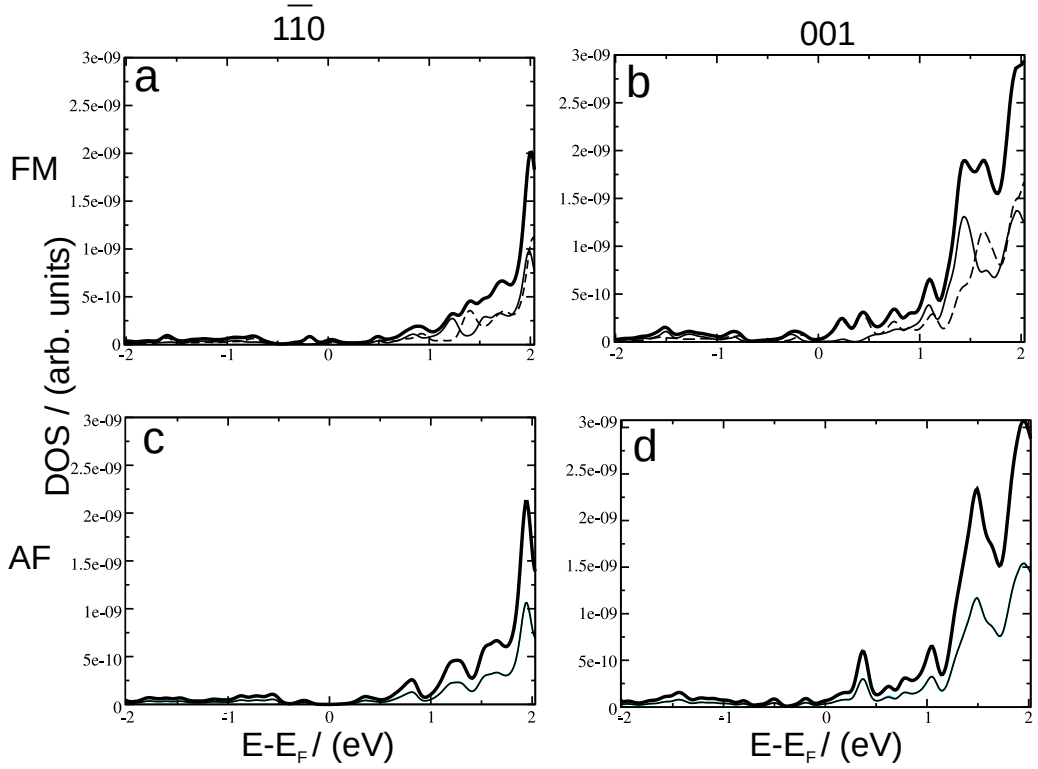

Figure 6.2: Calculated DOS in the vacuum at a distance of 10 a.u. from the surface. The DOS is averaged over the complete 2D unit cell. The left column (a), (c) shows the vacuum DOS of Fe[1$\bar{1}$0]/InAs(110). The right column (b), (d) - the vacuum DOS of Fe[001]/InAs(110). (a), (b) corresponds to the FM configuration with spin1 shown with a thin solid line, spin2 with a thin dashed line, and the sum of the both spins with a thick solid line. (c), (d) corresponds to the AF configuration. Due to the averaging over a unit cell the DOS of spin1 and spin2 are equal. The thick line corresponds to the sum of both spin channels.

which is half of the distance between the Fe atoms in the multimers along [1$\bar{1}$0].

The only case in the measurement with a positive contrast between two peaks is the spectroscopy on a perpendicular trimer at Fe3 (Fig. 6.1 (a)). A striking feature of this spectroscopy data is also the strong asymmetry of the peak at 1.09 eV. According to the calculation this can be explained with the double structure of the peak and a weaker contribution of the minority spin to the energetically higher part of the state. The contrast in the case of the parallel tetramer is negative for both middle atoms. The calculations reproduce

this trend. This means that the contrast between the two peaks is reduced from Fe[001]/InAs(110) (perpendicular case) to Fe[1$\bar{1}$0]/InAs(110)(parallel case).

Up to now, two states around 1 eV are identified, in the measured spectroscopies as well as in the calculated vacuum DOS. The agreement in the energetical positions of the calculated and measured states is reasonable. The difference in the contrast can be explained with different distances to the surface in the calculation versus the experiment. Another reason for the different contrast could be the difference in the geometry between the experiment and the theory. The strongly asymmetric form of the peak with higher energy at Fe3 in Fig. 6.1 (a) is explained by different contributions of two slightly split minority and majority states at this energy. In the next subsection I will determine the character of the states around 1 eV.

6.2 Vacuum states

To identify the atoms, which contribute to the vacuum DOS around 1 eV, I plotted in Fig. 6.3 the LDOS of Fe[001]/InAs(110) for the states at 1.1 eV 1.4 eV and 1.6 eV. In the first three rows the LDOS in the vacuum at the distance 10 a.u. from the surface is plotted. For all three states the LDOS has a maximum along Fe chains. For the state at 1.1 eV the LDOS along the chain has maxima at the positions of the In atoms. For the states at 1.4 eV and 1.6 eV the LDOS along the chain has maxima at the positions of the Fe atoms. This means, that for the multimers perpendicular to the InAs rows the lower vacuum state at 1.1 eV is located at In and the higher one at 1.5 eV at Fe. If we recall that at the pure InAs(110) surface the In DB is located at 0.9 eV, the In vacuum state around 1 eV becomes very plausible as a rudiment of the In DB. In Fig. 6.3 (a4)-(a6), (b4)-(b6), (c4)-(c6) a plane through the film is plotted. In Fig. 6.3 (a4)-(c4) it is visible, that the state at 1.1 eV is indeed the In DB, whereas the states at 1.4 eV and 1.6 eV in Fig. 6.3 (a5)-(c5) and (a6)-(c6) are the Fe minority, respectively majority states.

Similar for the system Fe[1$\bar{1}$0]/InAs(110) the LDOS of the states at 0.8 eV and 1.2 eV is plotted in Fig. 6.4. In Fig. 6.4 (b1) the maxima of the LDOS are located at the positions of In atoms. Differently in Fig. 6.4 (b2) the maxima are shifted to the Fe atoms. Due to the buried position of the Fe atoms, described in section 3.1.1, the maximum of the LDOS in Fig. 6.4 (b2) is not directly above the Fe atoms. Fig. 6.4 (b4) demonstrates that the state at 1.2 eV on the Fe is directed to the surface and further to the vacuum. However, In is relaxed far outwards, and therefore still plays a significant

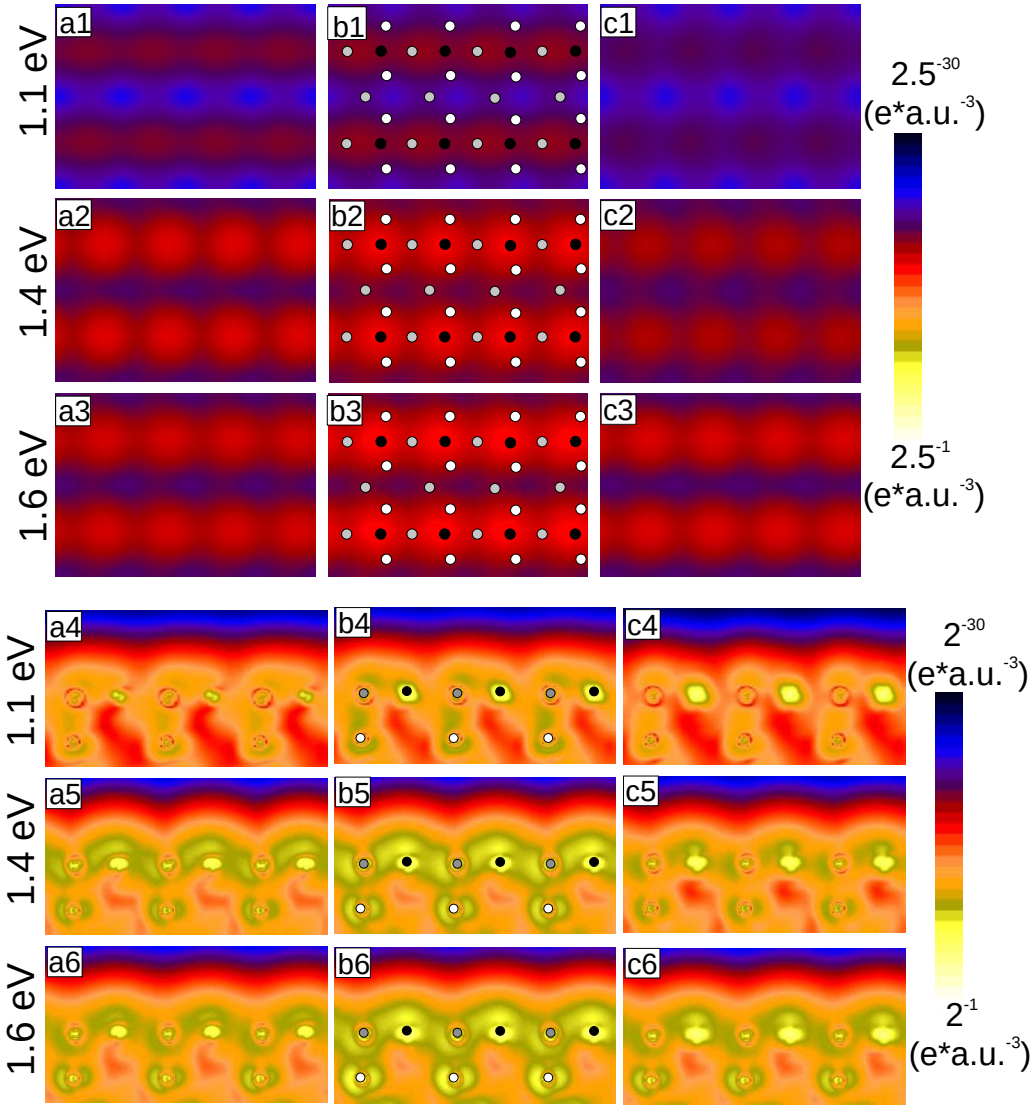

Figure 6.3: The LDOS of the vacuum states of the FM system Fe[001]/InAs(110) is shown. (a1)-(c1), (a2)-(c2) and (a3)-(c3) the LDOS distribution at the distance 10 a.u. from the surface. (a4)-(c4), (a5)-(c5) and (a6)-(c6) the LDOS in the $(1\bar{1}0)$-plane for the corresponding states is shown. In the left column (a) spin1, in the right (c) - spin2, and in the middle (b) the sum of both spin channels are presented.

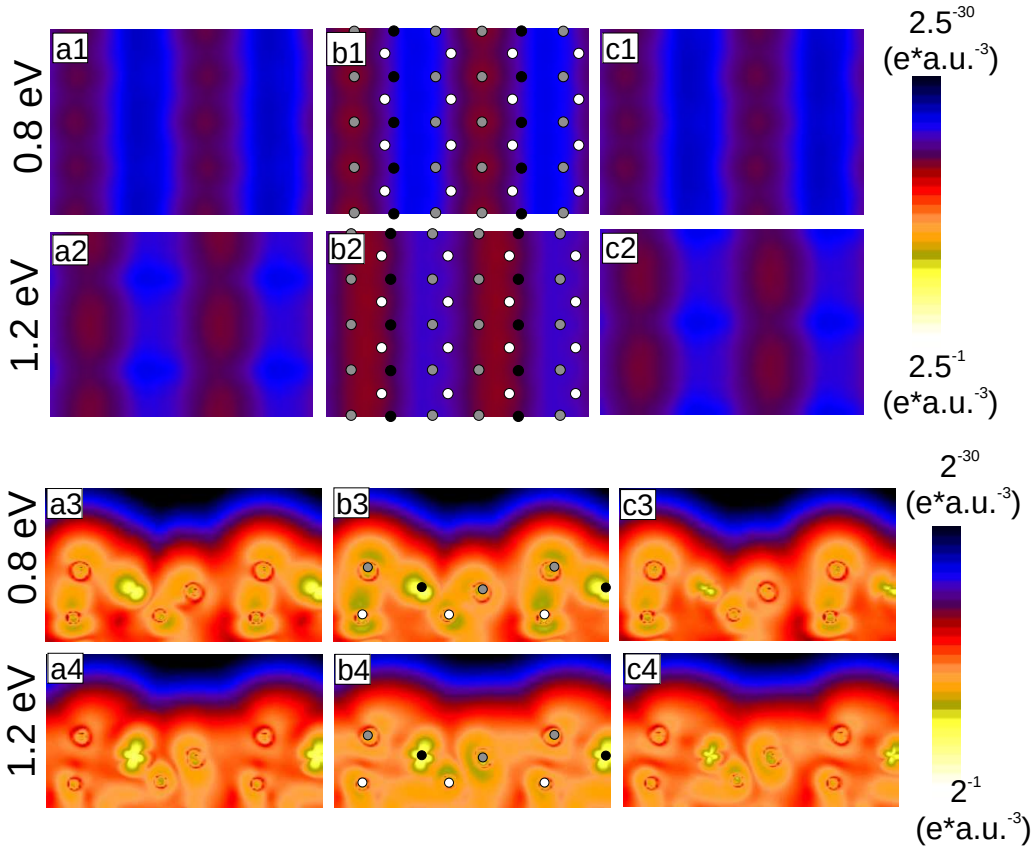

Figure 6.4: The LDOS distribution of the vacuum states of the system Fe[1$\bar{1}$0]/InAs(110) is shown. (a1)-(c1), (a2)-(c2) and (a3)-(c3) the LDOS distribution at the distance 10 a.u. from the surface. (a4)-(c4), (a5)-(c5) and (a6)-(c6) the LDOS in the (1$\bar{1}$0) plane for the corresponding states is shown. In the left column (a) spin1, in the right (c) - spin2, and in the middle (b) the sum of the both spin channels are presented.

role for the vacuum LDOS. Fig. 6.4 (b3) shows that the state at 0.8 eV at In comes indeed fom the In DB. At Fe this state is located mainly in the plane of the Fe and three adjacent As atoms.

In this section I determined the character of the vacuum states around 1 eV. The lower state is the rudiment of the In DB for the case of Fe[1$\bar{1}$0]/InAs(110) as well as for the case of Fe[001]/InAs(110). This can be supported by the experimental data, where the lower state in the spectroscopic data exists not only on the multimers, but also on the substrate. The higher state is located in both cases on Fe, whereas in the FM case of Fe[001]/InAs(110) the higher state is slightly spin-split. In the next section I analyse the topography of

Fe[1$\bar{1}$0]/InAs(110) and Fe[001]/InAs(110) to see if and how it is influenced by these vacuum states.

6.3 Topography of Fe[1$\overline{1}$0]/InAs(110) and Fe[001]/InAs(110)

To encourage further systematic experimental studies of Fe chains on InAs(110) we present in Fig. 6.5 - Fig. 6.7 and Fig. 6.8 - Fig. 6.10 an overview of the calculated topographic images of Fe[1$\bar{1}$0]/InAs(110) and Fe[001]/InAs(110) for a wide energy range. The images are simulated at the distance 10 a.u. from the surface. Due to the band maximum in Fig. 5.4 at -100 meV at $\overline{\Gamma}$ the As_1 atoms are imaged at this particular energy. At the lower voltages, between -200 meV and -600 meV the Fe band at -200 meV in Fig. 5.4, which corresponds to a $d_{z^2-r^2}$ state, determines the topography. This leads to the preferential imaging of Fe atoms, despite their position deep in the surface. At -600 meV and lower voltages the outward relaxation of the In_1 prevails all effects of the electronic structure, so that the In_1 atom is imaged at these voltages. The In_1 atom is also imaged at all positive voltages. This means, that the Fe state at 1.2 eV is visible in the spectroscopic measurements, however, not in the topographic images.

In Fig. 6.8 - Fig. 6.10 the calculated topography images of the system Fe[001]/InAs(110) are presented. The patterns consist of stripes along the Fe chains almost at all voltages. The maxima in these stripes are at the positions of the In_1 atoms at negative voltages, and beginning from 300 meV up to higher voltages at the positions of the Fe atoms. The In vacuum state at 1.1 eV is noticeable only in the more elongated form of the maxima along the stripes compared with the image at 1.5 eV. An interesting deviation from the pattern, consisting of the stripes along the Fe-chains is visible between -200 meV and 200 meV. At these voltages the image of the minority spin channel exhibits a kind of fish-bone pattern. At -100 meV and 100 meV the maximum is shown at the interstitial position.

Despite the absence of a systematic experimental study of Fe multimers with STM some results presented in [24, 30] demonstrate that at low voltages Fe atoms are surrounded by a black rim, whereas at higher voltages the black rim disappears. This is qualitatively reproduced in the calculation of the Fe[001]/InAs(110). Thus the Fe chains perpendicular to the InAs rows are more suitable to model the Fe monomers, than the Fe chains along the InAs rows.

Summarizing, we have shown, that for the Fe chains parallel to

the InAs rows the Fe atom is imaged only at low negative voltages. For the Fe chains perpendicular to the InAs rows the Fe atom is imaged at positive voltages higher than 300 meV, whereas at negative voltages the In atom shows up in the topography image.

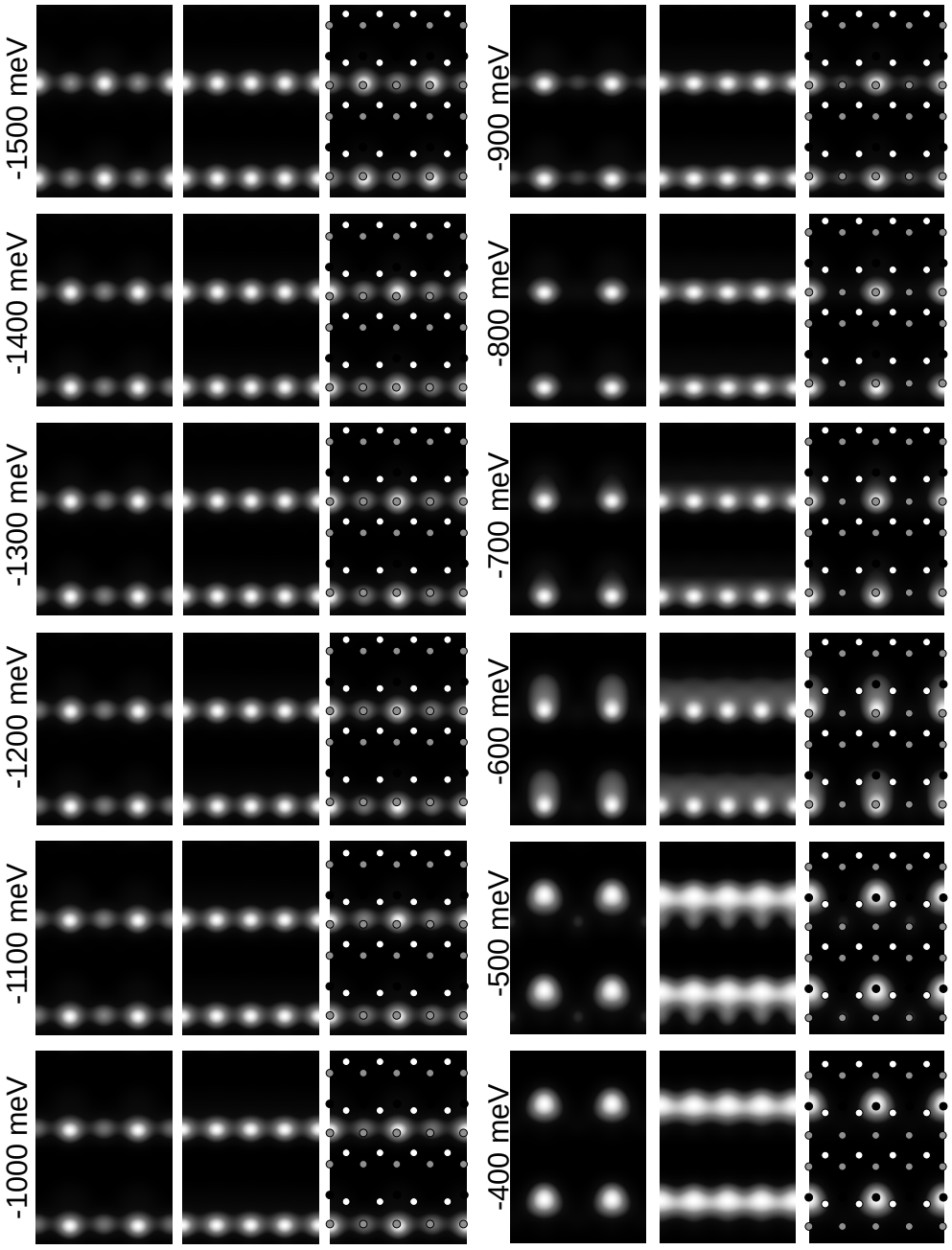

Figure 6.5: Topographic images at negative voltages for Fe[1$\bar{1}$0]/InAs(110) at a distance of 10 a.u. from the surface. The spin1 channel is presented in the left column, the spin2 channel - in the right and the sum of both spin channels in the middle. The position of the atoms is indicated in the right column: Fe with black circles, As with white, and In with grey.

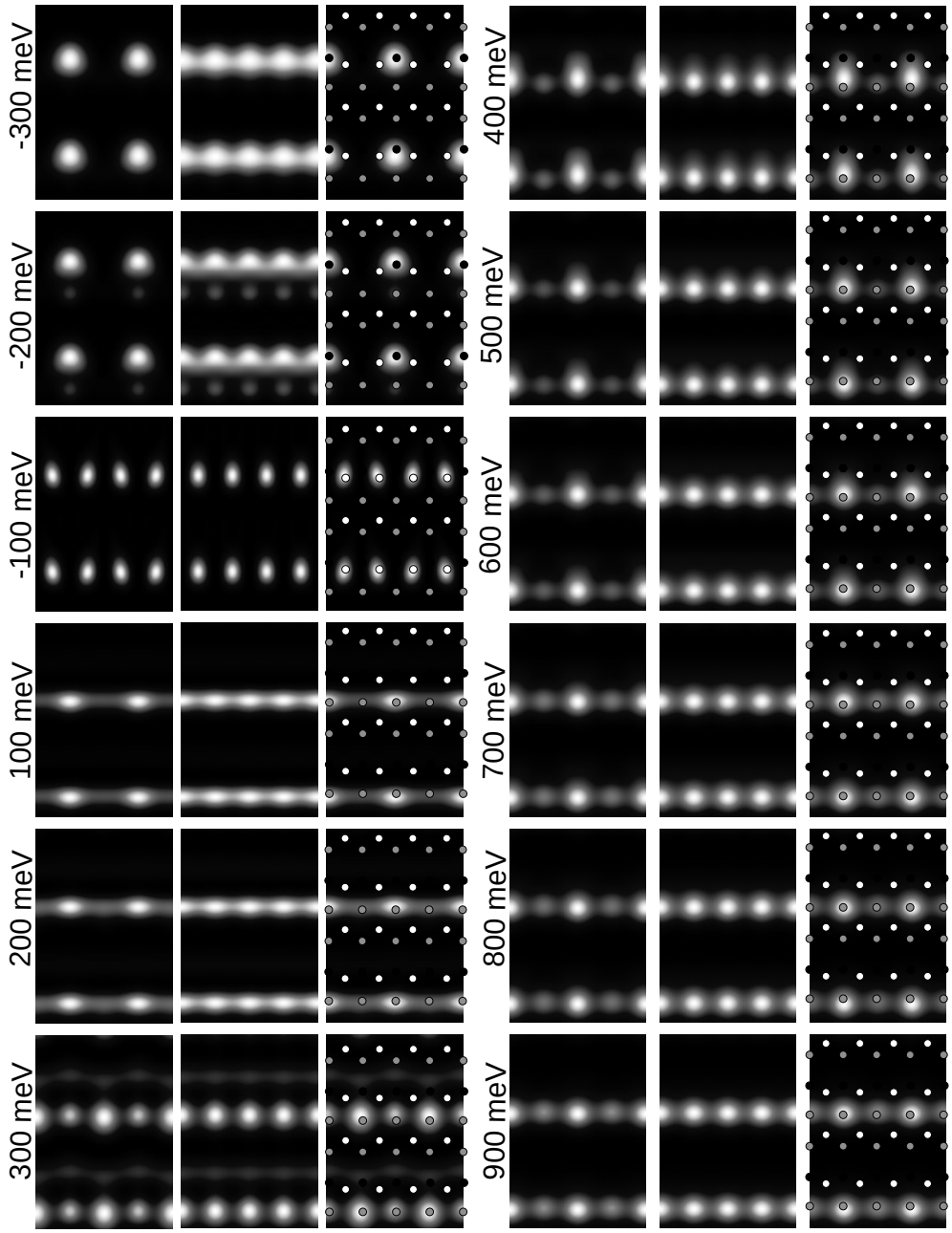

Figure 6.6: Topographic images around E_F for Fe[1$\bar{1}$0]/InAs(110) at a distance of 10 a.u. from the surface. The spin1 channel is presented in the left column, the spin2 channel - in the right and the sum of both spin channels in the middle. The position of the atoms is indicated in the right column: Fe with black circles, As with white, and In with grey.

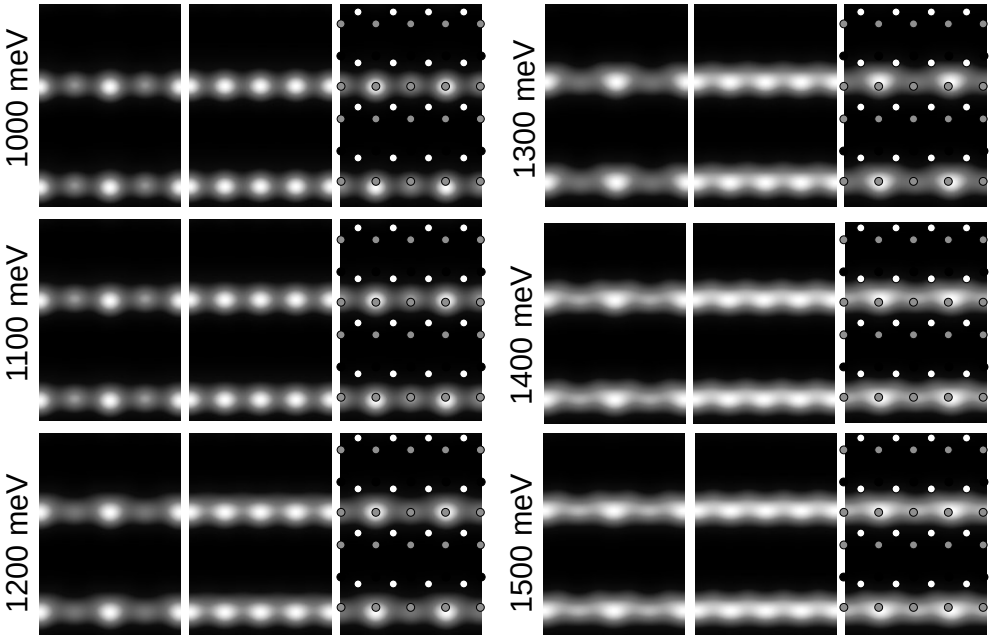

Figure 6.7: Topographic images at large positive voltages for Fe[1$\bar{1}$0]/InAs(110) at a distance of 10 a.u. from the surface. The spin1 channel is presented in the left column, the spin2 channel - in the right and the sum of both spin channels in the middle. The position of the atoms is indicated in the right column: Fe with black circles, As with white, and In with grey.

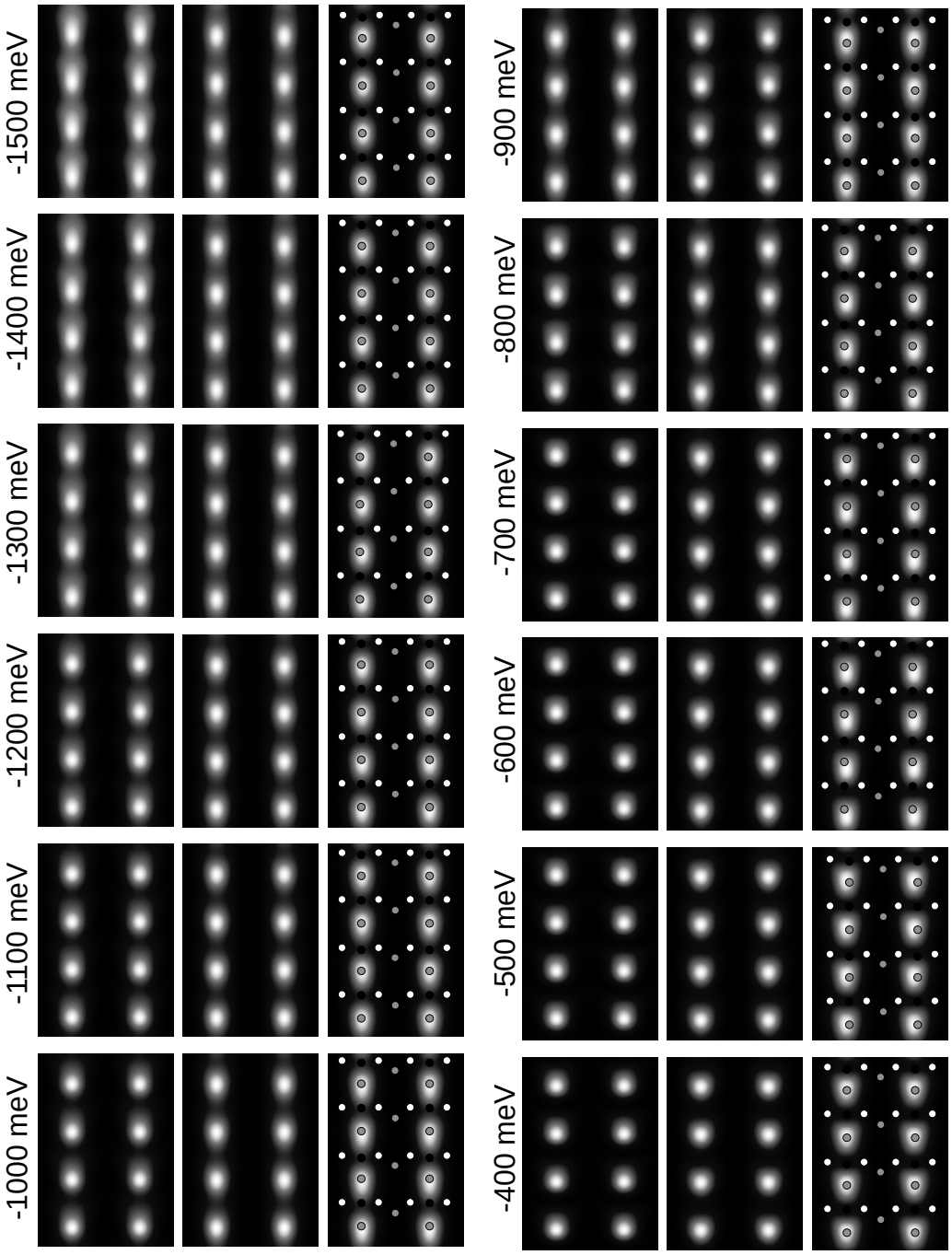

Figure 6.8: Topographic images at negative voltages for Fe[001]/InAs(110) at a distance of 10 a.u. from the surface. The spin1 channel is presented in the left column, the spin2 channel in the right, and the sum of both spin channels in the middle. The position of the atoms is indicated in the right column: Fe with black circles, As with white, and In with grey.

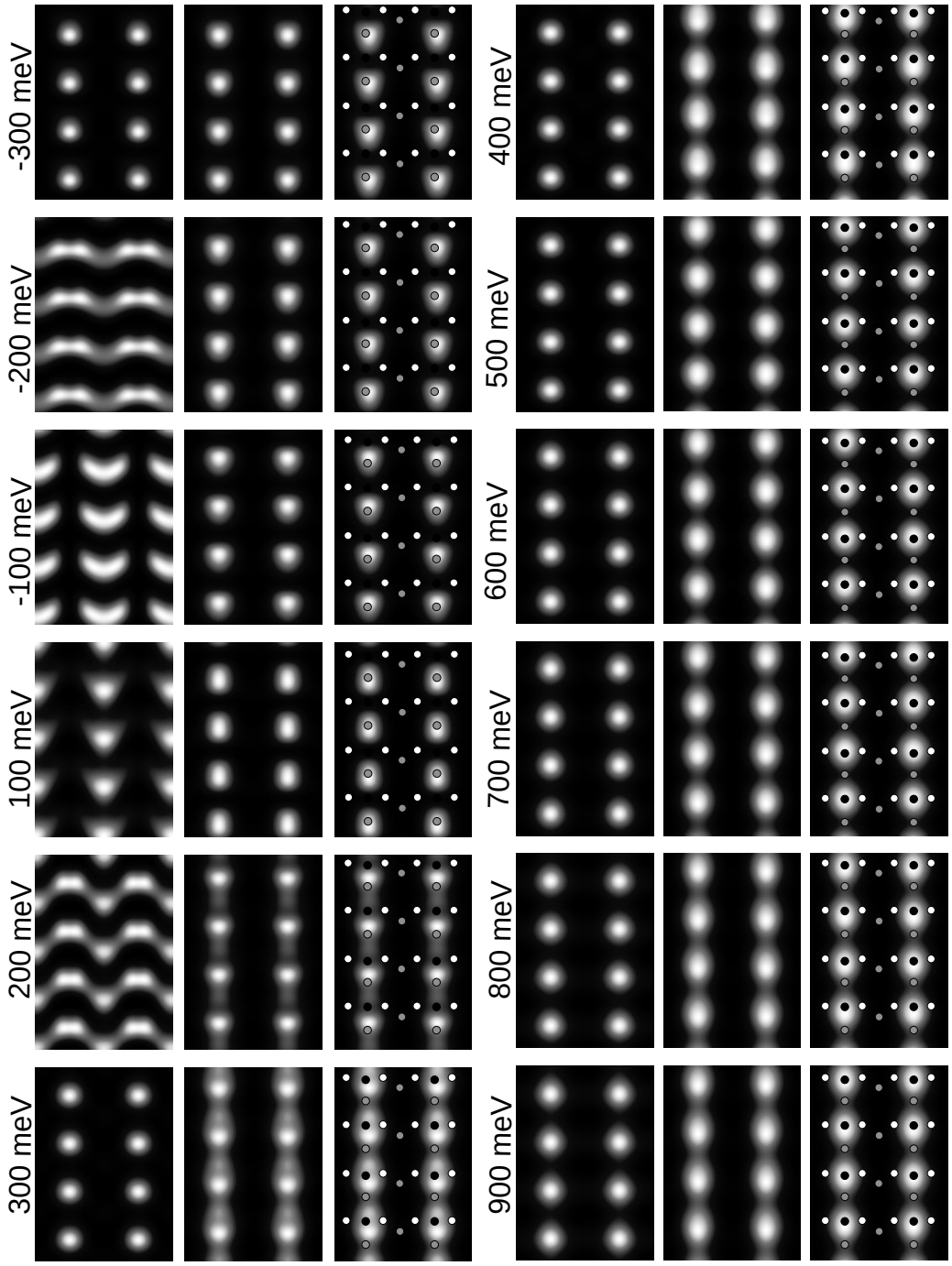

Figure 6.9: Topographic images around the E_F for Fe[001]/InAs(110) at a distance of 10 a.u. from the surface. The spin1 channel is presented in the left column, the spin2 channel in the right, and the sum of both spin channels in the middle. The position of the atoms is indicated in the right column: Fe with black circles, As with white, and In with grey.

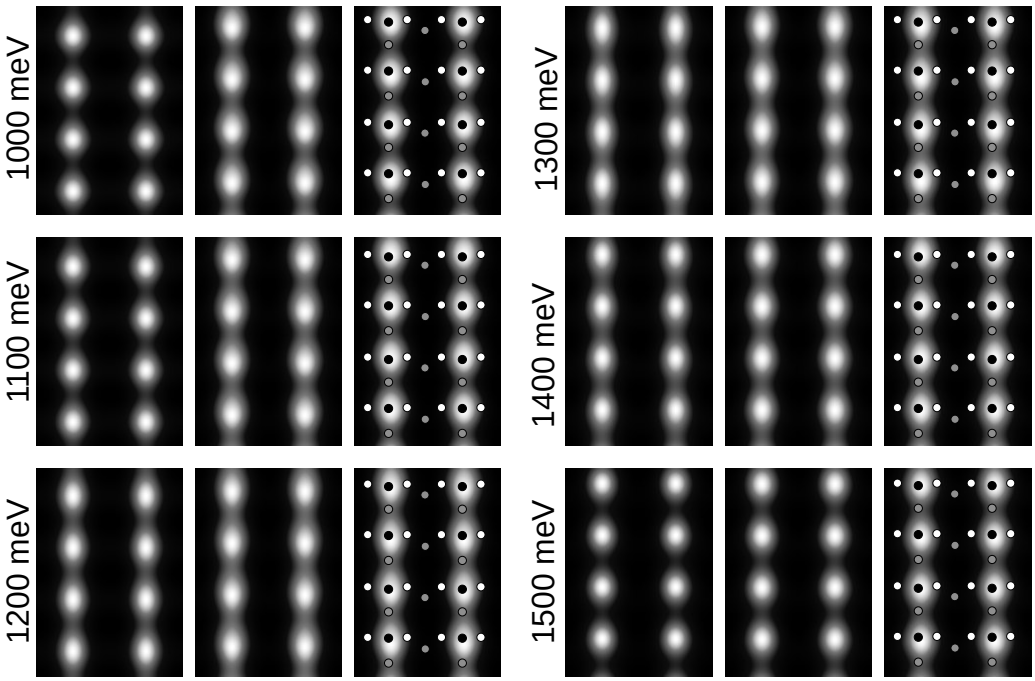

Figure 6.10: Topographic images at large positive voltages for Fe[001]/InAs(110) at a distance of 10 a.u. from the surface. The spin1 channel is presented in the left column, the spin2 channel in the right, and the sum of both spin channels in the middle. The position of the atoms is indicated in the right column: Fe with black circles, As with white, and In with grey.

Chapter 7

Spectroscopic difference between the Co(0001) hcp and fcc surfaces

7.1 Experimental motivation

The motivation for this part of the work come from STM measurements done on Co deposited on W(110). Fig. 7.1 (a) shows a constant current image of a monolayer high islands of Co on Co(0001)/W(110) taken during these measurements. The experimental details of this work are published in [51]. Two islands of a height of one ML are marked with black and white triangles, respectively. The topography of these two islands is very similar apart from the direction of the triangles. Despite this similarity in shape, the spectroscopy curves Fig. 7.1 (b) taken on each of the two islands are completely different. The intensity and the position of the peaks with energies below $-500\,\mathrm{meV}$ were found to depend on the tip. Only the peak at $-300\,\mathrm{meV}$ is reproducable in all experiments. Hence it follows that only the states around $-300\,\mathrm{meV}$ are related in the substrate. In order to find the reason for the different intensities of the spectroscopic peak at $-0.3\,\mathrm{eV}$ on the two islands imaged in Fig. 7.1 (a), we performed density-functional theory (DFT) calculations.

7.2 Calculational details

For simulating the Co(0001) surface we use a film geometry with 12 layers of Co embedded in infinite vacua on both sides of the film. We compare the perfect hcp structure (ABA) to an hcp structure exhibiting an fcc stacking-fault

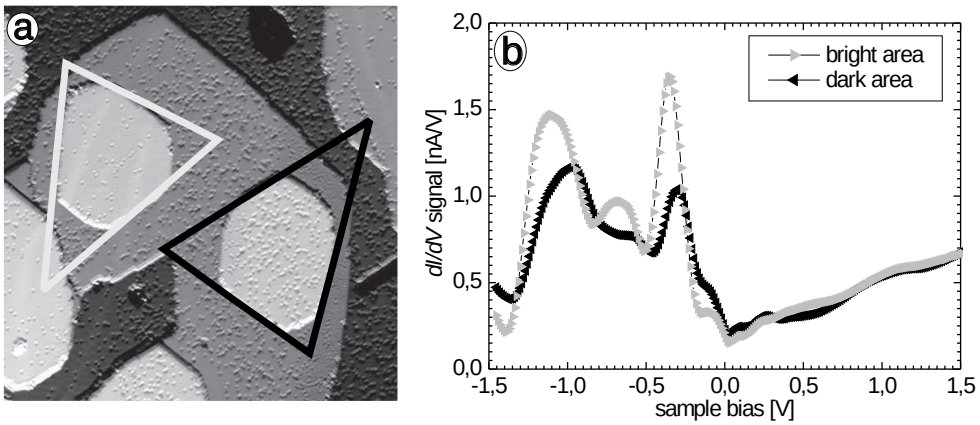

Figure 7.1: (a) Constant current image of Co ML islands on Co(0001), grown on W(110). (b) Spectroscopy curves taken correspondingly on the islands marked with white and black triangles in (a).

in both surface layers (ABC). The atomic positions in the two-dimensional unit cell are sketched for both cases in Fig. 7.2 (a). Both geometries are optimized by total-energy minimization using the theoretical Co bulk lattice constant which is determined to 2.509 Å (experimental value: 2.507 Å). Self-consistent results have been obtained with about 110 basis functions per atom and 26 **k**-points in the irreducible wedge of the 2DBZ (Fig. 7.2 (b)) as numerical parameters. The exchange-correlation functional is expressed within the generalized gradient approximation [39]. The Kohn-Sham equations are solved applying the FLAPW method, as realized in the `FLEUR`-code [23]. For the DOS calculation we used 50 **k**-points in the irreducible wedge of the 2DBZ. The spherical harmonics up to $l_{max} = 8$ are used for the basis functions in the muffin-tins and with $l_{max} = 6$ for the expansion of the non-spherical potential.

Compared with the ideal bulk termination, both surfaces are relaxed inwards. The surface layer of the faulted structure is relaxed by 0.046 Å and that of the unfaulted structure by 0.015 Å, which corresponds to 2.3% and 0.7% of the Co interlayer distance of 2.034 Å, respectively. The workfunction of the faulted structure (5.143 eV) is slightly larger than of the unfaulted structure 5.096 eV. Thus, the decay constant of the wavefunctions into the vacuum of the faulted structure is also slightly larger. The total energy of the faulted structure (fcc) is only 11 meV/atom larger than that of the unfaulted structure (hcp). Compared to $k_B T = 25$ meV/atom this small value

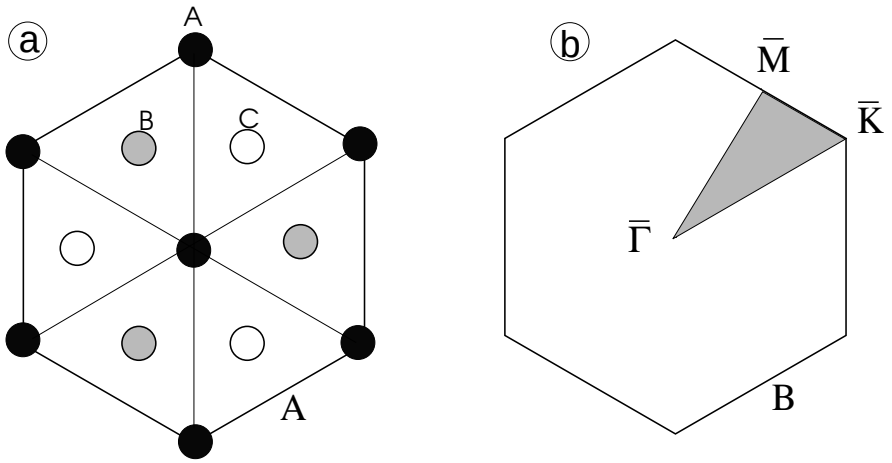

Figure 7.2: (a) The two-dimensional unit cell for the hcp and the hcp+fcc stacking fault structure. Black circles (A) mark the atomic positions in the third layer from the surface, grey (B) in the subsurface layer. The atoms in the surface layer have the position A for the hcp structure and for the fcc stacking fault the positions marked with white circles (C). (b) The corresponding 2DBZ with the irreducable part hatched grey. The side length of the hexagons in (a) and (b) have a relation of $B = \frac{2\pi}{A}$.

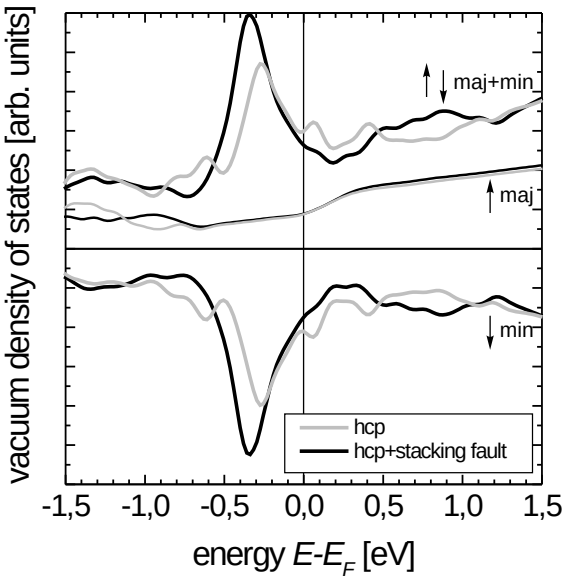

Figure 7.3: The vacuum DOS of the Co(0001) surface at the distance of 3 Å from the surface for the hcp-structure (grey) and hcp+fcc stacking fault surface (black). In the top part the majority spin DOS and the total DOS are shown. The lower part contains the minority spin DOS.

suggests that stacking fault nucleation sites occur rather frequently in thin film growth [8], possibly explaining the experimental observation that fcc areas exist in thin films even at room temperature.

7.3 Electronic structure

7.3.1 Difference in the calculated vacuum DOS between hcp and fcc surface

To simulate spectroscopic measurements we calculated the vacuum DOS for both structures. In the following all energies are given with respect to the Fermi level. Since the workfunctions of the faulted and the unfaulted structure differ by 47 meV, the Fermi levels are shifted accordingly with respect to the vacuum-zero. The results for the majority spin DOS and minority spin DOS as well as the sum of both DOSs are presented in Fig. 7.3 at a distance of 3 Å from the film surface.

The majority spin channel, shown in the top panel, exhibits a small shoulder between E_F and 200 meV and remains nearly featureless for the rest of the energy range. Consequently, the features in the averaged DOS are determined by the minority spin channel, which has a dominating peak at approx-

imately $-0.3\,\mathrm{eV}$ below E_F. The peak exhibits a full width at half maximum of $0.3 \pm 0.05\,\mathrm{eV}$. The unfaulted structure additionally has two minor peaks at $-600\,\mathrm{meV}$ and at $50\,\mathrm{meV}$. Since the proportion between different peaks in the vacuum DOS can change with the distance from the surface, we evaluated the vacuum DOS at distances ranging from 2 Å to 10 Å. For these distances the peak at -0.3 eV remains the dominating feature for both structures. Consequently, this peak corresponds to the one found in STS-measurements.

As visible in Fig. 7.3, the faulted structure exhibits a higher peak intensity than the unfaulted structure at $-0.3\,\mathrm{eV}$, and a lower intensity at $50\,\mathrm{meV}$ and $-0.6\,\mathrm{eV}$. We define a contrast between two peaks p_1 and p_2 like

$$c_{p_1,p_2} = \frac{DOS(p_1) - DOS(p_2)}{DOS(p_1) + DOS(p_2)}. \tag{7.1}$$

Then the contrast between faulted (f) and unfaulted (u) structures for these three peaks at two different distances amounts to:

Energy	$-0.6\,\mathrm{eV}$	$-0.3\,\mathrm{eV}$	$50\,\mathrm{meV}$
$C_{u,f}$ at 3 Å	0.35	−0.11	0.2
$C_{u,f}$ at 10 Å	0.62	−0.03	0.25

Table 7.1: Contrast of three peaks visible in Fig. 7.3 for the distance 3 Å, respectively 10 Å from the surface.

Moreover, the dominating peak on the faulted structure is at $-0.34\,\mathrm{eV}$, while that on the unfaulted structure is at $-0.28\,\mathrm{eV}$. This means that the peak on the faulted structure is shifted to lower energies by $60\,\mathrm{meV}$. These two findings are in excellent agreement with the STS results shown in Fig. 7.1 where an intensity change of $(50 \pm 20)\%$ and an energy shift of $55 \pm 35\,\mathrm{meV}$ are found. Finally, the calculated peak width is in reasonable agreement with the experimental result.

The reason for the difference between the two structures at $50\,\mathrm{meV}$ and $-600\,\mathrm{meV}$ is apparent from the relaxation data. The vacuum DOS curve is calculated at the distance of 3 Å from the vacuum boundary of the film, which is defined independently of the relaxation (chapter 2.4). The relaxation of the structures is such that the atoms of the fcc surface are shifted 0.03 Å further into the film from the vacuum boundary. Consequently, they contribute less than the atoms of the hcp surface to the vacuum DOS.

Tab. 7.1 shows that with increased distance from the surface the hcp peaks reach further than the fcc peaks. The reason for this is the smaller decay constant of the hcp structure, which leads to the change of the contrast

with distance in favour of the unfaulted surface for all three peaks at 50 meV, −0.3 eV and −0.6 eV.

7.3.2 Band structure analysis

Next we want to understand the mechanism behind why fcc stacking leads to a higher peak intensity at −0.3 eV. To answer this question, we first compare the vacuum DOS with the band structures of faulted and unfaulted surfaces. Fig. 7.4 shows band structures of majority (upper panel) and minority (lower panel) spin for both systems along the high symmetry directions. States which have more than 10% of their DOS in vacuum, are marked by black dots. The corresponding bands are identified as surface-related bands.

In the majority spin channel two of those bands are unoccupied with band minima at E_F and at 100 meV. These bandminima contribute to the shoulder between E_F and 200 meV in the vacuum DOS of Fig. 7.3. Two further surface-related bands which cross at the $\overline{\Gamma}$-point around −0.7 eV do not play a significant role in the vacuum DOS due to the high dispersion. The quantitative contribution to the vacuum DOS of the states around −1.4 eV at the $\overline{\Gamma}$-point is higher than 10%, but is a factor of 8 lower than the contribution from the band minima at E_F. For this reason they do not appear as a feature in Fig. 7.3.

In the minority spin channel two maxima and one minimum of surface-related bands exist in the energy range shown. The minimum is marked by the circles in Fig. 7.4 at approximately 1/4 of the way from $\overline{\Gamma}$ to $\overline{\mathrm{K}}$ and from $\overline{\Gamma}$ to $\overline{\mathrm{M}}$, respectively. This minimum is close to −0.3 eV. A second surface band has a maximum at about −0.5 eV and is located at the $\overline{\Gamma}$-point. This band maximum is visible in the vacuum DOS of the unfaulted structure as a peak at −0.6 eV in the minority spin DOS. For the faulted structure it is merged with the peak at −0.3 eV and cannot be distinguished clearly. Its contribution to the peak at −0.3 eV is a factor of 10 lower than the contribution of the band minimum away from $\overline{\Gamma}$. Consequently, the peak at −0.3 eV is caused by the band minimum of the surface band at 1/4 of the 2DBZ. The minor peak in the vacuum DOS at the hcp surface and the shoulder at the fcc faulted surface at 50 meV is caused by the band maximum at 50 meV at $\overline{\Gamma}$.

Therefore, we conclude that the band minimum is the origin of the peak measured by STS. This is in contrast to conclusions given for Co/Cu(111), where a band at $\bar{\Gamma}$ has been proposed to be responsible for the peak [37, 12].

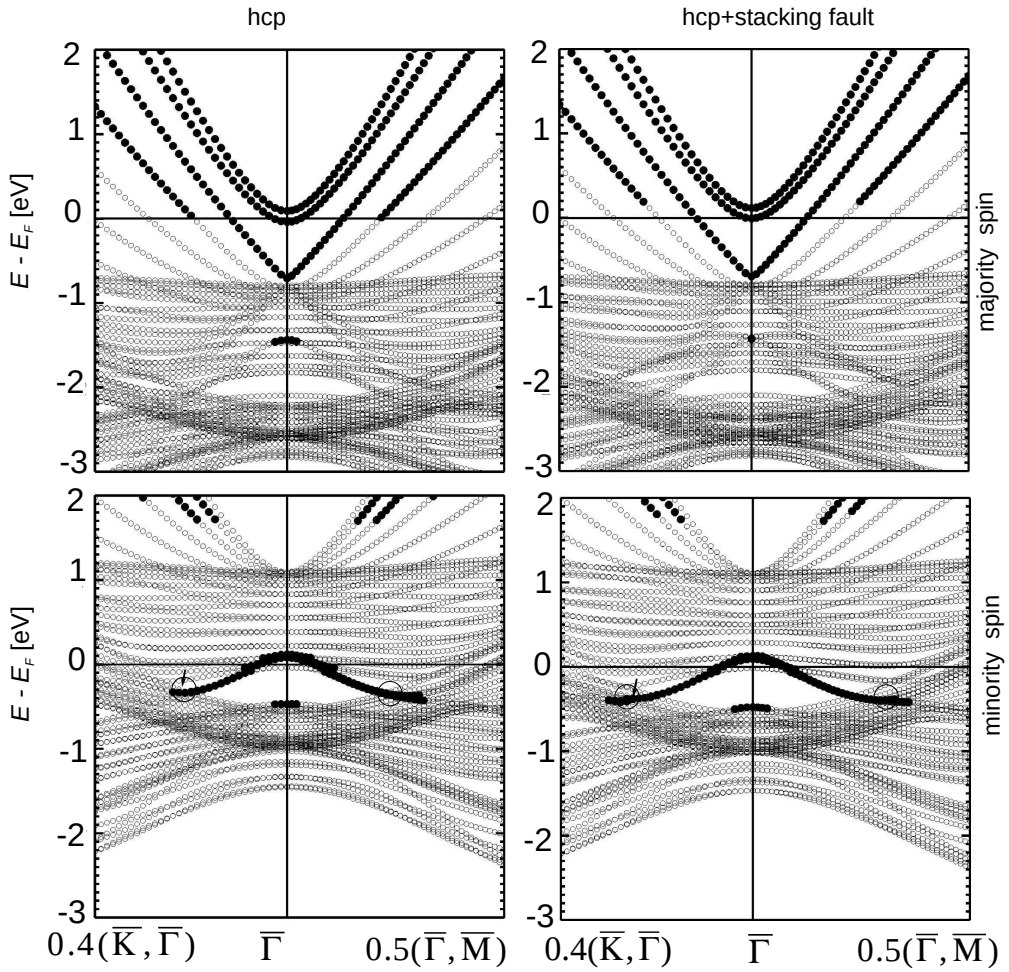

Figure 7.4: Majority spin (top part) and minority spin (lower part) band structure of the 12 ML Co slab in the unfaulted (left panel) and in the faulted (right panel) structure plotted along the high-symmetry directions in the neighborhood of $\overline{\Gamma}$. The empty circles represent the unprojected band structure, whereas the filled circles mark states that are located by more than 10% in vacuum.

7.4 Charge distribution analysis

7.4.1 Difference between the states at -0.3 eV and 50 meV

Finally, we analyze the charge distribution of the surface band of the minority spin channel with the band minimum at -300 meV. The character of this band with its minimum at 1/4 of the 2DBZ changes going from the band maximum at $\overline{\Gamma}$, where it has a predominant p-character, to the band minimum, where it has a $d_{3z^2-r^2}$-character with a small contribution of s- and p-states of less than 5%. The corresponding contour plots are presented in Fig. 7.5 (a) for the band maximum at 50 meV and at the $\overline{\Gamma}$-point, and in Fig. 7.5 (b) for the energy and the Bloch vector corresponding to the band minimum marked by arrows in Fig. 7.4. The contour lines between atomic positions are nearly horizontal in Fig. 7.5 (a). It is impossible to assign from the contour plot a specific character to this state. In contrast, the contour plots show a predominant $d_{3z^2-r^2}$-character at the surface layer with a minor contribution of an s-like character in Fig. 7.5 (b). The lobes of the DOS point away from the atomic positions into the vacuum in Fig. 7.5 (b). The extent of the state into the vacuum is slightly higher for the state in Fig. 7.5 (a) than in Fig. 7.5 (b). Within the bulk, the LDOS has at 50 meV $d_{3z^2-r^2}$- and at 300 meV predominant d_{xz}-character.

The contribution of the states, shown in Fig. 7.5, to the LDOS in each layer and in vacuum, normalised to 6 layers of Co, is indicated by the numbers next to the contour plots. The state at 50 meV (Fig. 7.5 (a)) has a huge part in the vacuum. Apart from the vacuum the largest contribution for both structures in Fig. 7.5 (a) and (b) is in the surface layer. Nevertheless, there is a considerable contribution in the subsurface layers. This means that the states at the surface can couple to bulk d-states. That this coupling takes place indeed can be concluded from the hybridization with the bulk d-bands near the band minimum and maximum, marked in Fig. 7.4. Consequently, the states have to be assigned to a *surface resonance* rather than to a *surface state*. In contrast, the dot marked band with the maximum at -0.5 eV at $\overline{\Gamma}$ is found to be a $d_{3z^2-r^2}$-surface state in accordance with the Co/Cu(111)-case [37, 12].

The large vacuum part of the state in Fig. 7.5 (a), which is located at $\overline{\Gamma}$, is in nice agreement with [21], where it is shown that the states with small $k_\parallel$ have a large probability density in vacuum. The vacuum part of the state at 300 meV in Fig. 7.5(b) is by a factor of 10 lower than that of the state at 50 meV. Nevertheless in the vacuum DOS (Fig. 7.3) the peak at 300 meV is much higher than the DOS at 50 meV. The reason is that in the 2DBZ the state at -300 meV is located on a ring with radius $\sim 1/4$ $\overline{\Gamma\mathrm{K}}$ and the

state at E_F is located at $\overline{\Gamma}$. Consequently, much more $k_{\|}$-vectors from the 2DBZ contribute to the peak at -300 meV. Summarizing we can say that three factors play a role for the high vacuum DOS of a state: the number of the Bloch waves that contribute to the state being determined by the dispersion of the corresponding band and by the part of the 2DBZ where the state is located; the third mechanism is that the states with shorter Bloch vectors have a higher probability density in vacuum [21]. In the cases, where the third and second mechanism are competitive, it is not possible to say without further analysis, if the states with shorter Bloch vectors carry the main part of the vacuum DOS.

7.4.2 Difference between the hcp- and fcc-surface

Now we examine the two states at 50 meV and -300 meV for similarities and differences between the faulted and unfaulted structures. In Fig. 7.5(a, b) the left panel shows the contour plots for the hcp structure at both energies, while the right panel contains the corresponding contour plots for the fcc structure. The numbers on the side of the contour plots in Fig. 7.5 show that the hcp structure has a slightly higher vacuum part for the state at 50 meV than the fcc surface. This can be explained from the different relaxation of both surfaces (section 7.3.1). The maximal deviation in the contribution of the layers between the two structures is 2%. Consequently, the charge distribution in the film is very similar for the hcp and fcc surface at 50 meV.

In contrast, the contribution of the third layer from the surface at -300 meV in Fig. 7.5 (b) is more than twice as high for the hcp than for the fcc structure. The reason for this can be explained as follows.

The contour plots in Fig. 7.5 (b) show that in the case of hcp-stacking the downward oriented orbitals of the surface atoms point directly to the atoms in the second subsurface layer. In contrast, for the faulted structure, the lobes point into the interstitial region. Accordingly, the surface resonance exhibits a stronger coupling to bulk d-states for pure hcp stacking than for stacking faults. This leads to a weaker electron-localization in the surface layer in the hcp case as can also be seen by comparing the distribution of the LDOS in the different layers (Fig. 7.5 (b)). As a consequence, the intensity of the vacuum DOS as measured by STS is lower for the hcp structure. The reason for a different brightness of hcp and fcc areas in dI/dV-maps at -300 meV thus is a different coupling of the $d_{3z^2-r^2}$-like surface resonance to the underlying bulk. Note that the intensity of the surface resonance in the hcp case is larger in the second subsurface layer than in the first subsurface layer. This approves the assumption that the geometrically induced coupling to the second subsurface layer is indeed the relevant coupling. Further, we

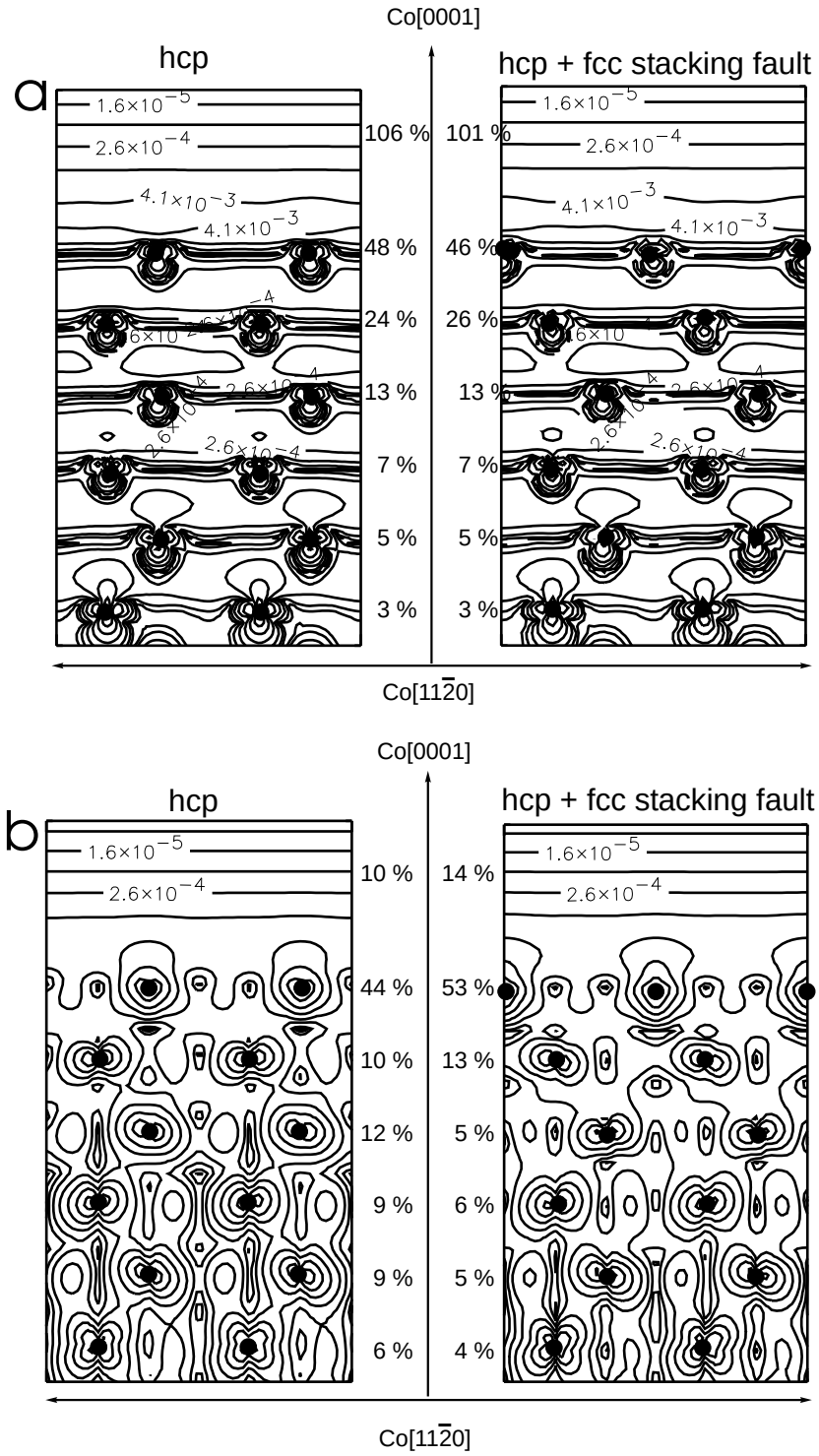

Figure 7.5: (a) Contour plots of the DOS for the band maximum of the surface related band at 50 meV located at $\overline{\Gamma}$. (b) Contour plots of the DOS for the band minimum of the surface related band at -300 meV away from $\overline{\Gamma}$.

want to point out that the surface resonance is crossing only one bulk d-band in the $(\bar{\Gamma}, \bar{K})$-direction before it runs into the band minimum in the hcp-case. In contrast, in the case of fcc stacking, the surface resonance crosses two bulk d-bands. Since the d-band to which the band minimum couples is approximately 50 meV lower in energy in the fcc case, the peak in the vacuum DOS accordingly occurs at lower energies.

In summary, the peak at $-300\,\mathrm{meV}$ measured by STS is assigned to a $d_{3z^2-r^2}$-like surface resonance with minority spin character and located in a band minimum away from $\overline{\Gamma}$. We identified the different appearances of hcp- and fcc-stacked areas in dI/dV-maps as due to a different, geometrically induced, coupling of the corresponding surface resonance to the bulk. This coupling is strongly dependent on the $d_{3z^2-r^2}$-like state at the surface atoms and does not work for the surface states with another symmetry.

Chapter 8

Summary

In this thesis, DFT calculations of Fe structures on InAs(110) as well as of Co islands on Co(0001) are presented. First the geometry of three different systems, namely an Fe monolayer and Fe chains along $[1\bar{1}0]$ (Fe$[1\bar{1}0]$/InAs(110)) and [001] (Fe[001]/InAs(110)) on InAs(110) are discussed. Then the electronic and magnetic structure of Fe chains on InAs(110) is studied in detail. A direct comparison between theory and experiment follows. The following results on the geometry of Fe structures on InAs(110) were obtained:

- An Fe atom in the Fe ML on InAs(110) takes almost the same position as an As atom along [001]. The relaxation is reversed compared to the pure InAs(110) surface. Under the Fe ML In has a higher position than As.

- For both chain structures, Fe becomes strongly bound to the As atoms. It takes a position in the arsenic's surrounding and at the same time as far as possible away from the In atoms. The bonds between the surface In and As are weakened in favour of the bonds between Fe and As.

- For the Fe$[1\bar{1}0]$/InAs(110) it is shown that Fe takes a position embedded in the surface in the middle of a triangle defined by three As atoms at the corners. The In atom previously bound to these atoms is relaxed out from the surface.

- For the Fe[001]/InAs(110) it is shown that Fe and one of the In atoms of the unit cell have almost the same vertical position. This In is located nearly equidistant to four surrounding As atoms of the surface.

For the magnetic and electronic structure of Fe chains on InAs(110) we found the following:

- The calculated magnetic structure of the chains is antiferromagnetic for Fe[1$\bar{1}$0]/InAs(110) and ferromagnetic for Fe[001]/InAs(110).
- We suggest as an explanation for the antiferromagnetic structure the antiferromagnetic superexchange between Fe atoms via d_{xy}(Fe)-p_y(As)-d_{xy}(Fe) and $d_{x^2-y^2}$(Fe)-p_x(As)-$d_{x^2-y^2}$(Fe). This is supported by analysing the electronic structure and the distribution of the LDOS around the Fe in the film.
- For the ferromagnetic structure of Fe[001]/InAs(110), the interaction between the Fe atoms is mediated through In, which has a position along the chain between Fe atoms, and neighbouring As. Fe interacts antiferromagnetically with As atoms: Fe↓-As_1↑ and ferromagnetically with In: Fe↑-In_1↑-Fe↑, Fe↓-In_1↓-Fe↓. Additionally, interaction of As with In contributes to the overall FM coupling between Fe atoms in the chain: Fe↓-As_1↑-In_1↑-As_1↑-Fe↓ Fe↓-As_1↑-In_1↓-As_1↑-Fe↓.
- The comparison with experimental results reveals, that there are two surface states around 1 eV. One is the rudiment of the In dangling bond and the other is an Fe state.
- An overview of the calculated topographic images is given, which shows that for Fe[001]/InAs(110) Fe atoms are imaged at large positive voltages while the In atoms are imaged at negative voltages. For Fe[1$\bar{1}$0]/InAs(110) Fe atoms are imaged at low negative voltages.

These calculations can serve as a starting point for further studies of transition metal structures on III-V semiconductor surfaces. From the experimental side the preparation of quasi-infinitely long chains of transition metals and STM measurements on them could be the next goal. From the theoretical side the simulation of monomers and multimers would improve the modeling of the experimental situation. Substitution of the Fe by other transition metals, or substitution of the InAs by other III-V semiconductors would give some insights into the dependance of the studied effects on the specific system.

In the last part of the work the interplay between geometry and electronic structure of the Co(0001) surface was studied. The results explain STM measurements on Co islands on Co(0001).

- The relaxation of the Co(0001) surface in hcp stacking and in hcp stacking with fcc stacking fault at the surface was calculated. The hcp surface relaxes inwards by 0.015 Å, whereas the faulted surface relaxes inwards by 0.046 Å.

- Both structures have a spin-polarized state around -300 meV. The intensity of this state is higher on the faulted structure. This is in nice agreement with STS measurements on Co islands on Co(0001). These measurements also show a peak around -300 meV with different intensity on the differently stacked islands.

- The intensity difference of this peak for different stackings is explained by a different, geometry induced coupling of the state at -300 meV to the bulk DOS.

Bibliography

[1] O. K. Andersen. Linear methods in band theory. *Phys. Rev. B*, 12:3060, 1975.

[2] P. W. Anderson. Antiferromagnetism. theory of superexchange interaction. *Phys. Rev.*, 79:350, 1950.

[3] V.I. Anisimov, V.P. Andropov, A.I. Lichtenstein, V.A. Gubanov, and A.V. Postnikov. Electronic structure and magnetic properties of 3d impurities in ferromagnetic metals. *Phys. Rev. B*, 37:5598, 1988.

[4] J. Bardeen. Tunnelling from a many-particle point of view. *Phys. Rev. Lett.*, 6:57, 1961.

[5] G. Binnig and H. Rohrer. Scanning tunnelling microscopy. *Helv. Phys. Acta*, 55:726, 1982.

[6] G. Binnig, H. Rohrer, Ch. Gerber, and E. Weibel. Surface studies by scanning tunneling microscopy. *Phys. Rev. Lett.*, 49:57, 1982.

[7] S. Blügel. *Theorie der Rastertunnelmikroskopie*. Forschungszentrum Jülich, 29. Ferienkurs des Instituts für Festkörperforschung: Physik der Nanostrukturen, 1998.

[8] C. Busse, C. Polop, M. Müller, K. Albe, U. Linke, and T. Michely. Stacking-fault nucleation on Ir(111). *Phys. Rev. Lett.*, 91:056103, 2003.

[9] C. J. Chen. Origin of atomic resolution on metal surfaces in scanning tunneling microscopy. *Phys. Rev. Lett.*, 65:448, 1990.

[10] C. J. Chen. Effects of $m \neq 0$ tip states in scanning tunneling microscopy: The explanations of corrugation reversal. *Phys. Rev. Lett.*, 69:1656, 1992.

[11] S. Datta and B. Das. Electronic analog of the electro-optic modulator. *Appl. Phys. Let.*, 56:665, 1990.

[12] L. Diekhöner, M. A. Schneider, A. N. Baranov, V. S. Stepanyuk, P. Bruno, and K. Kern. Surface states of cobalt nanoislands on Cu(111). *Phys. Rev. Lett*, 90:236801–1, 2003.

[13] T. Dietl, H. Ohno, F. Matsukura, J. Cibert, and D. Ferrand. Zener model description of ferromagnetism in zinc-blende magnetic semiconductors. *Science*, 287:1019, 2000.

[14] B. Engels, P. Richard, K. Schroeder, S. Blügel, Ph. Ebert, and K. Urban. Comparison between ab initio theory and scanning tunneling microscopy for (110) surfaces of iii-v semiconductors. *Phys. Rev. B*, 58:7799, 1998.

[15] S. C. Erwin, S.-H. Lee, and M. Scheffler. First principles study of nucleation, growth and interface structure of Fe/GaAs. *Phys. Rev. B*, 65:205422, 2002.

[16] R. P. Feynmann. Forces in molecules. *Phys. Rev.*, 56:340, 1937.

[17] J. B. Goodenough. *Magnetism and the Chemical Bond*. John Wiley & Sons, Inc., 1966.

[18] J. B. Goodenough and A. L. Loeb. Theory of ionic ordering, crystal distortion, and magnetic exchange due to covalent forces in spinels. *Phys. Rev.*, 98:391, 1955.

[19] D. Gottlieb and L. Wesoloski. Bardeen's tunneling theory as applied to scanning tunneling microscopy: a technical guide to the traditional interpretation. *Under review at Nanotechnology*.

[20] P. R. Hammar, B. R. Bennett, M. J. Yang, and M. Johnson. Observation of spin injection at a ferromagnet-semiconductor interface. *Phys. Rev. Lett.*, 83:203, 1999.

[21] S. Heinze. *First-Principles Thepry of Scanning Tunneling Microscopy Applied to Transition-Metal Surfaces*. University of Hamburg, PHD thesis, 2000.

[22] P. Hohenberg and W. Kohn. Inhomogenous electron gas. *Phys. Rev.*, 136:864, 1964.

[23] http://www.flapw.de.

[24] J. B. Klijn. *Local density of states of the adsorbat-induced two-dimensional electron system studied at zero and strong magnetic fields*. Thesis, Institute of Applied Physics, Hamburg University; Shaker Verlag, 2003.

[25] W. Kohn and L. J. Sham. Self-consistent equations including exchange and correlation effects. *Phys. Rev.*, 140:A1133, 1965.

[26] H. Krakauer, M. Posternak, and A.J. Freeman. Linearized augmented plane-wave method for the electronic band structure of thin films. *prb*, 19:1706, 1979.

[27] H. A. Kramers. L'interaction entre les atomes magnétogènes dans un cristal paramagnétique. *Physica*, 1:182, 1934.

[28] P. Kurz. *Non-Collinear Magnetism at Surfaces and in Ultrathin Films*. Thesis, Institut für Festkörperforschung, Forschungszentrum Jülich, 2000.

[29] P. Mahadevan, A. Zunger, and D. D. Sarma. Unusual directional dependence of exchange energies in GaAs diluted with Mn: Is the rkky relevant? *Phys. Rev. Let.*, 93:177201, 2004.

[30] T. Matsui, C. Meyer, L. Sacharow, and R. Wiesendanger. STM/STS observation of Fe multimers on semiconductor surface, to be published.

[31] Ph. Mavropoulos, O. Wunnicke, and P. H. Dederichs. Ballistic spin injection and detection in Fe/semiconductor/Fe junctions. *Phys. Rev. B*, 66:024416, 2002.

[32] Y. Mokrousov. *Ab initio All-electron Full-potential Linearized Augmented Plane-wave Method for One-dimensional Systems*. PhD-Thesis, Forschungszentrum Jülich GmbH, Institut für Festkörperforschung, 2005.

[33] M. Morgenstern, M. Getzlaff, D. Haude, and R. Wiesendanger. Coverage dependence of the Fe-induced Fermi-level shift and the two dimensional electron gas on InAs(110). *Phys. Rev. B*, 61:13805, 2000.

[34] M. Morgenstern, D. Haude, J. Klijn, C. Meyer, L. Sacharow, S. Heinze, S. Blügel, and R. Wiesendanger. Comparing the local density of states of three- and two-dimensional electron systems by low-temperature scanning tunneling spectroscopy. *Physica E*, 16:121, 2003.

[35] V. L. Moruzzi, J. F. Janak, and A. R. Williams. *Calculated electronic properties of metals*. Pergamon, New York, 1978.

[36] H. Ohno. Making nonmagnetic semiconductors ferromagnetic. *Science*, 281:951, 1998.

[37] S. N. Okuno, T. Kishi, and K. Tanaka. Spin-polarized tunneling spectroscopy of Co(0001) surface states. *Phys. Rev. Lett.*, 88:066803, 2002.

[38] C. Pampuch, O. Rader, T. Kachel, W. Gudat, C. Carbone, R. Kläsges, G. Bihlmayer, S. Blügel, and W. Eberhardt. One-dimensional spin-polarized quantum-wire states in Au on Ni(110). *Phys. Rev. Lett.*, 85:2561, 2000.

[39] J. P. Perdew, K. Burke, and M. Ernzerhof. Generalized gradient approximation made simple. *Phys. Rev. Lett*, 77:3865, 1996.

[40] J. P. Perdew and Y. Wang. Accurate and simple analytic representation of the electron-gas correlation energy. *Phys. Rev. B*, 45:13244, 1992.

[41] J. P. Perdew and A. Zunger. Self-interaction correction to density-functional approximations for many-electron systems. *Phys. Rev. B*, 23:5048, 1981.

[42] P. Pulay. Ab initio calculation of force constants and equilibrium geometries in polyatomic molecules. *Mol. Phys.*, 17:197, 1969.

[43] L.M. Sandratskii. Noncollinear magnetism in itinerant-electron systems: theory and applications. *Adv. Phys.*, 47:91, 1998.

[44] A.B. Shick, A. I. Lichtenstein, and W. E. Pickett. Implementation of the LDA+U method using the full-potential linearized augmented plane-wave basis. *Phys. Rev. B*, 60:10763, 1999.

[45] J. C. Slater. Wave functions in a periodic potential. *Phys. Rev.*, 51:846, 1937.

[46] M. Städele, J.A. Majewski, P. Vogl, and A. Görling. Exact Kohn-Sham exchange potential in semiconductors. *Phys. Rev. Lett.*, 79:2089, 1997.

[47] W.M. Temmerman, A. Svane, Z. Szotek, and H. Winter. *Electronic density functional theory: Recent progress and new directions.* Plenum Press, New York, 1998.

[48] J. Tersoff and D. R. Hamann. Theory and application for the scanning tunneling microscope. *Phys. Rev. Lett.*, 50:1998, 1983.

[49] J. Tersoff and D. R. Hamann. Theory of the STM. *Phys. Rev. B*, 31:805, 1985.

[50] U. von Barth and L. Hedin. Description of exchange and correlation effects in inhomogeneous electron systems. *J.Phys. C*, 5:1629, 1972.

[51] J. Wiebe, L. Sacharow, A. Wachowiak, G. Bihlmayer, S. Heinze, S. Blügel, M. Morgenstern, and R. Wiesendanger. Scanning tunneling spectroscopy on Co(0001): Spectroscopic signature of stacking faults and dislocation lines. *Phys. Rev. B*, 70:035404, 2004.

[52] R. Wiesendanger. *Scanning Probe Microscopy and Spectroscopy.* Cambridge University Press, 1994.

[53] E. Wimmer, H. Krakauer, M. Weinert, and A.J. Freeman. Full-potential self-consistent linearized-augmented-plane-wave method for calculating the electronic structure of molecules and surfaces: O_2 molecule. *Phys. Rev. B*, 24:864, 1981.

[54] O. Wunnicke, Ph. Mavropoulos, R. Zeller, P. H. Dederichs, and D. Grundler. Ballistic spin injection from Fe(001) into ZnSe and GaAs. *Phys. Rev. B*, 65:241306, 2002.

[55] R. Yu, D. Singh, and H. Krakauer. All-electron and pseudopotential force calculations using the linearized-augmented-plane-wave method. *Phys. Rev. B*, 43:6411, 1991.

[56] H. J. Zhu, M. Ramsteiner, H. Kostial, M. Wassermeier, H.-P. Schönherr, and K. H. Ploog. Room-temperature spin injection from Fe into GaAs. *Phys. Rev. Lett.*, 87:016601, 2001.

Publications and Conference Contributions

Publications

- J. Klijn, L. Sacharow, Chr. Meyer, S. Blügel, M. Morgenstern, and R. Wiesendanger: *STM measurements on the InAs(110) surface directly compared with surface electronic structure calculations.* Phys. Rev. B 68, 205327 (2003)
- J. Wiebe, L. Sacharow, A. Wachowiak, G. Bihlmayer, S. Heinze, S. Blügel, M. Morgenstern, and R. Wiesendanger: *Scanning tunneling spectroscopy on cobalt(0001): spectroscopic signature of stacking faults and dislocation lines.* Phys. Rev. B 70, 35404 (2004)
- L. Sacharow, G. Bihlmayer, S. Blügel, and M. Morgenstern: *High spin polarization at the Fe/InAs(110) interface.* Phys. Rev. B 69, 85317 (2004)

Conference Contributions

- L. Sacharow, M. Morgenstern, G. Bihlmayer, S. Blügel und R. Wiesendanger: *Hohe Spinpolarisation an der Fe/InAs(110) Grenzfläche*, Dresden, 24 -28 March 2003 (talk)
- L. Sacharow, J. Wiebe, A. Wachowiak, G. Bihlmayer, S. Heinze, S. Blügel, M. Morgenstern, and R. Wiesendanger: *Vergleich der ab-initio berechneten elektronischen Struktur verschiedener Stapelfolgen von Co (0001)*, Regensburg, 8 - 12 March 2004 (talk)
- L. Sacharow, J. Wiebe, A. Wachowiak, G. Bihlmayer, S. Heinze, S. Blügel, M. Morgenstern, and R. Wiesendanger: *Comparison of ab-initio calculated electronic structure: hcp- contra fcc-Co(1000) surface.*, XIV work-

shop on computational materials science CMS2004, Calaserena Village, Geremeas, Sardinia, Italy, 18 - 23 September 2004 (talk)

- L. Sacharow: *Die elektronische Struktur von Fe-Ketten auf der InAs(110)-Oberfläche*, GrK Workshop "Nanostrukturierte Festkörper", St. Peter-Ording, 13 - 15 December 2004 (talk)

- T. Matsui, C. Meyer, L. Sacharow, R. Wiesendanger: *STM/STS Observation of Fe multimers on Semiconductor Surface.*, 13 International Conference on Scanning Tunneling Microscopy/Spectroscopy and related Techniques, Sapporo Convention Center, Japan, 3-8 July 2005

Danksagung

An dieser Stelle möchte ich mich bei allen Menschen recht herzlich bedanken, die mit Ihrer Hilfe, Förderung, Geduld und Freundschaft maßgeblich zum Gelingen dieser Arbeit beigetragen haben.

Prof. Dr. Roland Wiesendanger danke ich für die exzellenten Arbeitsbedingungen und eine tolle, motivierende Atmosphäre in seiner Forschungsgruppe.

Prof. Dr. Markus Morgenstern danke ich für die Unterstützung durch sein Wissen, seine Erfahrung und sein Engagement. Ohne seine Betreuung wäre diese Arbeit nie fertig geworden.

Prof. Dr. Stefan Blügel danke ich für seine Begeisterungsfähigkeit und das tolle Programm `FLEUR`.

Prof. Dr. Alexander Lichtenstein danke ich für die Diskussionen und Erklärungen zum Superexchangemechanismus.

Gustav Bihlmayer danke ich für seine Geduld und die vielen Tips und Erklärungen zu `FLEUR` und vielen anderen Sachen.

Meinem Freund Felix Marczinowski danke ich für seine Geduld und Unterstützung, dafür daß er mir Mut gemacht hat wo ich mutlos war, gut zugeredet wo ich drauf und dran war alles zu schmeissen und für das gründliche Korrekturlesen dieser Arbeit.

Jan Klijn danke ich für seine Freundschaft, für sehr schöne und lustige Zeit während wir zusammengearbeitet haben und für ganz viel Unterstützung unterschielichster Art während ich zusammengeschrieben habe.

Christian Meyer danke ich für die vielen Tips mit den Rechnern und die nette und lustige Atmosphäre bei uns im Büro.

Theophilos Maltezopoulos danke ich für ganz viel Spaös während der Arbeit zusammen mit Christian Meyer und Jan Klijn.

Yuri Mokrousov danke ich für das gründliche Korrekturlesen des Theorieteils dieser Arbeit und unterstützende Worte in letzter und schwierigster Phase.

Marjanna Lezaic, Manfred Niesert und Marcus Heide danke ich für sehr viel Spass den ich während meiner Aufenthalte in Jülich hatte.

Ein ganz großer und besonderer Dank gilt allen Administratoren und Ansprechpartnern an diversen Rechenanlagen, die ich schwer arbeiten ließ. Dazu gehört das Physnet-Team der Uni-Hamburg, die Administratoren an den Multiprozessorrechnern des RRZ-Hamburg, die Administratoren und Ansprechpartner am HLRN-Zentrum in Berlin und natürlich die Mitarbeiter am ZAM im Forschungszentrum Jülich. Ohne die Kompetenz und Hilfsbereitschaft dieser Menschen wäre ich verloren gewesen.

Meinen Eltern danke ich für die stetige Unterstützung in jeder Hinsicht, die ich in jeder Phase meiner Ausbildung und Doktorarbeit erfahren habe.